Single-source-precursor synthesized SiC-based nanocomposites with an in-situ formed Nowotny phase as multifunctional materials for electrocatalytic and electromagnetic wave absorbing applications

M. Sc. Yao Feng

Prof. Dr. Ralf Riedel (Supervisor)

Dispersive Solids, Department of Materials and Earth Sciences

TECHNISCHE UNIVERSITÄT DARMSTADT

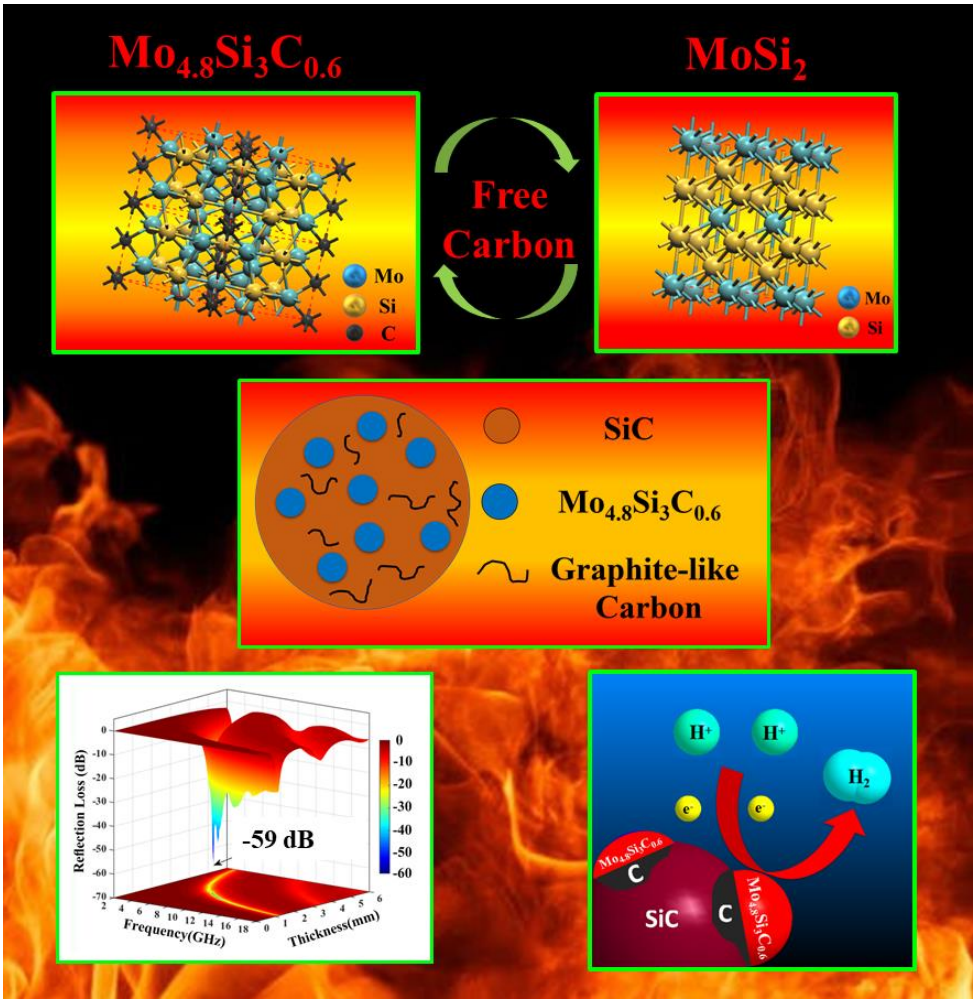

A Cumulative Dissertation approved by the Department of Materials and Earth Sciences in Fulfillment of the Requirements for the Degree of Rerum Naturalium (Dr. rer. nat.)

Single-source-precursor synthesized SiC-based nanocomposites with an in-situ formed Nowotny phase as multifunctional materials for electrocatalytic and electromagnetic wave absorbing applications

M. Sc. Yao Feng

From Xiangtan, Hunan, China, Matrikel-Nr.: 2787224

TECHNISCHE UNIVERSITÄT DARMSTADT

Referee: Prof. Dr. Ralf Riedel

Co-referee: Prof. Dr. Zhaoju Yu

Co-referee: Prof. Dr. Anke Weidenkaff

Fachbereich Material- und Geowissenschaften

Technische Universität Darmstadt

Date of submission: 07.07.2020

Date of oral examination: 26.10.2020

Darmstadt 2020

D 17

Yao Feng: Single-source-precursor synthesized SiC-based nanocomposites with an in-situ formed Nowotny phase as multifunctional materials for electrocatalytic and electromagnetic wave absorbing applications

Darmstadt, Technische Universität Darmstadt
Publication Year of Dissertation at TUprints: 2021
URN: urn:nbn:de:tuda-tuprints- 145511
Date of Oral Examination: 26.10.2020

Darmstadt 2020
D 17

Dedicated to my parents (献予我的父母)

Declaration

M. Sc. Yao Feng

Nieder-Ramstädter-Str. 11

64283 Darmstadt

Declaration

This work described in this thesis was carried out at the Department of Materials and Earth Sciences, Technische Universität Darmstadt during the period October 2016 to May 2020. This thesis represents the author's original work, except where otherwise stated, and no part of it has been submitted for a degree at any other university. Prior to the submission of this thesis, some work has been published as described in the relevant chapters herein.

Eidesstattliche Erklärung

Hiermit erkläre ich an Eides statt, dass ich die vorliegende Dissertation selbstständig und nur mit den angegebenen Hilfsmitteln angefertigt habe. Von mir wurde weder an der Technischen Universität Darmstadt noch einer anderen Hochschule ein Promotionsversuch unternommen.

Darmstadt, den 24.04.2020

M. Sc. Yao Feng (冯珧)

The presented cumulative dissertation summarizes the essential scientific findings, which were reported to the scientific community in the following peer-reviewed journals. Copies of the published studies below are enclosed in the Chapter Cumulative Publications of this thesis.

1. **Feng Y**, Yu Z, Schuch J, Tao S, Wiehl L, Fasel C, Jaegermann W, Riedel R, Ternary Nowotny phase $Mo_{3+2x}Si_3C_{0.6}$ dispersed in a porous SiC/C matrix: A novel catalyst for hydrogen evolution reaction. *Journal of the American Ceramic Society*, 103 (2020) 508-519.

2. **Feng Y**, Yu Z, Riedel R, Enhanced hydrogen evolution reaction catalyzed by carbon-rich $Mo_{4.8}Si_3C_{0.6}$/C/SiC nanocomposites via a PDC approach. *Journal of the American Ceramic Society*, 103 (2020) 1385-1395.

3. **Feng Y**, Yang Y, Wen Q, Riedel R, Yu Z, Dielectric properties and electromagnetic wave absorbing performance of single-source-precursor synthesized $Mo_{4.8}Si_3C_{0.6}/SiC/C_{free}$ nanocomposites with an in-situ formed Nowotny phase. *ACS Applied Materials & Interfaces*, 2 (2020) 16912-16921.

Contents

List of figures

List of tables

List of abbreviations

PDCs	Polymer derived ceramics
HER	Hydrogen evolution reaction
CNTs	Carbon nanotubes
RGO	Reduced graphene oxide
EM	Electromagnetic
EMA	Electromagnetic wave absorbing
SSA	Specific surface area
NP	Nowotny phase
DVB	Divinylbenzene
OER	Oxygen evolution reaction
NHE	Normal hydrogen electrode
RHE	Relative hydrogen electrode
E	Applied potential
E_{HER}	Standard reduction potential for an RHE reference
iR	Ohmic potential drop of current flow in ionic electrolyte
η	Excess potential (overpotential)
H^+	Proton
e^-	Electron
A	An empty active site of the catalyst surface
AH_{ads}	An adsorbed hydrogen atom
ΔG_H	Free energy of hydrogen adsorption
i_0	Exchange current density
ε	Complex permittivity
μ	Complex permeability
tan δ/ tg δ	Loss tangent
$\varepsilon'/\varepsilon''$	Real part of the permittivity/ Imaginary part of the permittivity
μ'/μ''	Real part of the permeability/ Imaginary part of the permeability

EMW	Electromagnetic wave
MA	Microwave absorption
RC	Reflection coefficient
RL	Reflection loss
RL_{min}	The minimum reflection loss
EAB	Effective absorption bandwidth
P_I /P_R	Incident/received power of an EM wave
Z_{in}	Input impedance at the air-absorber interface
Z_0	Intrinsic impedance of free space
α	Attenuation constant
f	Frequency of the electromagnetic wave
d	Thickness of the microwave absorbing material
σ(T)	Temperature-dependent electrical conductivity
σ	Electrical conductivity
CCVD	Chemical catalytic vapor deposition
CVI	Chemical vapor infiltration
CMCs	Ceramic matrix composites
SSPs	Single-source precursors
AHPCS	Allylhydridopolycarbosilane (SMP10)
PDC-NCs	Polymer-derived ceramic nanocomposites
PCS	Polycarbosilane
CMC	Ceramic–matrix composites
NEMS/ MEMS	Nano-electromechanical/micro-electromechanical systems
FT-IR	Fourier transformed infrared spectroscopy
ATR	Attenuated-total-reflectance
TGA	Thermogravimetric analysis
TG/MS	Thermogravimetric analysis coupled with mass spectrometry
NMR	Nuclear magnetic resonance

MAS NMR	Magic-angle spinning nuclear magnetic resonance
XRD	X-ray diffraction
TEM	Transmission electron microscopy
HRTEM	High-resolution transmission electron microscopy
SEAD	Selected Area Electron Diffraction
SEM	Scanning electron microscopy
XPS	X-ray photoelectron spectroscopy
BET	Brunauer-Emmett-Teller theory
EIS	Electrochemical impedance spectroscopy
OCP	Open circuit potential
CV	Cyclic voltammogram
η_1/η_{10}	the overpotentials driving current densities of 1 mA cm^{-2}/10 mA cm^{-2}
EASA	Electrochemical active surface area
C_{dl}	Double-layer capacitances
S_{ij}	Scattering parameters
C_{free}	Free carbon
wt.% / vol.% / mol%	Weight percent/Volume percent/Mol percent

1. Introduction and motivation

Hydrogen has been considered as a clean renewable energy source since the beginning of the 1970's [6]. However, for the moment, our major energy resources are still limited by non-renewable fossil fuels (coal, oil and natural gas) which caused a series of critical global environmental crisis, such as air/water pollution and global warming [7]. Therefore, for the ecological development of human economy and society, sustainable energy, particularly hydrogen, is becoming an urgent task, which has aroused widespread concern in the past decades [8-10]. Among all of the strategies to yield hydrogen fuel, electrochemical water splitting is one of the most efficient ways due to its renewability and environmental-friendliness [1, 11]. The electrocatalytic hydrogen evolution reaction (HER), as a crucial half-cell reaction of electrochemical water splitting , is the reduction of aqueous protons by electrons passed through a catalyst to liberate H_2 [12]. For minimizing the energy loss during HER, researchers are seeking for suitable electrocatalysts which can significantly decrease the overpotential and consequently promote the reaction rate and total cell efficiency [13]. In general, platinum (Pt) or Pt-group composite materials are considered as the most efficient catalysts for HER [5, 14-15]. However, Pt and its alloys are too low earth-abundance and expensive to be utilized for large-scale energy conversion applications [14, 16]. Thus, in recent years, advanced alternative electrocatalysts based on earth-abundant and cost-effective elements have attracted a lot of attention as a desirable replacement for Pt-containing catalysts [17-19]. Among many kinds of noble-metal free HER catalysts, transition-metal-based catalysts (such as Mo-based [20], Co-based [21] and Ni-based [22-23] compounds) have been reported to possess excellent electrocatalytic activity and long-term durability in terms of the HER process, due to their d-band electronic density-of-state similar to that of Pt [24-25]. In addition, a rational nanostructure and porous morphology will not only increase active sites and reduce the catalyst amount but also contribute to alleviate the overpotential brought about by the resistances of ions, gas diffusion and charge transfer [13]. Some conductive supports with high surface area, such as carbon nanosheets [26-28], carbon nanotubes (CNTs) [29-31] and reduced graphene oxide (RGO) [32-34], are introduced to further increase the reaction rate of HER.

High frequency electromagnetic (EM) wave is identified as a form of microwaves in the wavelength range from 2.4×10^{-2} m to 3.7×10^{-2} m [35]. The rapid development of high-frequency electronic components and devices, particularly in the field of telecommunication, has already caused serious electromagnetic interference and pollution which are threatening human being's health [36-38]. Therefore, high-performance electromagnetic wave absorbing (EMA) materials are playing more and more important role in a large variety of practical applications such as wireless communication and stealth technology [35, 39]. Particularly, when EMA materials are applied in some hostile environments, such as aggressive media or high temperatures, they are further required to possess outstanding oxidation resistance, high melting point, high chemical stability and thermal stability [40-43]. From some research, we note that silicon carbide (SiC) is considered as promising candidate material for EMA, which can be applied in in harsh environments, due to its outstanding oxidation resistance, high melting point and thermal/chemical stability [44-46]. However,

the EMA performance of pure SiC is limited by its inappropriate dielectric properties with low dielectric loss, because of the poor electrical conductivity (ca. 10^{-3} S/cm) [47-49]. The introduction of electrically conductive phases (e.g., CNTs [50-51], graphene [52], Ni [53], Fe [47], and HfC [54] and others) into the SiC matrix is an efficient strategy to enhance the EMA performance of SiC-based ceramics by tailoring the complex permittivity of composites. However, there are still some inevitable drawbacks in the above-mentioned materials. For example, when carbon nanofillers (CNTs or graphene) were introduced into the SiC matrix by mechanically mixing, their aggregation effect leads to an inhomogeneous dispersion of those carbon nanofillers [55]. Then, for some metal phases (Fe/Ni phases), their poor chemical stability will cause those phases to get easily corroded in hostile environments [47, 53]. Moreover, practical applications of HfC are limited by its high density and cost [54].

Silicon-based polymer-derived ceramics (PDCs) have been used for the fabrication of mainly Si-based advanced ceramics since 50 years ago [56-57]. Consequently, the recent research extended remarkably the possible fields of applications of PDCs including high-temperature-resistant materials (energy materials, automotive, aerospace, etc.), hard materials, chemical engineering (catalyst support, food- and biotechnology, etc.), or functional materials in electrical engineering as well as in micro/nanoelectronics [58]. Particularly, PDC technology is a simple method to produce porous ceramics as catalyst supports [59-61] with high specific surface area (SSA) [62-63] and outstanding corrosion stability [64]. Nevertheless, there is a lack of knowledge concerning silicon-based polymer-derived ceramics applied for electrochemical water splitting. Moreover, after considering the advantages and above-mentioned limitations of SiC, advanced SiC-based (nano)composites are explored in this study for the application as EMA materials.

In the early 1954, the Nowotny phase (NP, $Mo_{4.8}Si_3C_{0.6}$), as the only stable ternary phase in the Mo-Si-C system, was identified and characterized by Nowotny and coauthors for the first time [65]. Due to the intrinsic properties including its excellent mechanical behavior and high melting point (~ 2100 °C), the NP becomes a promising second-phase in SiC-based ceramics for high temperature applications [65-66]. Accordingly, $Mo_{4.8}Si_3C_{0.6}$/SiC-based composites revealed enhanced fracture toughness and creep resistance at both room and high-temperatures [67-69] as well as outstanding oxidation resistance up to 1600 °C [70]. Moreover, Zhu et al. [67] found the $Mo_{4.8}Si_3C_{0.6}$ phase exhibiting high electrical conductivity, and its superconducting transition temperature is reported to be as high as 12.2 K [71]. By now, in addition to the above-mentioned applications, the literature concerning functional properties of NP is very limited. Thus, the further development of other possible applied field of NP is still an attractive challenge.

Based on the above-mentioned discussion, this Ph.D. thesis comprises three parts summarizing three accepted publications [72-74]. In the first part of the present study, the Nowotny phase embedded in a porous SiC/C nanocomposite matrix was synthesized via a single-source-precursor approach which involves the reaction of allylhydridopolycarbosilane with $MoO_2(acac)_2$. It is the first time to discover that NP/C/SiC ceramic nanocomposites exhibit outstanding electrocatalytic properties suitable for the electrochemical hydrogen evolution. Then, in the second part, divinylbenzene (DVB) was used as a carbon-rich source to synthesize

mesoporous NP/C/SiC ceramic nanocomposites with higher carbon content. The HER activity of the carbon-rich NP/C/SiC ceramic nanocomposites was further improved, due to their enhanced conductivity and surface area. Finally, the third part of the thesis describes the discovery of interesting dielectric properties and outstanding EMA performance of the as-synthesized NP/C/SiC ceramic nanocomposites. The high-temperature phase evolution of the respected nanocomposites is discussed as well in this part.

2 Fundamentals

In this chapter, the fundamentals and basic principles underlying the scientific findings of the present thesis are introduced and discussed with respect to the latest research developments.

2.1 Electrochemical water splitting

2.1.1 General background

Hydrogen is considered as an ideal renewable energy source for the replacement of fossil fuels due to free emission of greenhouse gas (e.g. CO_2) during the processes of energy conversion [75]. Hydrogen, unlike oil and natural gas, is not a natural energy source on our planet. Thus, effective and low-cost hydrogen production is one of the greatest challenges for its large-scale utilization [1, 76]. **Figure.2.1** summarizes three main types of industrial hydrogen production: steam methane reforming, coal gasification and water electrolysis [1]. At present, more than 95 % of industrial hydrogen is produced by steam methane reforming and coal gasification, which means current hydrogen production is still strongly dependent on fossil fuels [1]. Besides, the high temperature reaction of steam methane reforming and coal gasification inevitably releases large amounts of carbon dioxide. Thus, the hydrogen production techniques based on steam methane reforming and coal gasification cannot really solve the problem of greenhouse gas pollution and global warming. The increased amount of hydrogen production via water electrolysis is becoming a more and more urgent challenge.

The first research of water electrolysis can be dated back to 1789 [77]. Water electrolysis, also called water splitting, is the decomposition of water into oxygen and hydrogen gas driven by an electric current. This method can produce hydrogen with high purity (close to 100%). Generally, as shown in **Figure.2.2**, an

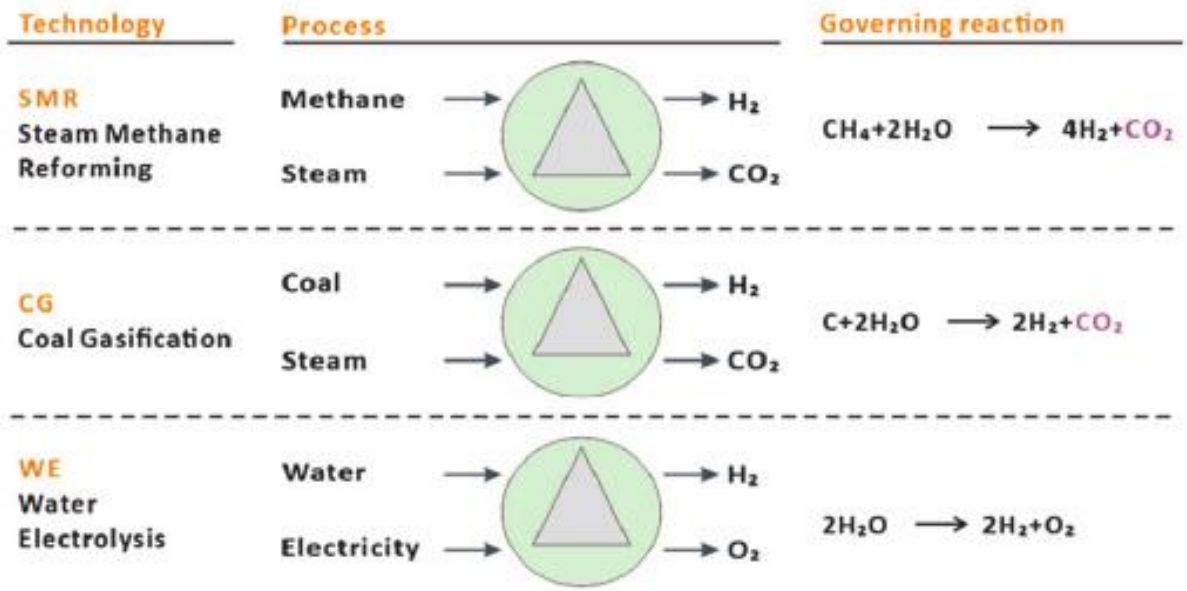

Figure 2. 1 Three typical pathways for industrial hydrogen production [1].

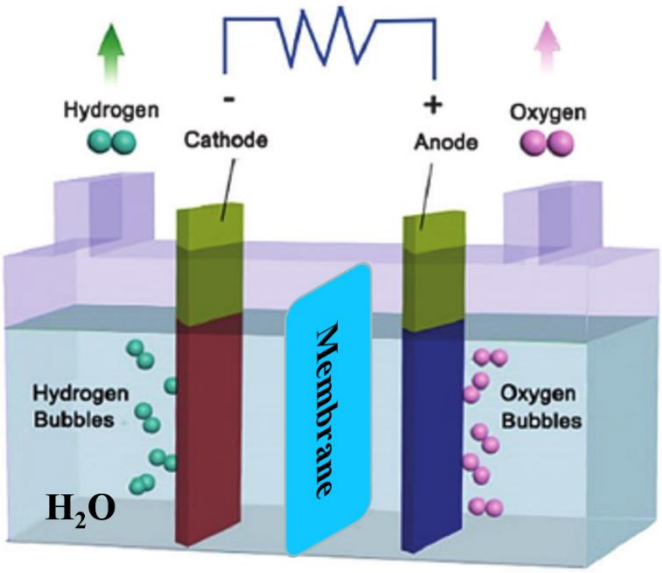

Figure 2. 2 Simplified schematic diagram of an electrolyzer [1].

electrolyzer consists of four component parts: an electrolyte (i.e., H_2O), a membrane, a cathode and an anode. Total reaction of water splitting can be described as the following equilibrium reaction [**Eq. (2.1)**]. The hydrogen evolution reaction (HER) and the oxygen evolution reaction (OER), as two half-reactions, occur at the cathode and anode, respectively [1]. Depending on the pH value, the water splitting half-cell reaction is described as shown below [**Eq. (2.2-2.5)**]:

Total reaction: $H_2O \rightarrow H_2 + 1/2\ O_2$ **Eq. (2.1)**

In acidic solution

Cathode (HER): $2\ H^+ + 2\ e^- \rightarrow H_2$ **Eq. (2.2)**

Anode (OER): $H_2O \rightarrow 2\ H^+ + 1/2\ O_2 + 2\ e^-$ **Eq. (2.3)**

In neutral and alkaline solutions

Cathode (HER): $2H_2O + 2\ e^- \rightarrow H_2 + 2\ OH^-$ **Eq. (2.4)**

Anode (OER): $2\ OH^- \rightarrow H_2O + 1/2\ O_2 + 2\ e^-$ **Eq. (2.5)**

2.1.2 Fundamentals of the hydrogen evolution reaction

The electrocatalytic hydrogen evolution reaction (HER), which is the reduction of aqueous protons by electrons passing through a catalyst to liberate H_2, is one of the crucial half-cell reactions of the electrochemical water splitting [12]. The HER basic mechanism is highly dominated by the pH value of the electrolyte. According to the Nernst equation under standard temperature and pressure (25 ºC, 1 atm), the Nernst potential referenced to a normal hydrogen electrode (NHE) can be reduced by increasing the pH value. However, when we use a relative hydrogen electrode (RHE) as reference, the Nernst potential can

be directly regarded as 0 V (vs. RHE) regardless of pH values of the electrolyte. In fact, the Nernst potential normally used to imply the thermodynamic equilibrium potential during electrochemical reactions occurs. The real HER usually requires extra energy to overcome the intrinsic activation barriers, which can be expressed briefly by the following equation[13]:

$$E = E_{HER} + i\,R + \eta$$

Where, E is the applied potential, E_{HER} is the standard reduction potential for an RHE reference (0 V *vs.* RHE), $i\,R$ is the ohmic potential drop of current flow in ionic electrolyte, and η is an excess potential (also called as overpotential) used to overcome the intrinsic activation barriers. The overpotential (η) is strongly related to the energy efficiency of the cathode, which can be optimized by the assistance of suitable HER electrocatalysts. For example, the overpotential of Pt, as an excellent cathode catalyst for HER, is close to zero.

In general, the HER can be explained by the Volmer-Heyrovsky or Volmer-Tafel mechanism. In acidic conditions, the first step of HER is described by the Volmer reaction [**Eq. (2.6)**] which means combination of a proton (H^+) and an electron (e^-) on an empty active site of the catalyst surface (A) to yield an adsorbed hydrogen atom (AH_{ads}). Subsequently, the formation of H_2 may occur via two different reaction pathways (Volmer-Heyrovsky or Volmer-Tafel mechanism). One possible pathway is the Heyrovsky reaction [**Eq. (2.7)**]: the adsorbed hydrogen atom (AH_{ads}) combines with a proton (H^+) and an electron (e^-) to evolve a hydrogen molecule (H_2). Another possible reaction is known as the Tafel reaction [**Eq. (2.8)**]: two adsorbed hydrogen atoms (AH_{ads}) combine on the catalyst surface to produce a hydrogen molecule (H_2). All above-mentioned reactions are described in detail as follows:

Volmer reaction: $A + H^+ + e^- \rightarrow AH_{ads}$ **Eq. (2.6)**

Heyrovsky reaction: $AH_{ads} + H^+ + e^- \rightarrow H_2 + A$ **Eq. (2.7)**

Tafel reaction: $AH_{ads} + AH_{ads} \rightarrow H_2 + 2\,A$ **Eq. (2.8)**

In alkaline conditions, the proton source is the water molecule instead of H^+ during the process of Volmer and Heyrovsky reaction. Besides, the Tafel plot calculated from the polarization curve can be used to infer the HER mechanism [78-79]. Ideally, in acidic solutions, when the reaction rate is limited by the electrochemical hydrogen adsorption (Volmer reaction), the Tafel slope reaches a high value of 120 mV dec^{-1}. On the other hand, if the rate-limiting step happens in the Heyrovsky or Tafel reaction, the Tafel slope is significantly reduced (30 mV dec^{-1}).

2.1.3 Non-noble metal based electrocatalysts

Suitable HER electrocatalysts are utilized on the cathode, which reduce the overpotential significantly, promote the reaction rate and increase the total cell efficiency. Thus, many researchers attempted to develop

highly active HER electrocatalysts. Ideal catalysts should have low Tafel slopes and a high exchange current density driven by a low overpotential. According to the above discussion, regardless of the HER mechanism, an adsorbed hydrogen atom (H_{ads}) should be produced on the electrocatalyst surface. The strength of the hydrogen-surface bond can be described by the free energy of hydrogen adsorption (ΔG_H). A volcano plot can be depicted by the exchange current density (i_0) for the HER versus the free energy of hydrogen adsorption [80]. As depicted in **Figure.2.3** [5], platinum-group metal based catalysts, such as Pt, Ru, Ir and their oxides, are at the summit of the volcano, indicating they have the highest activity for HER, due to their ultra-low hydrogen adsorption energy ($\Delta G_H \approx 0$). For the most effective electrocatalyst Pt [11], a current density of 10 mA cm^{-2} can be reached with an overpotential of only 30 mV, and its Tafel slope is around 30 mV dec^{-1}.

Unfortunately, the large-scale application of Pt-group electrocatalysts is seriously limited by its high cost and scarcity. Therefore, highly active HER alternative catalysts based on non-precious metals have aroused intense research interests [81]. According to the volcano plot, for metals on the left of Pt, the strength of the hydrogen-surface bond is too strong and blocks the active site, which obstacles the evolution of hydrogen. On the other hand, for metals on the right of Pt, their hydrogen-surface bond is too weak to yield a stable intermediate state. Transition metals and their compounds are promising candidates to replace noble-metal Pt-groups as HER electrocatalysts to produce H_2. The well-known electrocatalytically active transition metals mainly include iron (Fe), cobalt (Co), nickel (Ni), copper (Cu), molybdenum (Mo) and tungsten (W), while their compounds include carbides, sulfides, nitrides, phosphides and borides.

Miles and coauthors investigated the HER performance of 31 metals by cyclic voltammetric techniques, indicating that the catalytic activity order of non-noble metals is Ni >Mo > Co > W > Fe > Cu [82]. Moreover,

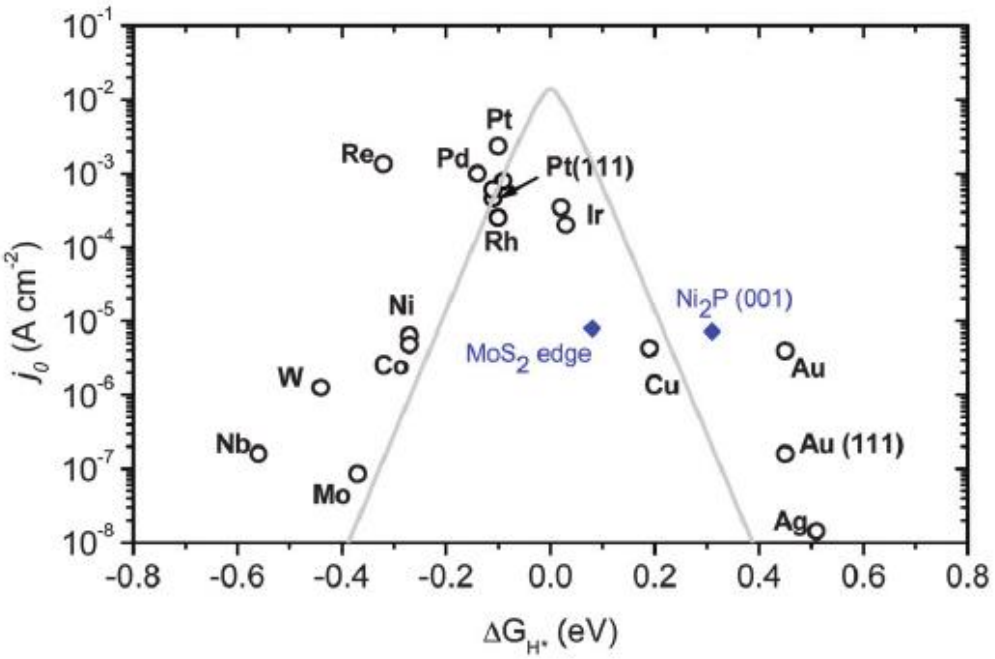

Figure 2. 3 A volcano plot of experimentally measured exchange current density as a function of the DFT-calculated Gibbs free energy of adsorbed atomic hydrogen [5].

for recent decades, transition metal-based alloys have been investigated widely for HER applications. Raj [83] reported the catalytic activity of several Ni-based alloys prepared by electrodeposition techniques. The results indicate their catalytic activity order as follows: NiMo > NiZn > NiCo > NiW > NiFe > NiCr, and among them the NiMo alloy also revealed the best stability. The Fe-based alloys are another typical transition metal-based catalyst, which can be used for water splitting cathode materials. Rosalbino et al.[84] prepared several Fe-based crystalline alloys, including $Fe_{90}Ce_{10}$, $Fe_{90}Sm_{10}$, $Fe_{90}Y_{10}$ and $Fe_{90}MM_{10}$ (MM: mischmetal), for the HER and found that $Fe_{90}MM_{10}$ showed the best electrocatalytic activity.

Transition metal carbides, such as tungsten carbide (WC, W_2C), and molybdenum carbide (Mo_xC_y), have been famously reported to exhibit catalytic activities for HER due to their d-band electronic density-of-state similar to that of Pt [24, 85]. Compared with the HER electroactivity of nine typical transition metal carbides, Regmi et al. found that the Mo_2C catalyst possesses the best electrocatalytic activity, followed by WC and V_8C_7 [86]. Transition metal dichalcogenides (MX_2; M: Mo, W and X: S, Se, Te) [87-89] are another type of transition metal compounds developed for the HER catalyst. For instance, the monolayered nanosheets of WS_2 was successfully prepared by lithium intercalation, and showed a very low overpotential for the HER [90]. Transition metal phosphides, as the promising transition metal based HER catalysts, were firstly reported by Rodriguez in 2005 [91]. Among of various transition metal phosphides, nickel phosphides and cobalt phosphides are considered to be more active than other materials [92]. Ni_2P [22] and CoP [93] exhibit excellent HER activity with low overpotentials of 130 and 85 mV, respectively for driving cathodic current densities of 20 mA cm^{-2} in acidic media.

Besides, recently metal-free catalysts are considered as another promising low-cost non-noble metal based electrocatalyst for the HER. Researchers attempted to utilize heteroatoms (such as N, B, P and S) to substitute carbon in carbon-based materials, which can adjust its electronic structure and chemical/electrochemical properties. For example, Qiao and coauthors [94] designed and synthesized N, P, S, B, O, F doped or dual-doped graphene as metal-free electrocatalysts for the HER. Besides graphene, other heteroatoms-doped carbon materials, such as CNTs [95], hexagonal carbon [96], activated carbon [97] and carbon nitride (C_3N_4) [17], were also reported to show suitable electrocatalytic properties for the HER.

2.1.4 Molybdenum-based HER electrocatalysts

In this Ph.D. thesis, we mainly focus on Mo-based HER electrocatalysts. Thus, in the following, Mo-based HER electrocatalysts, as an important typical transition-metal electrocatalyst, are introduced in more detail. In general, Mo-based HER electrocatalysts mainly include molybdenum carbide (Mo_xC_y) [19-20], molybdenum disulfide (MoS_2) [98-100], molybdenum boride (MoB) [20] and molybdenum phosphide (MoP) [101-103]. Leonard et al.[19] synthesized four different phases of molybdenum carbides (α-MoC_{1-x}, β-Mo_2C, μ-MoC and γ-Mo_2C) and compared their electrocatalytic activity, indicating that hexagonal-Mo_2C has the best activity followed by γ-Mo_2C. In the early 1970s [104], the electrochemistry and photochemistry of MoS_2 layered crystals have been proven by Tributsch et al., while, until 2005, its good HER activity was discovered by Nørskov and

co-workers [105]. Since then, various materials and electrode preparation methods have been reported for the optimization of the MoS_2 catalysts [106-107]. Compared with other Mo-based HER electrocatalysts, the time to develop MoP for the HER was relatively short. Several efficient strategies have been exploited, which make MoP to achieve an electrocatalytic performance comparable to other well-studied HER electrocatalysts [101-103, 108-109]. For instance, Xiao and co-workers [101] reported that MoP exhibits high activity towards HER in both acid and alkaline media even in bulk form, and it achieved a current density of 30 mA cm^{-2} at a potential of 180 mV (*vs*. RHE).

Furthermore, there are several reported approaches that can be used to further optimize the electrocatalytic activity of Mo-based HER electrocatalysts, including five main aspects [1]: (i) increasing the number of exposed active sites; (ii) enhancing the reactivity of active sites; (iii) improving the electrical contact to active sites; (iv) doping suitable heteroatoms into the lattice of Mo-based HER electrocatalysts; (v) combining Mo-based HER electrocatalysts with some high conductive carbon supports, such as CNTs and graphene. Compared with bulk electrocatalysts, the electrocatalysts with unique nanostructure (such as nanosheets [110] , nanowires [111], nanorods [112] or nano/mesoporous structure [113]) usually have larger specific surface areas (SSA) and higher number of exposed reactive sites. For example, **Figure.2. 4** shows

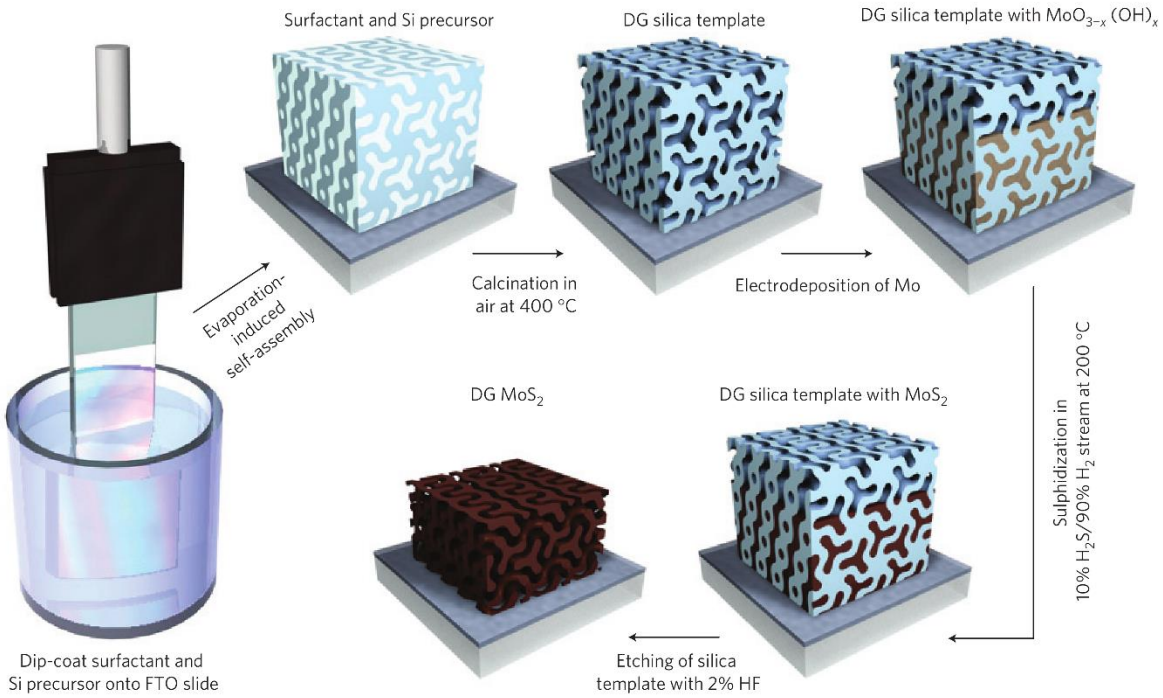

Figure 2. 4 Synthesis procedure and structural model for mesoporous MoS_2 with a double-gyroid morphology **[113]**.

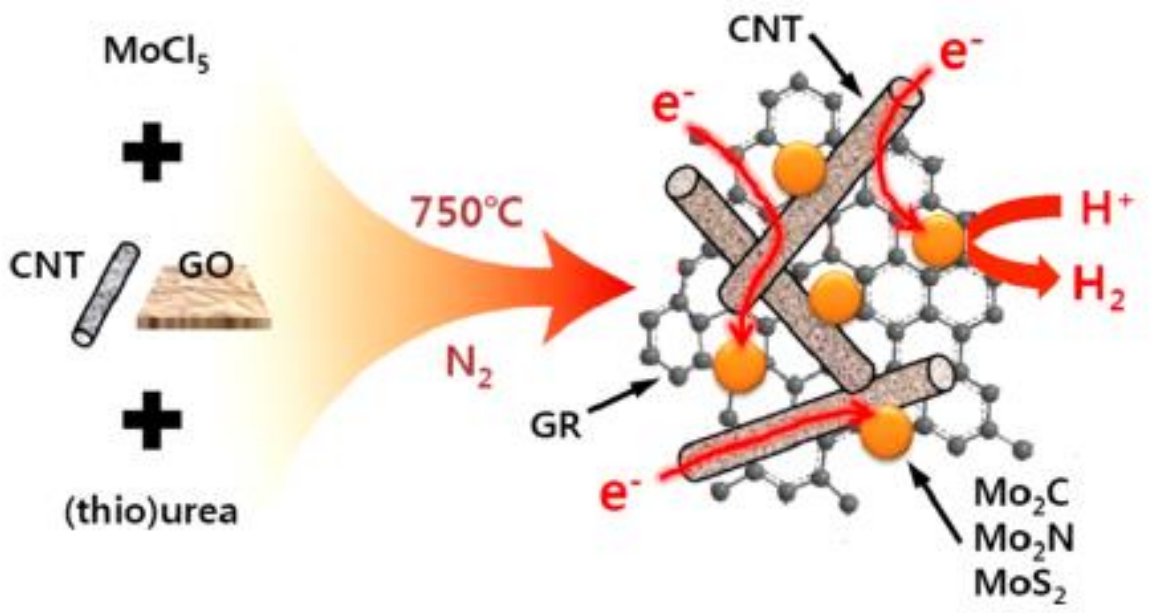

Figure 2. 5 Schematic illustration of synthetic method and resultant Mo-compounds on CNT-GR hybrid support for hydrogen evolution [31].

the synthesis procedure and structural model for mesoporous MoS_2 prepared by Jaramillo's group [113]. The high surface curvature of the catalyst´s mesostructure exposes a large fraction of edge sites leading to excellent activity for HER. Metal/nonmetal-doping is the second main method, which can adjust the structure and HER activity of Mo-based electrocatalysts effectively. Specifically, metal-doping elements include Co, Ni, V and Li [114-116], while O [117] , N [118] and P [119] , as the nonmetal-doping elements, were introduced to enhance the catalytic activity of Mo-based electrocatalysts. Additionally, an alternative strategy to increase the number of active sites is introducing carbon supports (such as CNTs [29, 31, 120-121] or graphene [31, 122-123]) with nanostructure and high surface area, during the preparation of Mo-based electrocatalysts. For example, Youn's group [31] synthesized a series of Mo-based nanocrystals (Mo_2C, Mo_2N, and MoS_2) on CNT-GR composites by a modified urea-glass route (**Figure.2.5**). The results reveal that Mo_2C/CNT-GR exhibits much better HER activity than Mo_2N/CNT-GR and MoS_2/CNT-GR. In detail, the overpotentials (η_{10}) driving current densities of 10 mA cm^{-2} of the Mo_2C/CNT-GR is 130 mV, while the η_{10} values of Mo_2N/CNT-GR and MoS_2/CNT-GR are 186 and 255 mV, respectively. In addition, they also proved that the CNT-GR hybrid as a support plays a crucial role to enhance the activity of Mo-compounds by alleviating the aggregation between the Mo-based nanocrystals, providing a large surface area to contact with electrolyte, and facilitating the electron transfer.

Finally, the electrochemical performances of some representative Mo-based HER electrocatalysts are summarized in **Table 2.1**.

Table 2. 1 The HER performance of some representative Mo-based electrocatalysts.

Catalyst	Current density (j, mA cm^{-2})	Overpotential at the corresponding current density (mV)	Tafel Slope (mV/dec)
Defect-rich MoS_2 ultrathin nanosheet [110]	13	200	50
Mo_2C-Graphene composites [32]	10	150	57
Mo_2C/CNT [29]	10	152	65
MoB microparticles [20]	20	~225	55
MoP nanoparticles [102]	10	125	54
Mo_2C nanowires [111]	60	200	53
MoC_x nano-octahedrons [124]	10	142	53
Mo_2S@N-doped carbon nanoboxes [125]	10	165	55
Mo_2C nanotubes [126]	10	172	62
Amorphous MoS_x [87]	10	540	40
Mo_2C@NC [27]	10	124	60
Mo_2C nanoparticles [127]	10	198	58
$Mo_{0.06}W_{1.94}C$/CB [128]	10	220	/
Fe-doped β-Mo_2C [129]	10	290	/

2.2 Electromagnetic absorption materials

2.2.1 General background

Microwaves are identified as a form of electromagnetic (EM) wave at frequencies between 300 MHz and 300 GHz (wavelengths: 0.01-1m), which have been used extensively in commerce, industry and defense applications [130]. For example, the electromagnetic wave at frequencies of 1 and 100 GHz normally is applied in radio-frequency engineering including mobile phones, radios and Wi-Fi. In recent decades, a growing number of demanding applications of electromagnetic wave rely on the unique properties of electromagnetic materials [131]. The incidence of EM wave obeys the laws of optics, including three basic processes: reflection, absorption and transmission. Specially, for dielectric materials as an electrical insulator, when EM wave is incident on the surface, the bound charges generate a displacement current. Positive charges are displaced in the direction of the field while negative charges shift in the direction opposite to the field. This process is called dielectric polarization. During the process of dielectric polarization, the dissipation of electromagnetic energy is called dielectric loss. Electromagnetic properties of a dielectric material are characterized by a complex permittivity ε, which can be expressed as follows [**Eq. (2.9)**]:

$$\varepsilon = \varepsilon' - j\varepsilon'' \qquad \textbf{Eq. (2.9)}$$

where ε' and ε'' represent the real part and imaginary part of the permittivity, respectively. Moreover, based on the Debye polarization relaxation equation, the loss tangent values can be used to evaluate the dielectric loss of materials in the associated frequency range, and it can be described in detail as follows [**Eq. (2.10)**] [35]:

$$\tan\delta = \frac{\varepsilon''}{\varepsilon'} = \frac{(\varepsilon_s - \varepsilon_\infty)}{\varepsilon_s + \varepsilon_\infty \omega^2 \tau^2} \qquad \textbf{Eq. (2.10)}$$

where ε_s, ε_∞, ω and τ are the static dielectric constant, optical frequency dielectric constant, frequency and relaxation time of polarization, respectively. According to the value of the real part (ε') and imaginary part (ε'') of the permittivity, dielectric materials can be divided into three categories: (i) electromagnetic wave transparent materials with low ε' (1-5) and ε'' (tan δ ≦ 0.01); (ii) electromagnetic wave absorption (EWA) materials with low ε' (5-20) and intermediate ε'' (1-10); (iii) electromagnetic wave shielding materials with high ε' and high ε''. The EM wave transmission model for different dielectric materials are described in **Figure.2.6**

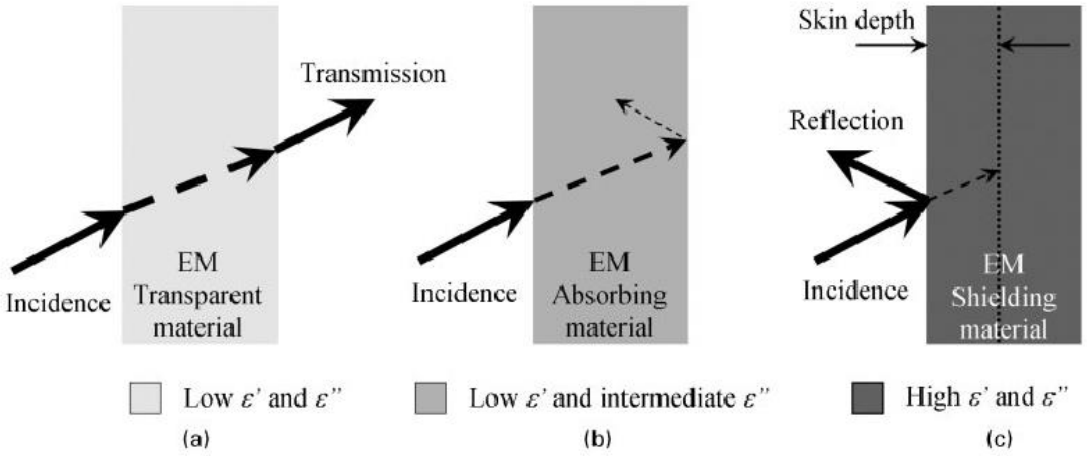

Figure 2. 6 Electromagnetic (EM) wave transmission model for materials with different complex permittivity. (a) EM wave transparent materials; (b) EM wave absorption materials; (c) EM wave absorption materials [131].

2.2.2 Mechanisms of electromagnetic wave absorption materials

When electromagnetic wave (EMW) is incident on the surface of materials, EMW absorption materials can transform electromagnetic energy into internal energy of the absorber (such as thermal energy). In general, EM absorption materials can be used to minimize various EM reflection and interference, due to their strong ability of EM waves absorption. The United States Naval Research Laboratory analyzed the reflected wave of the materials placed on a metal panel by arch free-space measurement method [**Figure.2.6** (a)], which can be used to evaluate absorption properties of EMW absorption materials. Furthermore, the reflection coefficient (RC or RL or reflectivity), as a critical parameter, was introduced to describe the EM absorbing property of the materials and is defined by the following equation:

$$\mathrm{RC} = 10\log_{10}\left(\frac{P_R}{P_I}\right)(\mathrm{dB}) \qquad \textbf{Eq. (2.11)}$$

where P_I and P_R refer to the incident power and received power of an EM wave, respectively. Specifically. RC < -10 dB means that more than 90 % of the EMA energy is absorbed while less than 10% of the energy is reflected.

When the EM wave is incident into a multilayer microwave absorber that consists of i layers of different materials backed by a perfect electric conductor (such as a metal plate) [**Figure.2.7 (b)**], the wave impedance (Z_i) of the i-th layer is expressed based on the transmission-line theory [131-133]:

$$Z_i = \eta_i \frac{Z_{i-1} + \eta_I \tanh(\gamma_i d_i)}{\eta_i + Z_{i-1}\tanh(\gamma_i d_i)} \qquad \textbf{Eq. (2.12)}$$

$$\eta_i = \eta_0\sqrt{\mu_i/\varepsilon} \qquad\qquad \gamma_i = j2\pi f\sqrt{\mu\varepsilon}/c$$

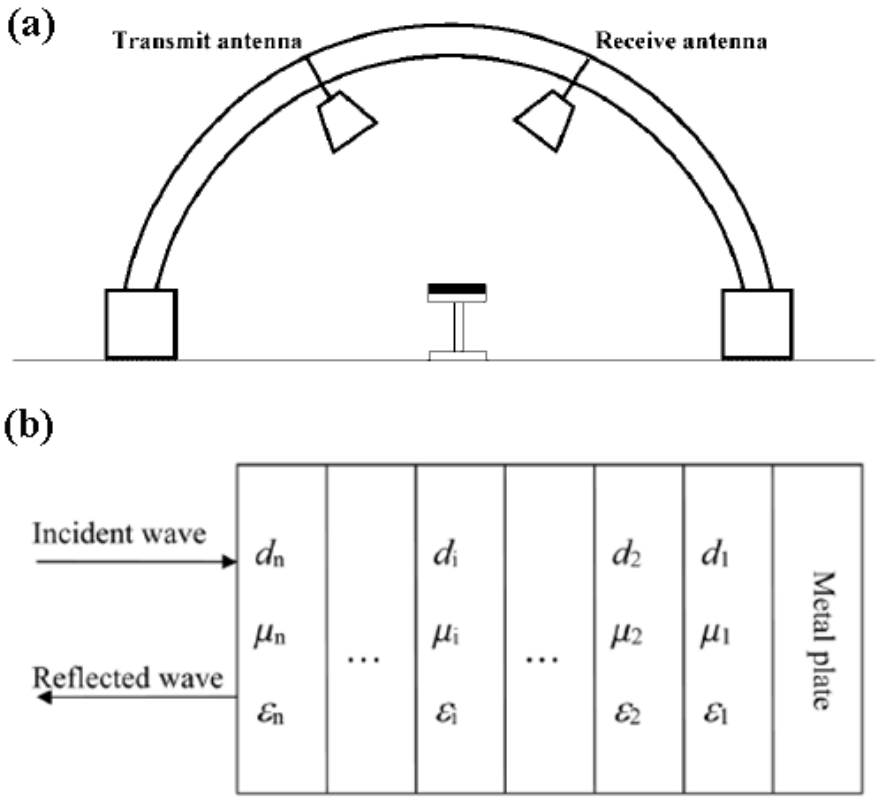

Figure 2. 7 Schematics of (a) Naval Research Laboratory arch free-space measurement method and (b) a multilayer microwave absorber with a normally incident wave [3].

where d_i, μ_i, and ε_i denote the thickness, relative magnetic permeability and permittivity of the i-th layer, respectively. η_0 is the characteristic impedance of the free space; f is frequency of microwaves; c is the speed of light in free space; μ_i and ε_i are the relative complex permeability and permittivity of the i-th layer, respectively. Thus, the reflection loss (RL) of normal incident electromagnetic wave at the absorber surface is expressed as follow:

$$\mathrm{RL} = 20\log|\Gamma| = 20\log\left|\frac{Z_n-\eta_0}{Z_n+\eta_0}\right| \qquad \textbf{Eq. (2.13)}$$

where Γ is the reflection coefficient. Specifically, for the metal back-panel model comprising a single layer of absorber, the reflection loss can be given as [133-134]:

$$\mathrm{RL} = 20\log\left|\frac{\sqrt{\frac{\mu}{\varepsilon}}\tan h\left(j\frac{2\pi fd}{c}\sqrt{\mu\varepsilon}-1\right)}{\sqrt{\frac{\mu}{\varepsilon}}\tan h\left(j\frac{2\pi fd}{c}\sqrt{\mu\varepsilon}+1\right)}\right| \qquad \textbf{Eq. (2.14)}$$

Here we can see that the high-performance of EW absorption materials is strongly dependent on the combination of the magnetic permeability (μ) and the permittivity (ε) satisfying the impedance matching condition [135]. Moreover, the attenuation ability for the EM wave normally can be evaluated by the attenuation constant α, and it is defined by the following equation [136-137]:

$$\alpha = \frac{\sqrt{2}\pi f}{c} \times \sqrt{(\mu''\varepsilon'' - \mu'\varepsilon') + \sqrt{(\mu''\varepsilon'' - \mu'\varepsilon')^2 + (\mu'\varepsilon'' - \mu''\varepsilon')^2}} \quad \textbf{Eq. (2.15)}$$

Accordingly, the α value depends on i) the complex magnetic permeability (μ' and μ''), ii) the permittivity (ε' and ε'') and iii) the frequency (f) of the incident wave.

2.2.3 Typical types of EWA materials

There has been a long history of the research on electromagnetic wave absorption materials, which can trace back to World War II (1940s) when Germans attempted to cope with the situation that aircrafts were detected by early radar sets [138]. In decades of development, electromagnetic absorbing materials are expected to have broad bandwidth, minimum RL and small thickness or light weight [130]. According to the above-discussed absorption mechanisms, EWA materials can be divided into two categories: magnetic-loss type and dielectric-loss type.

For magnetic-loss materials, the EM energy can be mainly attenuated by magnetic hysteresis, magnetic domain-wall resonance, eddy current and natural resonance [139-140]. The typical magnetic-loss materials mainly include spinel ferrites (Fe_3O_4) [141], ferromagnetic metal particles (Fe/Co/Ni) [142-143], carbonyl iron [144] and Ba/Sr-based hexaferrites [145-146]. In general, the traditional magnetic-loss materials exhibit better EM absorbing performance at low frequency range, because their complex permeability will be remarkably decreased by the Snoek's limit (Fe_3O_4) or eddy current phenomenon (Fe/Co/Ni) in the GHz range [147]. Besides, magnetic-loss type EMA materials cannot be applied at high temperature, because metals lose their permanent magnetic properties above their Curie temperature [148].

On the other hand, the dielectric-loss materials possess EMA performance due to the interfacial polarization and high dielectric loss in the microwave frequency range. The real part (ε′) and imaginary part (ε″) of the permittivity reveal the polarization capacity and dielectric loss ability of the absorber material, respectively [48]. According to the Debye theory, the real part (ε') and imaginary part (ε″) of the permittivity can be described as follow [149]:

$$\varepsilon' = \varepsilon_\infty + \frac{\varepsilon_S - \varepsilon_\infty}{1 + [\omega\tau(T)]^2} \quad \textbf{Eq. (2.16)}$$

$$\varepsilon'' = \frac{\varepsilon_S - \varepsilon_\infty}{1 + [\omega\tau(T)]^2}\omega\tau(T) + \frac{\sigma(T)}{2\pi\varepsilon_0 f} \quad \textbf{Eq. (2.17)}$$

where ε_s is the static relative permittivity, ε_∞ is the relative permittivity at high-frequency limit, ω is the angular frequency of the incident electromagnetic wave and τ(T) is the temperature-dependent relaxation time of the polarization. σ(T) is the temperature-dependent electrical conductivity, ε_0 is the permittivity of vacuum (8.854×10^{-12} F/m) and f is the frequency of the incident electromagnetic wave. Although temperature can affect the value of σ(T), the dielectric-loss materials without a Curie temperature means

that they can be strongly considered as candidates to be utilized in high temperature environments. Moreover, the typical dielectric-loss materials mainly include carbon black [132], CNTs [150], graphene [151], carbon fiber [149], silicon carbide [152] and some conductive polymers (e.g., polypyrrole [153]).

Furthermore, in order to attain a suitable imaginary part (ε'') of the permittivity and dielectric loss value (tan δ), composite materials containing a conductive secondary phase and/or micro-meter-sized pores are becoming increasingly popular. In case of composites with conductive fillers (such as carbon or other high conducting components), the electronic transport could be approximated by the free electron theory. Therefore, based on the Debye theory [**Eq. (2.17)**], ε'' can be expressed briefly by the equation as follows [149, 154]:

$$\varepsilon'' \approx \frac{\sigma}{2\pi f \varepsilon_0} \qquad \textbf{Eq. (2.18)}$$

Thus, the enhanced electric conductivity (σ) of the composites can lead to the increase of ε″ and tan δ. Nanocarbon fillers as conductive secondary phase such as CNTs and RGO, were widely investigated to modify polymer/ceramic based materials [50-51, 155-156]. For instance, Fan et al. [156] prepared a phenol-formaldehyde cement-based absorber using ball-milled flaky graphite, leading to a maximum absorption of 25.5 dB at 14.5 GHz and an absorption bandwidth of 2.9 GHz. In general, polymer based EMA materials cannot be used for structural applications at high temperatures, due to their poor thermal stability and mechanical properties [157]. Therefore, ceramic based EMA materials for electromagnetic wave absorption will be furfure discussed in the following part.

Besides, EMA materials with a single loss mechanism cannot exhibit enhanced EMA performance due to the lack of well impedance matching [158]. Therefore, composite materials with mutual electromagnetic loss mechanisms (magnetic-loss and dielectric-loss) were widely investigated to further improve the microwave absorption ability in a wide frequency range. A series of magnetic/dielectric composites, such as CoS_2/rGO [159] , $MnFe_2O_4$/rGO [160], NiO/rGO [161], were reported recently. For example [162], as shown in **Figure 2. 8**, Jian and co-workers developed the hydrothermal method coupled with the chemical catalytic vapor deposition (CCVD) technology to design Fe_3O_4@C (FC) and Fe-Fe_3O_4@C (FFC) hybrid nanorings for enhanced microwave absorption performance. The resulted FFC hybrid nanorings have a minimum RL value of -32.9 dB at 17.1 GHz, whereas the absorption bandwidth (RL < -10 dB) is from 5.2 to 18 GHz, which can be explained by the microwave absorption mechanisms including natural ferromagnetic resonance, eddy current effect, dipole relaxation polarizations and interfacial polarization.

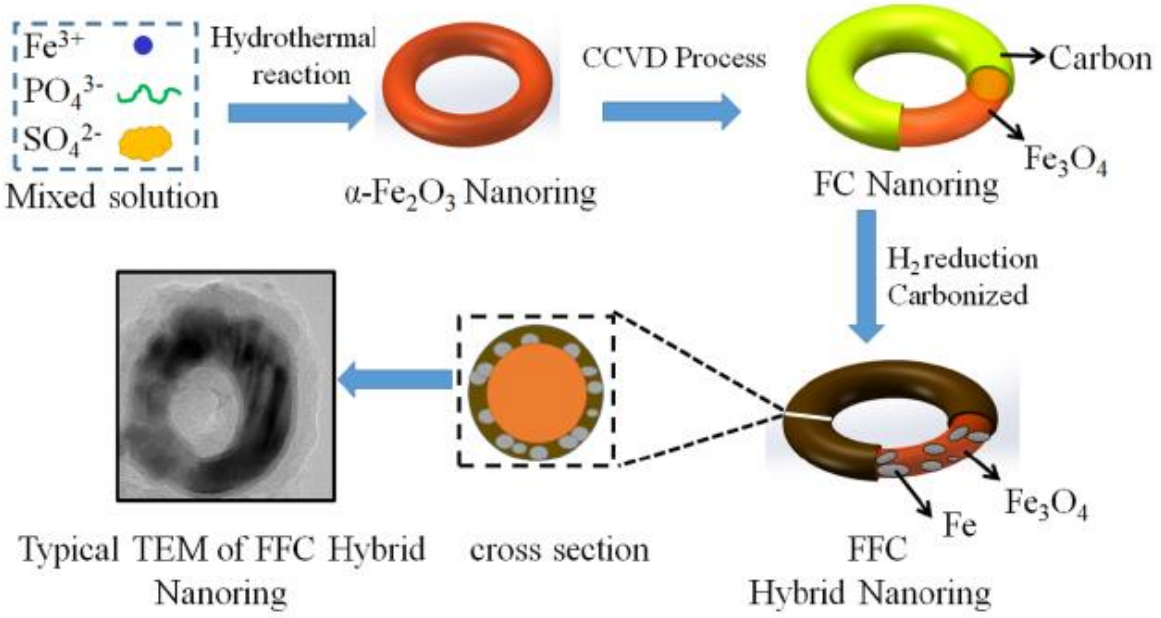

Figure 2. 8 Schematic presentation of the synthesis process of α-Fe_2O_3, FC, and FFC hybrid nanorings [162].

2.2.4 Ceramic based composites towards EMA materials

When EMA materials are applied in harsh environments (e.g., at high-temperatures or in aggressive media), they are required to possess excellent oxidation resistance, high melting point and high chemical/thermal stability [40-42]. As discussed above, magnetic-loss type EMA materials and polymer-based dielectric-loss type EMA materials are limited by the Curie temperature and low melting/softening point, respectively. Thus, they are usually utilized as low temperature EM absorbers. Ceramics with low density can offer superior effectiveness in the gigahertz frequency range, as well as excellent stability in high-temperature, corrosive and oxidizing atmospheres. In the last decade, ceramics and their composites have been considered as an important candidate EMA materials used in various environments, particularly under high-temperature conditions. Silicon carbide (SiC), silicon dioxide (SiO_2) and silicon nitride (Si_3N_4) are promising candidate materials with applicable complex permittivity ($\varepsilon' < 9$) for EMA applications at high temperature, due to their high thermal and chemical stability, high hardness and strength. However, pure ceramics only exhibit limited EM absorption capability [44, 163]. For optimizing the real part (ε') and imaginary part (ε'') of the permittivity, ceramic-based EM absorption materials are designed as composites composed of an electrically loss phase (A phase) embedded in an electrically insulating ceramic matrix (B phase), and sometimes there is an intermediate phase (C phase) between A and B phase. The typical A/B type ceramic-based composites include carbon fiber/SiO_2 [149], NiO/SiC [43], CNTs/SiO_2 [157, 164], RGO/SiO_2 [148], C/SiC [165] , $ZrN_{0.4}B_{0.6}$/SiC [166] and pyrolytic carbon/ Si_3N_4 [167], while some A/B/C type ceramic-based composites, such as SiC/Si_3N_4/carbon foams [168] and SiC/HfC_xN_{1-x}/C [54], were also reported. Among them, Jian et al. [166] prepared the heterogeneous $ZrN_{0.4}B_{0.6}$/SiC nanohybrid via combined

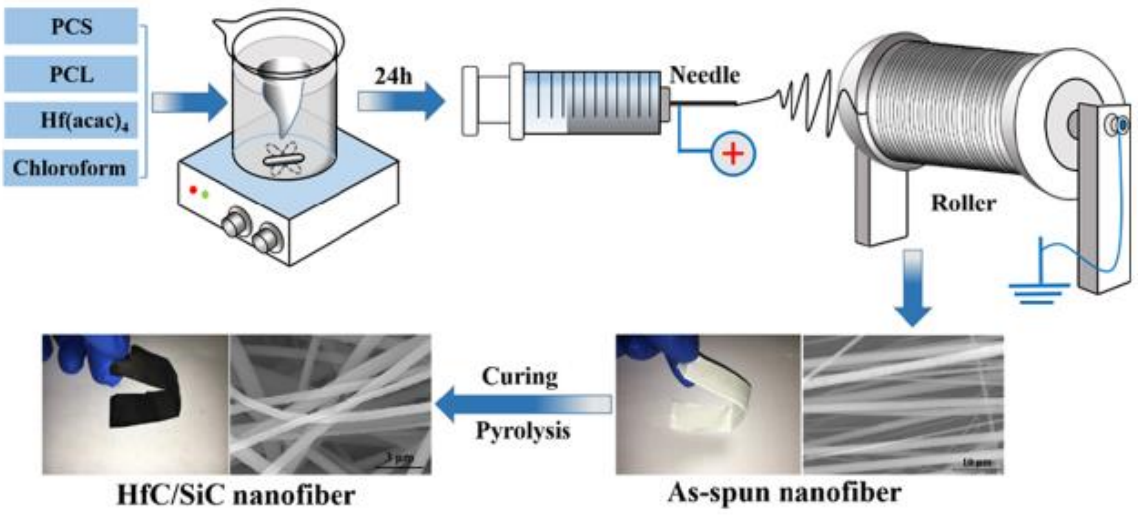

Figure 2. 9 Schematic illustration of the fabrication process of HfC/SiC nanofiber mats. The insets on the right and left are digital photos and SEM images of the as-spun nanofiber mats and pyrolyzed HfC/SiC nanofiber mats, respectively [48].

catalytic chemical vapor deposition (CCVD) and chemical vapor infiltration (CVI) processes, which exhibited enhanced microwave absorption ability with a minimum RL value of -50.8 dB.

Particularly, polymer-derived ceramics (PDCs) as a novel technology for the fabrication of ceramic-based EMA materials has attracted much attention in the past several years. The PDC approach has some unique advantages: (i) ceramic matrix (B phase) with a lower ε′ is preferable for impedance matching; (ii) the dielectric loss phase (A phase) can be dispersed homogeneously in a ceramic matrix [55]; (iii) the in-situ formed free carbon with high electric conductivity can increase the ε'' value of the composites and enhance the dielectric loss [74, 169]; (iv) PDC approach via different shaping techniques can fabricate ceramic based EMA with various shapes (e.g., monoliths, coatings, fibers and porous parts) [58]. As an example [48], **Figure 2.9** shows the fabrication process of HfC/SiC nanofiber mats via a combined PDC route and electrospinning technique. The HfC/SiC nanofiber mats exhibit a high flexibility and outstanding microwave absorption properties, and it can reach a minimal RL of -33.9 dB at 12.8 GHz. Besides, other typical ceramic-based EMA materials prepared by the PDC route include Co/SiC [170], n-SiC/SiOC [154], Pd_2Si/SiCN [171], SiC/HfC_xN_{1-x}/C [54] and RGO/SiCN [172].

Finally, the EMA performance of some representative ceramic based EMA materials are summarized in **Table 2.2**.

Table 2. 2 The EM absorbing performance of some representative ceramic based EMA materials.

Sample	Optimum thickness (mm)	RL_{min} (dB)	Effective Absorption Bandwidth (GHz)
CNT/SiC [173]	2.00	-47.7	3.4
$ZrN_{0.4}B_{0.6}$/SiC [166]	3.05	-50.8	2.8
SiC/Fe_xO_y EGL [174]	2.00	-41.8	6.58
SiC/C NCs [175]	2.08	-51.53	7.2
SiC/C Foam [176]	3.60	-51.58	10.83
NiO@SiC [43]	2.00	−46.9	4.2
SiC/$HfC_xN_{1-x}C_x$/C [54]	2.97	−47	3.6
Graphene/SiC [52]	3.00	−19.6	4.2
HfC/SiC [48]	3.00	−33.9	7.4
n-SiC/SiOC [154]	2.30	-61	3.5
CNTs/SiBCN [177]	2.50	-32	3

2.3 Polymer derived Si-based ceramics

2.3.1 General background

Polymer derived ceramics denoted commonly as PDCs is a term for advanced ceramic materials derived from preceramic polymers. A variety of preceramic polymers consist of Si-based polymers with the general composition:

$$[R^1R^2Si\text{-}X\text{-}]_n$$

The group (X) of the polymer backbone represents different type of Si-based polymers such as poly(organosilanes) with X = Si, poly(organocarbosilanes) with X = CH_2, poly(organosiloxanes) with X = O, poly(organosilazanes) with X = NH, and poly(organosilylcarbodiimides) with X = [N=C=N]. The substituents R^1 and R^2 at the Si atoms are commonly H and/or organic groups and can be changed to adjust the viscosity, chemical/thermal stability and solubility of the preceramic polymer. Besides, the functional

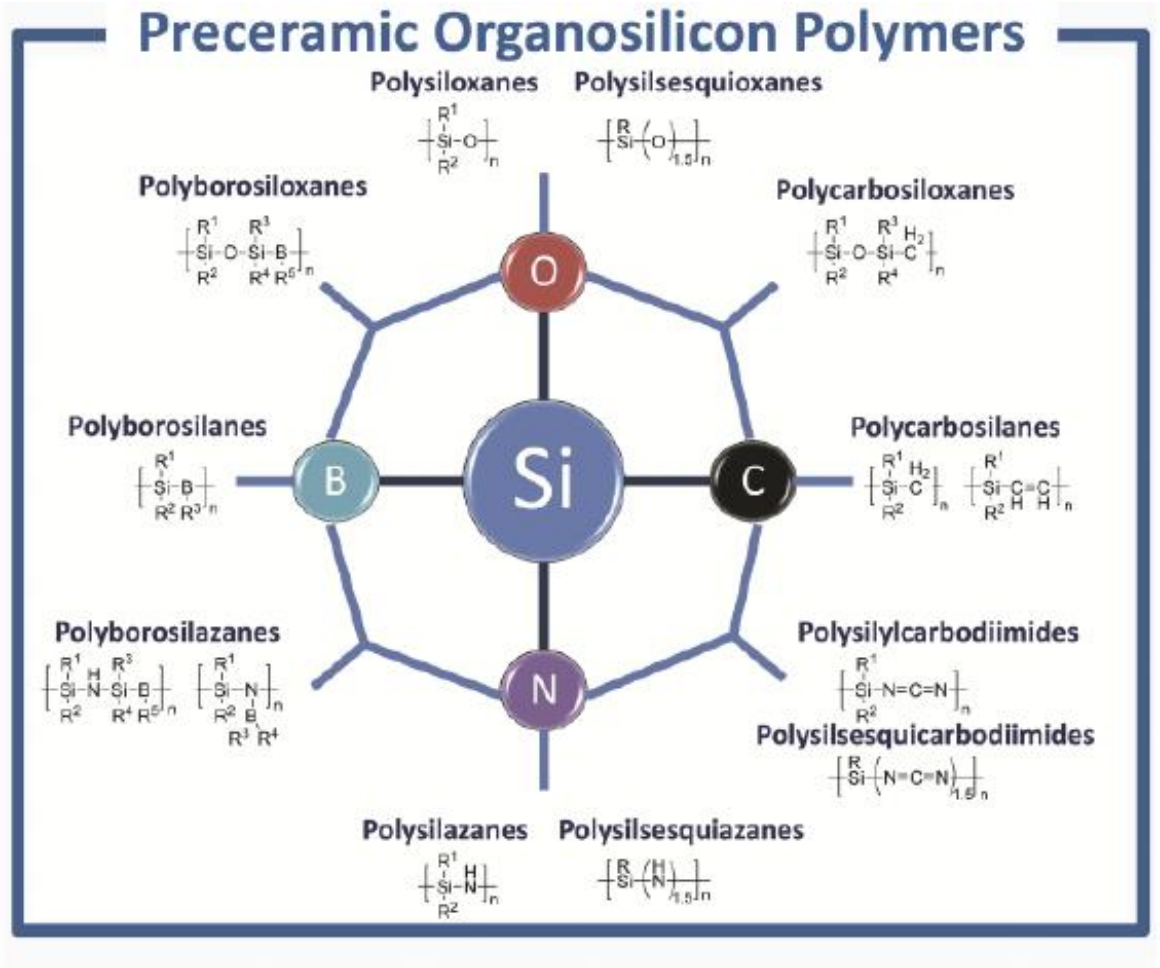

Figure 2. 10 Main representative classes of Si-based preceramic polymer [58].

group R also controls the carbon content of the final ceramic. In the early 1960s, silicon based PDCs have been synthesized directly by the pyrolysis of organosilicon polymers [178]. The PDC route for the fabrication of Si-based advanced ceramic materials includes four typical steps: (i) synthesis of preceramic precursors; (ii) shaping and crosslinking; (iii) ceramization and (iv) crystallization. Main representative classes of Si-based preceramic polymer are summarized in **Figure 2.10** [58].

Among them, the commercially available allylhydridopolycarbosilane (AHPCS, SMP10) produced by Starfire Systems (Schenectady, NY) were used as the starting material for the synthesis of SiC-based ceramics in this this Ph.D. work. Compared with traditional ceramics, one unique technological advantage of PDCs is that preceramic precursors can be shaped into different components such as coatings, fibers and aerogels [179-180]. After shaping, cross-linking can be achieved by different means. Thermal cross-linking is the most important curing step and involves suitable functional groups (e.g., Si-H, Si-OH, or Si-vinyl functionalities) which enable the formation of a thermoset via condensation or addition reactions. Crosslinking occurs spontaneously, typically, below 200 °C, while additional catalysts can decrease the temperature of the cross-linking reactions [181-182]. Besides, other cross-linking methods most used were oxidative curing [183], γ-radiation or e-beam curing [184] and UV curing [185-186]. Subsequently, the cured

preceramic polymers have to be converted into ceramics via the decomposition or elimination of organic moieties (such as methyl, phenyl, vinyl groups) and hydrogen. This conversion is denoted as the polymer-to-ceramic transformation or ceramization, which is almost completed at about 1000 °C. Then, at elevated temperatures (above 1100 °C), the initial amorphous network of the formed ceramics starts to transform to the local crystallization of the emerged phases. The chemical bonding is redistributed, resulting phase separation and finally leading to nucleation and growth of nanocrystals. Crystallization of the PDCs often is associated with decomposition, leading to a release of gaseous by-products such as CO, SiO, or N_2 and others [58].

2.3.2 Polymer-derived ceramic nanocomposites (PDC-NCs)

Nanocomposite materials can be defined as consisting of at least two Gibbsian phases, one of them being nanoscaled (less than 100 nm) [4]. In the last three decades, extensive research has been carried out to investigate the synthesis and properties of polymer-derived ceramic nanocomposites (PDC-NCs), which are synthesized starting from suitable single-source precursors and subsequent polymer-to-ceramic conversion to obtain amorphous single-phase ceramics. At temperatures ranging from 1000 to 1800 °C, phase separation processes eventually occur to yield bi- or multiphase ceramic nanocomposites. In a first step, e.g. polycarbosilanes (PCS) can be chemically modified by their reaction with molecular transition

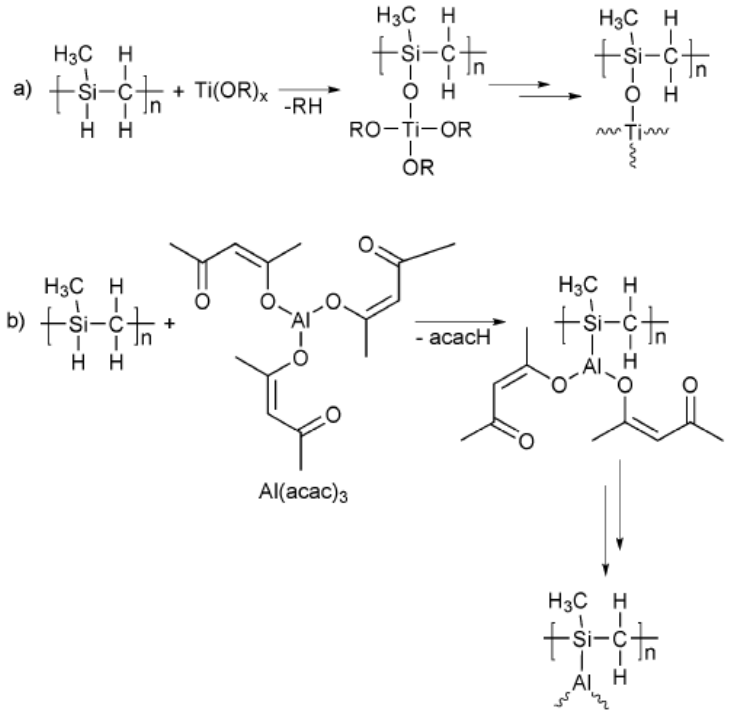

Figure 2. 11 Chemical modification of PCS: (a) with metal alkoxides (as for titanium (IV) n-propoxide, R = propyl) and (b) with metal acetyl acetonate complexes (as for aluminium (III) acetyl acetonate**) [4].**

metal compounds to obtain a so-called single-source precursor. There are two reaction pathways of PCS with metal-organic compounds shown in **Figure 2.11.** As shown in **Figure 2.11** (a), the reaction of PCS with metal alkoxides, such as aluminum, titanium and zirconium alkoxide, form Si-O-M bonds and evolve alkanes [187-189]. The reaction of PCS with metal acetyl acetonates (M = Al, Zr) forms Si-M bonds and release acetyl acetone [190-191] [**Figure 2.11** (b)]. After cross-linking (100-400 ℃) and ceramization (up to 1000-1400 ℃), polymer-derived ceramics are amorphous materials which persist up to very high temperatures. In general, PDCs remain amorphous up to temperatures ranging from 1000 to 1800 ℃, basically depending on the chemical composition. In the case of Hf-modified and polymer-derived SiOC [192], samples annealed at 1300 ℃ were found to exhibit small tetragonal HfO_2 precipitates of 5-10 nm in diameter finely dispersed throughout the amorphous SiOC matrix. Moreover, due to their unique microstructure, PDC-NCs present excellent behavior in hostile environments (high-temperatures or oxidative/corrosive conditions) and interesting functional properties (e.g. optical, electrical, and magnetic properties) for applications such as high temperature sensors, micro glow plugs and electrochemical devices [193-196].

2.3.3 Functional applications of polymer derived Si-based ceramics

Because of their physical-chemical and thermomechanical properties as well as their ability of being shaped using a wide variety of processing methods, PDCs have been explored for several applications mainly including fibers, ceramic–matrix composites (CMCs), highly porous components and coatings. The oldest and most successful commercial application of preceramic polymers is the ceramic fiber technology which can be applied as components for CMCs. In order to maintain good mechanical properties (tensile strength: 2.6-3.3 GPa) at high temperatures, the oxygen content of the ceramic fiber should be decreased to less than 0.5 wt% [197]. Initially numerous case studies are mainly focused on the high-temperature mechanical applications of polymer-derived dense bulk materials and fibers with low porosity. Recently, nano powders and micro/mesoporous PDCs with high surface area were applied in catalytic engineering and liquid/gas separation processes [61-63]. For example, Hojamberdiev and co-workers [63] reported that polymer-derived mesoporous SiOC/ZnO nanocomposite for water decontamination was prepared by a simple mechanical incorporation of ZnO nanopowders into the commercial vinyl-functionalized polysiloxane followed by pyrolysis at 700 °C for 2 h. The adsorption and photocatalytic properties of the as-prepared samples were evaluated by measuring the decrease in concentration of methylene blue (MB) after adsorption in the dark and photochemical reaction under UV irradiation, respectively. And the results indicated that the photocatalytic activity of porous SiOC ceramic for the degradation of MB is enhanced significantly by the incorporation of ZnO nanopowders into the SiOC matrix. Furthermore, micro- or nanostructured PDCs can be realized via lithographic methods [198] or 3D manufacturing techniques [199], which allow them to be applied as components for microfluidics nano-electromechanical (NEMS) and micro-electromechanical systems (MEMS) operating in harsh environments. Besides, researchers reported that SiCN has emerged as promising component for anode material in lithium-ion batteries, which further broadens the field of application of advanced PDCs [200-201]. Moreover, PDCs as a new technology for the fabrication of ceramic

based EMA materials has been already discussed above.

2.4 Nowotny phase

2.4.1 General background

In 1954, the Nowotny phase (NP), as the only stable ternary compound based on the Mo-Si-C system, was first identified and characterized by Nowotny et al [202]. Then, Parthé and co-workers [203] reported the accurate chemical composition of the NP with the formula $Mo_{4.8}Si_3C_{0.6}$. Besides, the chemical composition of the NP also can be described as Mo_5Si_3C or $Mo_{\leq 5}Si_3C_{\leq 1}$. According to X-ray diffraction result, The compound crystallizes with a hexagonal unit cell with a = 7.286 + 0.001 Å, c= 5.046 + 0.002 Å, in space group $P6_3/mcm$ (D^3_{6h}), six Mo atoms in position 6(g_I) with x = 0.240, 3.6 Mo atoms in 4(*d*), six Si atoms in position 6(g_{II}) with x=0.60 and 1.2 C atoms in 2(*b*). The carbon atoms occupy the octahedral voids formed by the Mo atoms in position 6(g_I) [203]. Thus, the crystal structure of the NP can be expressed as **Figure 2.12** [2]. Initially, the NP was synthesized by hot pressing a mixture of Mo, Si, and C powders with a prolonged holding time (1-3 h) under applied pressure (15 - 35 MPa) at the temperatures ranging from 1500 to 1700 °C [66, 68, 70, 202-203].

Furthermore, other combinations of starting materials were attempted, including graphite, Si, Mo, Mo_2C, $MoSi_2$ and Mo_5Si_3 [204]. There are two possible reactions of NP synthesis reported in the literature [205-206]:

$$Mo_5Si_3 + 0.7\ C \rightarrow Mo_{4.8}Si_3C_{0.6} + 0.1\ Mo_2C \qquad \textbf{Eq. (2.19)}$$

$$4.8\ MoSi_2 + 7.2\ C \rightarrow Mo_{4.8}Si_3C_{0.6} + 6.6\ SiC \qquad \textbf{Eq. (2.20)}$$

According to the reaction schemes, it is difficult to obtain pure single-phase NP. Commonly, there are other phases, such as Mo_2C, Mo_5Si_3, SiC or C, in the synthesized NP containing composites [207].

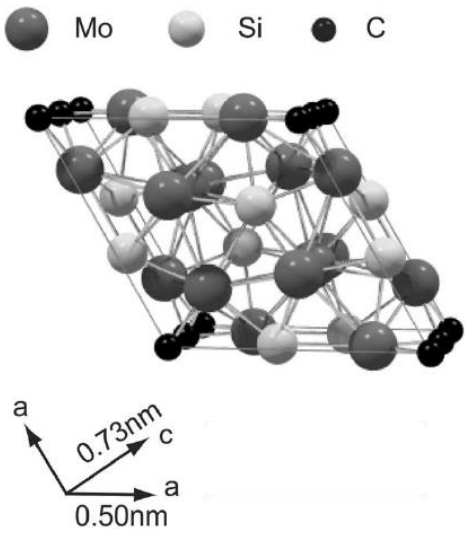

Figure 2. 12 Crystal structure of the Nowotny phase [2].

2.4.2 Properties and functional applications of the Nowotny phase

Although the Nowotny phase was first identified several decades ago, the discovered properties and functional applications of the compound are still limited until now. Firstly, the NP is mainly considered as an attractive reinforcement second phase of Si-based ceramic composites to enhance the fracture toughness, creep resistance and oxidation resistance of the composites due to its excellent mechanical properties and high melting point (~ 2100 °C) superior than that of the $MoSi_2$ and Mo_5Si_3 phases [65-70]. Even at high temperature (1700 °C), the SiC-$Mo_{\leq 5}Si_3C_{\leq 1}$ composite fabricated via the melt-infiltration process can still retain around 90% of their room-temperature strength, while compressive constant-load creep tests show that the stress range of a SiC-$Mo_{\leq 5}Si_3C_{\leq 1}$ composite is 200-250 MPa at 1760-1850 °C [67]. It is reported, that a SiOC-$Mo_{4.8}Si_3C_{0.6}$-$MoSi_2$ composite exhibits superior oxidation resistance at 450 ℃ and 1200-1600 ℃ in air, which is attributed to the $Mo_{4.8}Si_3C_{0.6}$ and $MoSi_2$ dispersoids [208]. Furthermore, the superconducting behavior of the $Mo_{4.8}Si_3C_{0.6}$ phase was found with a superconducting transition temperature as high as 12.2 K [71].

3 Cumulative part of the thesis

Within the cumulative part of this thesis, the major scientific findings reported in publications 1-3 are summarized and discussed. The first part of the work presented in Chapter 3.1 focuses on the synthesis, characterization of microstructure, and electrocatalytic activity of a Nowotny phase (NP) containing ceramic nanocomposite, namely $Mo_{3+2x}Si_3C_{0.6}$/C/SiC nanocomposite, synthesized via a single-source-precursor approach involving the reaction of $MoO_2(acac)_2$ with allylhydridopolycarbosilane (AHPCS, SMP-10). This is the first time that the NP is discovered to possess electrocatalytic activity and excellent durability in terms of the HER. In Chapter 3.2, in order to further improve the HER activity of the NP/C/SiC ceramic nanocomposites, divinylbenzene (DVB) was used as a rich-carbon source to synthesize mesoporous NP/C/SiC ceramic nanocomposites with enhanced carbon content. The obtained carbon-rich NP/C/SiC ceramic nanocomposite demonstrates a superior HER performance. Finally, we investigated the dielectric properties of the NP/SiC/C_{free} nanocomposites and evaluated their EMA performance. It is also for the first time that the NP is reported as EMA material. Besides, the correlation between the free carbon (C_{free}) content and *in-situ* formation of NP as well as their influence on the dielectric properties of the resultant NP/SiC/C_{free} nanocomposites were also addressed. Based on our previous discovery in Chapter 3.1 and Chapter 3.2 that the NP embedded in a SiC-based matrix with high specific surface area exhibits excellent electrocatalytic properties suitable for the electrochemical HER, the results in Chapter 3.3 prove that NP/SiC/C_{free} nanocomposites have to be considered as novel multifunctional materials with tailorable microstructure and excellent performance in two different fields including electrochemical water splitting and EMW absorption.

1. **Feng Y**, Yu Z, Schuch J, Tao S, Wiehl L, Fasel C, Jaegermann W, Riedel R, Ternary Nowotny phase $Mo_{3+2x}Si_3C_{0.6}$ dispersed in a porous SiC/C matrix: A novel catalyst for hydrogen evolution reaction. *Journal of the American Ceramic Society*, 103 (2020) 508-519.

2. **Feng Y**, Yu Z, Riedel R, Enhanced hydrogen evolution reaction catalyzed by carbon-rich $Mo_{4.8}Si_3C_{0.6}$/C/SiC nanocomposites via a PDC approach. *Journal of the American Ceramic Society*, 103 (2020) 1385–1395.

3. **Feng Y**, Yang Y, Wen Q, Riedel R, Yu Z, Dielectric properties and electromagnetic wave absorbing performance of single-source-precursor synthesized $Mo_{4.8}Si_3C_{0.6}$/SiC/C_{free} nanocomposites with an in-situ formed Nowotny phase. *ACS Applied Materials & Interfaces*, 12 (2020) 16912-16921.

3.1 Ternary Nowotny phase $Mo_{3+2x}Si_3C_{0.6}$ dispersed in a porous SiC/C matrix: a novel catalyst for hydrogen evolution reaction

The content of this Chapter is published in:

1. Feng Y, Yu Z, Schuch J, Tao S, Wiehl L, Fasel C, Jaegermann W, Riedel R, Ternary Nowotny rhase $Mo_{3+2x}Si_3C_{0.6}$ dispersed in a porous SiC/C matrix: A novel catalyst for hydrogen evolution reaction. *Journal of the American Ceramic Society*, 103 (2020) 508-519.

In this chapter, we present the in-situ formation of a nano-sized Nowotny phase (NP) with an occupancy of the Mo2 site between x = 0.9 and 0.764, depending on the pyrolysis temperature, embedded in a SiC-based matrix obtained from a novel single-source precursor. Electrochemical measurements revealed that the in-situ generated NP exhibits an outstanding catalytic activity with respect to the HER. To the best of our knowledge [68-69], this is the first time that the NP is discovered to possess electrocatalytic activity and excellent durability in terms of the HER. The obtained NP/C/SiC nanocomposite is characterized by the following specific features: i) in-situ formed catalytically active NP nanoparticles within an in-situ generated SiC/C-based matrix and ii) the simultaneous formation of carbon-rich phases improving the electric conductivity, which significantly increases the charge transfer rate during the HER process. As a result, the NP/C/SiC-based nanocomposites exhibit excellent HER activity with low overpotentials of 22 and 138 mV vs. reversible hydrogen electrode (RHE) for driving cathodic current densities of 1 and 10 mA cm^{-2} in acidic media, respectively.

3.1.1 Experimental section

3.1.1.1 Synthesis of the single-source-precursor

The single-source-precursor for the preparation of the NP/C/SiC nanocomposites was synthesized using allylhydridopolycarbosilane (AHPCS, SMP-10, Starfire System Inc, Schenectady, NY) and bis(acetylacetonato) dioxomolybdenum (VI) [$MoO_2(acac)_2$] (Sigma Aldrich) as starting materials. Polystyrene (PS, average Mw 35000, Sigma Aldrich) was used as pore former. The synthesis procedure was carried out under an argon atmosphere (Schlenk technique) in order to prevent hydrolysis of the starting materials. One typical synthesis is described as follows: 1.00 g $MoO_2(acac)_2$ was introduced into a 100 mL Schlenk flask in an argon atmosphere, and then 25 mL anhydrous toluene (Sigma Aldrich) was added to solve $MoO_2(acac)_2$ until a dark blue solution was obtained. Subsequently, 2.00 g SMP-10 and 2.00 g PS were added to the Schlenk flask with stirring at room temperature for 30 min. After dispersing under ultrasound for another 10 min, the resultant solution was refluxed for 24 h in an argon atmosphere. Finally, a viscous dark yellow Mo-containing precursor was obtained after the solvent was stripped off under vacuum. The weight ratios of SMP-10/$MoO_2(acac)_2$/PS are 2/1/2 and 2/1/4, and the obtained samples are abbreviated as SM/Mo/PS 2-1-2 and SM/Mo/PS 2-1-4, respectively. A control test without PS was

performed under the same conditions and the resultant product is nominated as SM/Mo/PS 2-1-0.

3.1.1.2 Synthesis of the single-source-precursor

Before pyrolysis, all Mo-containing precursors were cured at 170 °C for 6 h in an argon atmosphere. The pyrolysis of the as-cured precursors was then performed in a tube furnace. The cured sample was placed in an alumina boat and heated in a quartz glass tube under an argon flow. According to the literature [209], the pyrolysis profile with slow heating rates and long dwelling times was chosen to prepare nanoporous ceramics with high surface area as follows: the precursors were heated from room temperature with a rate of 100 °C/h to 200 °C, hold for 5 h at 200 °C, further heated to 300 °C with a rate of 50 °C/h, hold for 3 h at 300 °C, further heated to 400 °C with a rate of 50 °C/h, hold for 3 h at 400 °C, further heated to 500 °C with a rate of 50 °C/h, hold for 5 h at 500 °C, further heated to 600 °C with a rate of 50 °C/h, hold for 3 h at 600 °C, further heated to 1100 °C with a rate of 50 °C/h, hold for 2 h at 1100 °C, and finally cooled to room temperature with a rate of 50 °C/h. Subsequently, the materials were annealed at elevated temperatures (1200 °C-1400 °C) for 2 h in Ar to form NP/C/SiC nanocomposites.

3.1.1.3 Materials characterization

Attenuated total reflectance infrared (ATR-IR) spectra of the samples were recorded using a PerkinElmer Spectrum spotlight 200 Fourier transform infrared (FT-IR) spectrometer with a PerkinElmer single reflection UATR unit. Thermogravimetric analysis with in-situ mass spectrometry (TGA/MS) were carried out with a thermal analysis device (STA 449C Jupiter, Netzsch, Germany) coupled with a quadruple mass spectrometer (QMS 403C Aëolos, Netzsch, Germany) to study the polymer-to-ceramic transformation of the Mo-containing precursors. The thermal analysis includes heating under flowing argon with a rate of 5 °C min^{-1}, holding at 1400 °C for 2 h and free cooling down to room temperature. The carbon and oxygen contents of the ceramics were measured by hot gas extraction techniques with a LECO C-200 and a LECO TC-436 analyzer (LECO Corporation, St. Joseph, MI), respectively. Powder X-ray diffraction (XRD) experiments were recorded using a STADI P powder diffractometer (STOE & Cie GmbH, Darmstadt, Germany) with Mo $K\alpha_1$ radiation source and a Germanium-monochromator. Raman spectra were recorded from 400-4000 cm^{-1} employing a micro-Raman HR8000 spectrometer (Horiba JobinYvon, Bensheim, Germany) with a laser wavelength of 631.81 nm. The X-ray photoelectron spectroscopy (XPS) measurements were performed with monochromatic Al K_α radiation (XR 50, SPECS Surface Nano Analysis GmbH). A hemispherical electron analyzer (PHOIBOS 150, SPECS Surface Nano Analysis GmbH) was used, calibrated with the core lines of copper, silver and gold. Peaks were fitted using a Shirley background and a mixed Gauss/Lorentz peak. The $Mo_{3+2x}Si_3C_{0.6}$/C/SiC nanocomposite powder samples before and after the electrochemical measurements were embedded in indium foil and glassy carbon electrode respectively. The microstructural analysis of the nanocomposite powders was performed by scanning electron microscopy (SEM) on a Philips XL30 S-FEG microscope (FEI Company, Hillsboro, OR). Transmission electron microscopy (TEM) studies were conducted on ground powder samples using a JEM-

2100 (JEOL Ltd, Tokyo, Japan) microscope at an acceleration voltage of 200 kV (wavelength 2.508 pm). In addition, the selected area electron diffraction (SAED) technique was employed in order to analyze the formed crystalline phases. The BET specific surface area of the ceramics was investigated by an Autosorb-3B Surface Area and Pore Size Analyzer (Quantachrome Instruments Corporation, Boynton Beach, FL) at -196 °C, after the powdered samples were out gassed at 100 °C for 24 h. The N_2 isotherm at -196 °C was used to calculate the specific surface area from the linear BET plots. The total pore volume was determined from the amount of vapor adsorbed at a relative pressure p/p_0 = 0.972. The micropore volume was calculated using de Boer's t-plot analysis.

3.1.1.4 Electrochemical characterization

Electrochemical characterization was carried out in a three-electrode setup using an Interface 1000 potentiostat from Gamry Instruments. The measurements were performed in a standard photoelectrochemical cell of 7.2 mL volume (PECC-2, Zahner) in 0.5 M H_2SO_4 (Carl Roth, standard solution) as electrolyte. A platinum wire was used as the counter electrode and an Ag/AgCl electrode saturated in 3 M KCl was used as a reference electrode. The working electrodes were prepared by dispersing 10 mg of catalyst in 1.0 mL of deionized water and 20 µL of 5 wt% Nafion solution and pipetting out 20 µL of the obtained slurry onto a glassy carbon electrode with 0.2 cm^2 active area to provide a weight density of 0.95-1.00 mg/cm^2. 9 µL of Nafion solution was added on top to fix the electrocatalyst. All potentials were referenced to a reversible hydrogen electrode (RHE). All catalysts were investigated according to a specified test procedure, which included the measurement of the open circuit potential (OCP), the electrochemical impedance spectroscopy (EIS) (20 Hz to 20 kHz) to obtain the setup resistance for iR compensation and the cyclic voltammogram (CV) recorded with a scan rate of 5 mV/s in the range of 0.1 to -0.5 V. All potentials presented were corrected for iR losses.

3.1.2 Results and discussion

3.1.2.1 Characterization of the single-source-precursor

Taking the synthesis of SM/Mo/PS 2-1-2 as an example, the molecular structure of the single-source-precursor was investigated by FT-IR spectroscopy and the results are shown in **Figure 3.1**. From a comparison of the FT-IR spectra of the SM/Mo/PS 2-1-2 with those of the original SMP-10, $MoO_2(acac)_2$ and PS, it is found that the sample SM/Mo/PS 2-1-2 exhibits characteristic peaks of that of SMP-10, $MoO_2(acac)_2$ and PS. The PS is used as a pore former, which contains no functional group that can be involved in the chemical reaction between SMP-10 and $MoO_2(acac)_2$. It's worth mentioning that the relative intensity of the Si-H stretch (2136 cm^{-1}) absorption peak in the SM/Mo/PS 2-1-2 precursor significantly decreases, compared to that of the original SMP-10. This result indicates that SMP-10 reacted with $MoO_2(acac)_2$ consuming Si-H groups. As for the reaction of polycarbosilane with metal acetylacetonates, it has been confirmed to form Si-O-M bonds by our previous work [210-211]. In this study, as shown in **Figure**

3.1 (b), the new absorption band at 950 cm^{-1} is assigned to the formed Si-O-Mo unit [212].

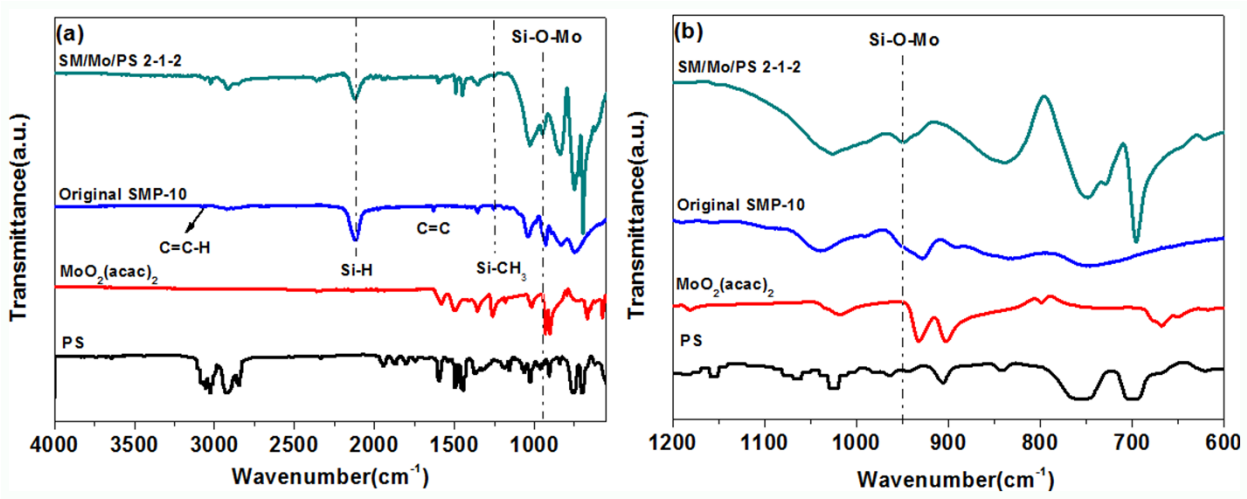

Figure 3. 1 FT-IR spectra of the original AHPCS, PS, $MoO_2(acac)_2$, and the sample SM/Mo/PS 2-1-2 (a) with a magnification of the region between 600 and 1200 cm^{-1} (b).

The FT-IR results clearly demonstrate, that the reaction between SMP-10 and $MoO_2(acac)_2$ results in the formation of Si-O-Mo bonds. Based on this finding, which is in agreement with previous studies [210-211], the idealized reaction scheme shown in **Figure 3. 2** is discussed.

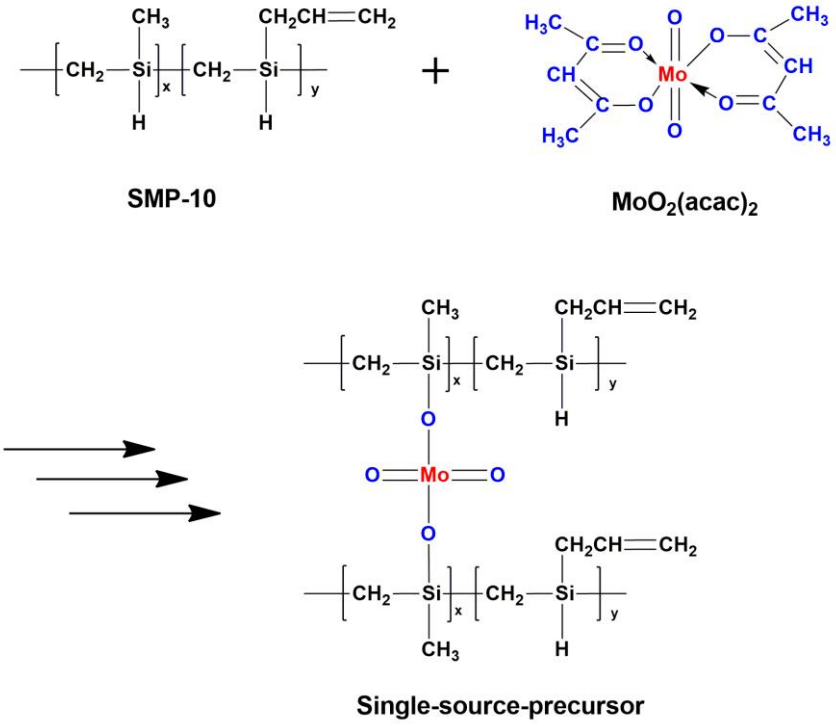

Figure 3. 2 Idealized reaction path between SMP-10 and $MoO_2(acac)_2$ to form the single-source-precursor SSP.

In order to understand the thermal behavior during the polymer-to-ceramic transformation, the SMP-10 and Mo-containing precursors cured at 170 °C were analyzed by TGA and the result is presented in **Figure 3. 3**. According to the literature [213-214], the different pyrolytic characteristics of the ceramic precursor and pore former are essential for obtaining porous materials. The cured SMP-10 was converted into ceramics in high yield (78 wt%) above 850 °C since no obvious weight loss is observed at higher temperatures. As expected, the ceramic yields of SM/Mo/PS 2-1-2 and SM/Mo/PS 2-1-4 are much lower than that of SM/Mo/PS 2-1-0 (without PS) and the cured SMP-10, and the ceramic yield of samples with higher PS content (SM/Mo/PS 2-1-4) is lower than that of SM/Mo/PS 2-1-2, due to the fact that PS decomposes completely at 600 °C [215]. Furthermore, according to the initial additive amount of PS and the ceramic yields (70.7 wt%) of SM/Mo/PS 2-1-0 at 1400 °C, the theoretical ceramic yields of SM/Mo/PS 2-1-2 and SM/Mo/PS 2-1-4 at 1400 °C are 42.4 wt% and 30.3 wt%, which are close to the ceramic yields of SM/Mo/PS 2-1-2 (38.6 wt%) and SM/Mo/PS 2-1-4 (31.2 wt%) analyzed by TGA, respectively. The result again confirms the complete decomposition of PS during the pyrolysis. In summary, the decomposition and elimination of PS results in the formation of pores, and the pyrolysis of the Mo-containing SMP-10 produces the skeleton of the porous ceramics. Moreover, a small weight loss of SM/Mo/PS 2-1-2 and SM/Mo/PS 2-1-4 was detected at 1100 - 1400 °C. Elemental analysis of the samples (SM/Mo/PS 2-1-2) annealed at 1300 and 1400 °C indicate that the oxygen content reduced from 15.29 wt% to 6.13 wt% due to carbothermal reaction [214] which leads to the weight loss analyzed during 1100 - 1400 °C. Moreover, the carbon content of sample (SM/Mo/PS 2-1-2) annealed at 1400 °C is 24.88 +/-0.01 wt.%.

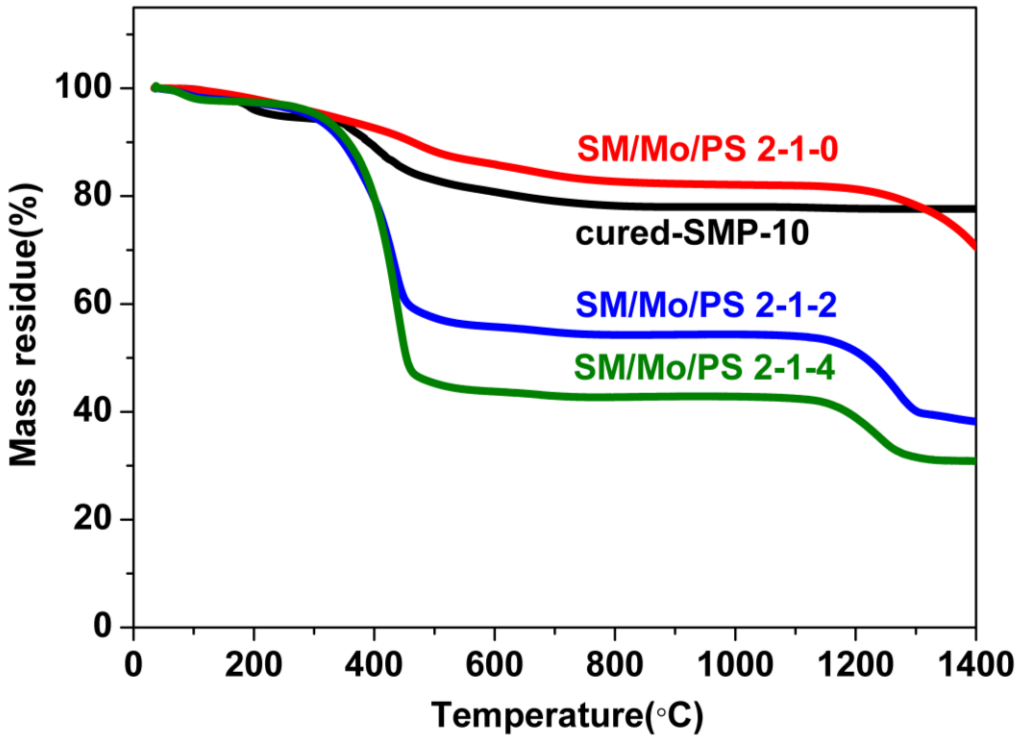

Figure 3. 3 TGA curves of preceramic precursors with different PS content after cured at 170 °C.

3.1.2.2 Phase composition and microstructure of the ceramics

The phase composition of the resultant ceramic samples annealed at 1100-1400 °C was studied by powder X-ray diffraction (XRD) and Raman spectroscopy. **Figure 3. 4** (a) clearly shows that the resultant ceramics are composed of a Nowotny phase (NP) with a composition close to $Mo_{4.8}Si_3C_{0.6}$ (ICSD-23858, JCPDS card no. 43-1199) and sphalerite-type SiC (JCPDS card no. 49-1428). The NP is found after annealing of the SSP at 1200 °C, and increasing annealing temperature leads to a sharpening of the characteristic peaks of the NP, indicating an improved degree of crystallization. In addition, the lattice parameters of the NP are different for samples synthesized at different temperature, best seen for the (102) and (112) reflections. Interestingly, the samples prepared at lower temperature (1350 °C and below) do not show a significant reduction of the c lattice parameter of the Nowotny phase. **Figure 3. 4** (b) shows the (102) and (112) reflections of the 1200 to 1350 °C samples nearly at the positions given in the literature [203], whereas they are clearly shifted for the sample prepared at 1400 °C.

A Rietveld refinement of the powder pattern of the NP/C/SiC-based ceramic nanocomposite annealed at 1400 °C (denoted as sample SM/Mo/PS 2-1-2 1400) was performed using the program GSAS-II [216]. The result is shown in **Figure 3. 4** (c). The peak shapes were modeled by pseudo-Voigt functions, using the instrument parameters from a NIST Si standard. Most of the reflections can be attributed to sphalerite-type SiC and a Nowotny phase similar to $Mo_{4.8}Si_3C_{0.6}$ [203], however with significantly changed lattice parameters. A few reflections, the strongest of them at $2\theta = 15.3°$, come from a third not yet identified phase. No reflections of crystalline Mo_2C or Mo_5Si_3 or graphite are visible, however there is a considerable amorphous background, which may contain free carbon. The weight fractions of the N-MoSiC and SiC phases obtained by Rietveld refinement of the XRD patterns are 28 (26) wt% and 72 (74) wt%, respectively, when prepared at 1400 °C (1350 °C), while the average crystallite sizes of the N-MoSiC and SiC phases are 70 nm and 40 nm, respectively. The crystal structure [203] of $Mo_{4.8}Si_3C_{0.6}$ is shown in **Figure 3. 4** (d).

The Nowotny phase of the sample annealed at 1400 °C exhibits a significant reduction of the c c-lattice parameter by 2.0 % as compared to the value given for $Mo_{4.8}Si_3C_{0.6}$ by Parthé [203]. The a-lattice parameter is slightly increased by 0.1 %, which results in a reduction of the unit cell volume by 1.7 %. As essentially only the c-axis is affected, the corresponding X-ray reflections experience the largest shifts, especially (102) and (112) at $2\theta = 17.73°$ and 19.96° with d = 2.303 Å and 2.047 Å, respectively, whereas for the sample prepared at 1350 °C the (102) and (112) reflections are at $2\theta = 17.42°$ and 19.70° with d = 2.343 Å and 2.074 Å, with no significant deviation from the literature values of $Mo_{4.8}Si_3C_{0.6}$. Corresponding to the reduced unit cell volume also the occupation factor of Mo2 on the threefold axis with a short Mo-Mo distance of half the c-axis [c.f. **Figure 3. 4** (d)] is reduced from 0.9 in the literature [203] to 0.764 in our refinement. Thus, the composition of the Nowotny phase in the 1400 °C sample is approximately $Mo_{4.5}Si_3C_{0.6}$ instead of $Mo_{4.8}Si_3C_{0.6}$.

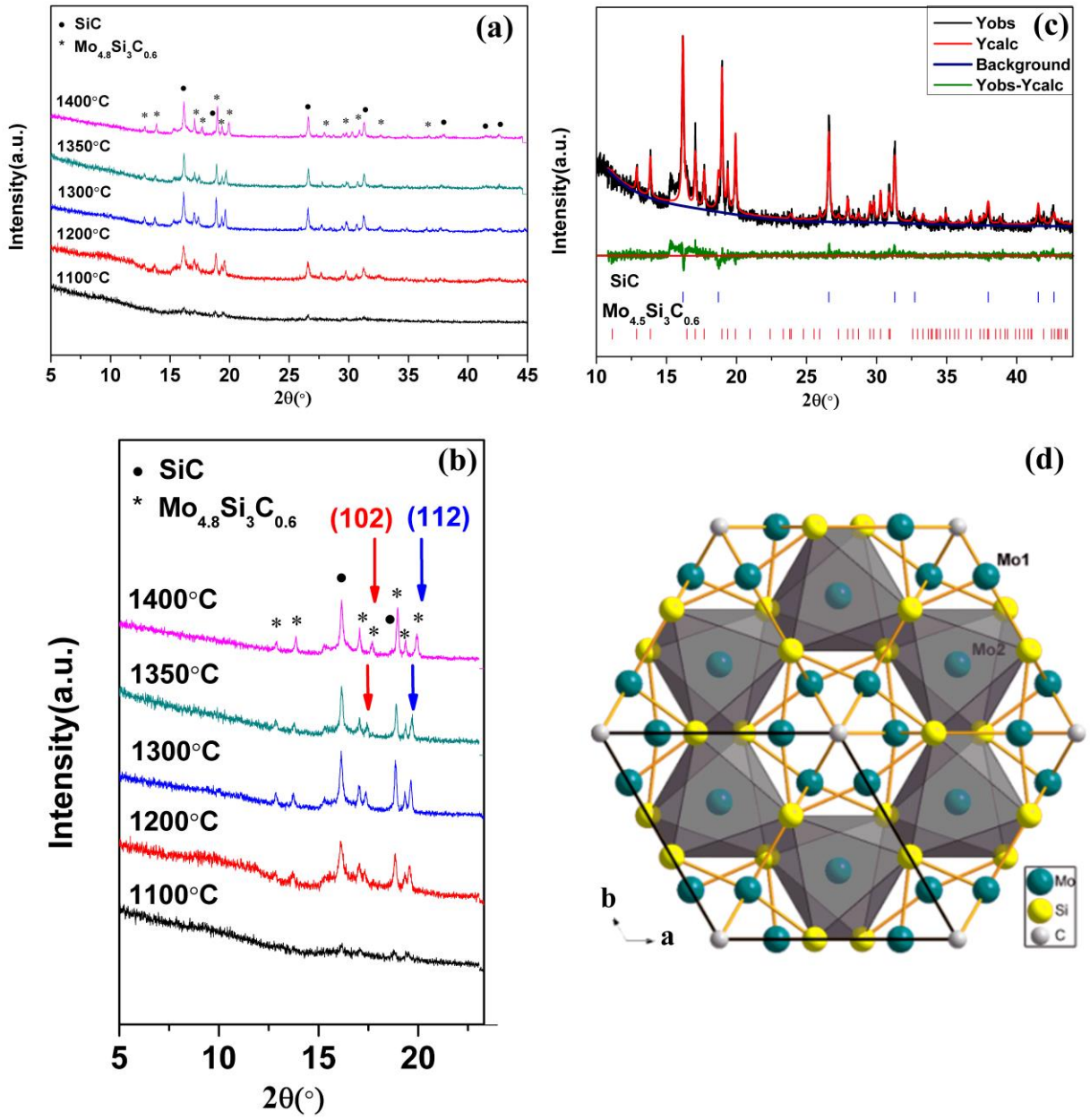

Figure 3. 4 XRD patterns (a) of SM/Mo/PS 2-1-2 derived NP/C/SiC nanocomposites after annealing at different temperatures with a magnification of the 2θ region between 5 and 25 ° (b); Diffraction pattern (c) of the ceramic annealed at 1400 °C (SM/Mo/PS 2-1-2 1400) with the result of Rietveld refinement. Y_{obs} and Y_{calc} represent the observed and calculated profiles respectively; the blue line represents the background; the green line at the bottom denotes the intensity difference between the observed and calculated profiles; (d) Crystal structure of the Nowotny phase $Mo_{4.8}Si_3C_{0.6}$. The unit-cell and atomic bonds are shown. Green balls: Mo, gray balls: C, and yellow balls: Si. The Mo2 site, shown with the octahedral coordination (gray faces), is not fully occupied, as well as the carbon site.

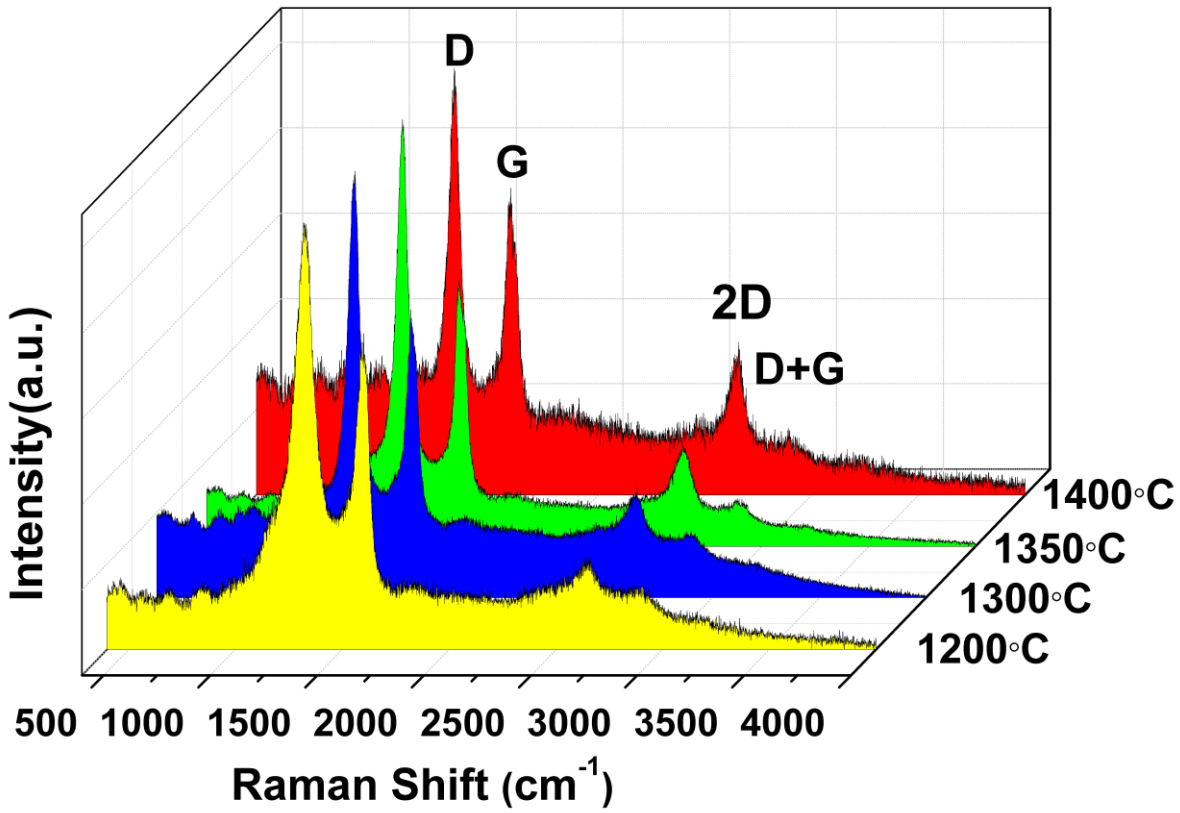

Figure 3. 5 Raman spectra of SM/Mo/PS 2-1-2 derived NP/C/SiC nanocomposites after annealing at different temperatures.

As shown in **Figure 3. 5**, Raman spectra of the ceramics annealed at 1200-1400 °C reveal the presence of sp^2-bonded carbon at all temperatures. Accordingly [217-218], the D-band at ca. 1340 cm^{-1} originates from a double-resonance Raman process in disordered carbon and the G-band at ca. 1585 cm^{-1} corresponds to graphitic carbon. Besides, the 2D band (2700 cm^{-1}) is an overtone of the D band which is usually found in defect-free graphite samples. And the D + G band (2945 cm^{-1}) can be assigned to a combination of the G and D modes which is characteristic for disturbed graphitic structures. After heat treatment at 1200 °C, the D (1350 cm^{-1}) and G (1580 cm^{-1}) bands of carbon are broad due to the high disorder of the segregated carbon. With increasing annealing temperature, the D and G bands show smaller line width and the intensities of the G and 2D (2700 cm^{-1}) bands grow gradually indicating progressive structural ordering of the carbon. Based on the XRD and Raman spectroscopic results, the ceramics obtained after annealing at $T \geq 1200$ °C are characterized as NP/C/SiC nanocomposites.

The morphology and microstructure of the NP/C/SiC-based ceramic nanocomposite annealed at 1400 °C (denoted as sample SM/Mo/PS 2-1-4 1400) were investigated by SEM and TEM (**Figure 3. 6**). The SEM images show an aerogel-like morphology [see **Figure 3. 6** (a), (b)]. With respect to the microstructure, the bright-field lattice image reveals the presence of faceted NP nanoparticles with the size of < 100 nm

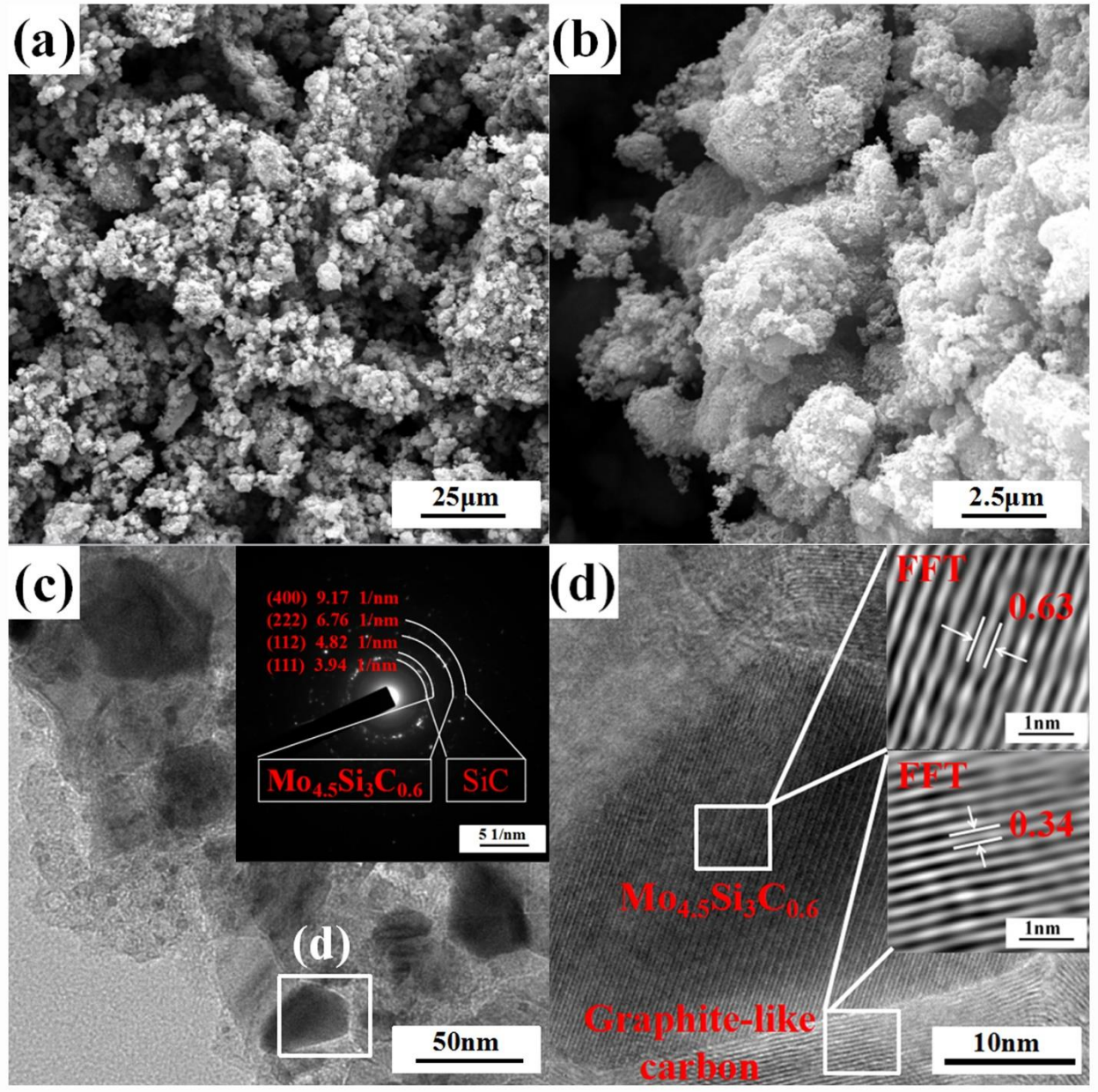

Figure 3. 6 (a, b) SEM images, (c) TEM image and (d) HRTEM images of NP/C/SiC-based nanocomposites (SM/Mo/PS 2-1-4 1400).

dispersed in a SiC matrix. The crystalline phases consist of NP and SiC, exclusively, as identified by selected-area electron-diffraction (SAED) [**Figure 3. 6** (c)]. The high-resolution image [**Figure 3. 6** (d)] shows a NP crystallite (lattice spacing of ca. 0.63 nm) with a size of about 20-30 nm, which reflects the nanoscaled microstructure and fulfills the definition of nanocomposites. The in situ formed NP nanocrystallites are dispersed in a simultaneously generated nanocrystalline SiC matrix. Due to the matrix confinement, the crystal growth of the nanocrystalline Nowotny phase is strongly retarded. According to the literature [219-220], although the catalytic activity of large and irregular Mo-based particles is already high, enhanced performance due to more defined nanoparticles is still an important challenge for Mo-based electrocatalysts. In addition, some graphite-like carbon shell, with a lattice spacing of ca. 0.34 nm, was

found around the NP nanoparticle as shown in **Figure 3. 6** (d). The carbon shell is considered to improve the electric conductivity of the electrocatalyst, which is a significant requirement to increase the electrocatalytic activity.

The porosity features of the ceramic samples with different PS content annealed at 1300, 1350 and 1400 °C were investigated according to the Brunauer-Emmet-Teller (BET) method by N_2 adsorption isothermal analysis. As shown in **Figure 3. 7**, the nitrogen physisorption isotherms manifest that all samples reveal a type-IV isotherm which is related to a mesoporous nature of the materials. Previous studies indicated that tuning the ratio of preceramic precursor to pore former is a convenient method to change the surface area of porous materials [214]. Therefore, the weight ratio of SMP-10 to PS was varied from 1/0 to 1/2. With increasing PS content in the feed, the specific surface area of the samples annealed at the same temperature (1300, 1350 and 1400 °C) increases significantly as can be quantitatively evaluated from the BET results shown in **Figure 3. 7** (a)-(c). Especially, after annealing at 1400 °C for 2 h, the sample with high PS content (SM/Mo/PS 2-1-4 1400) is analyzed to still maintain a high surface area (141.8 m^2/g), which is significantly higher than that of the sample without PS (SM/Mo/PS 2-1-0 1400, 7.32 m^2/g) [**Figure 3. 7** (c)]. With the

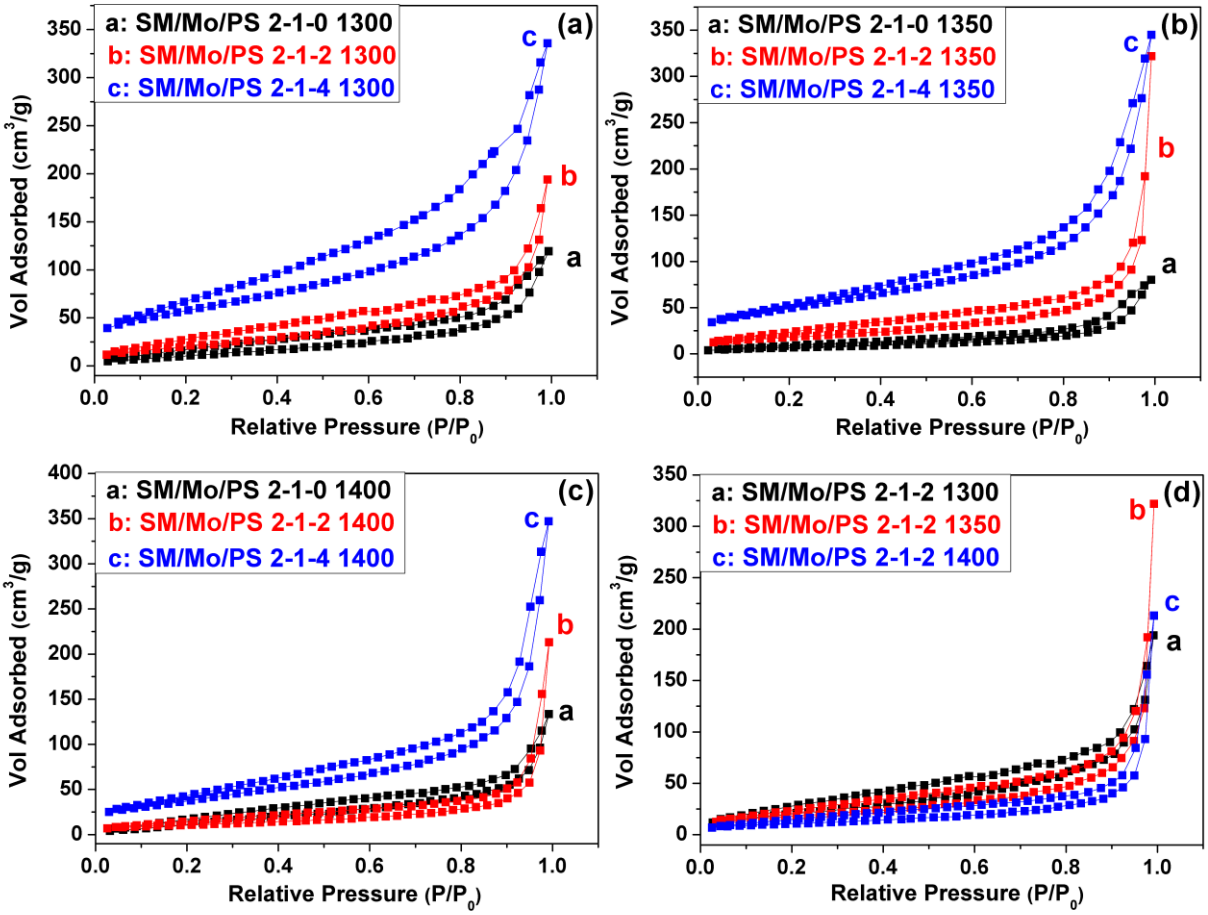

Figure 3. 7 N_2 adsorption-desorption isotherms of the ceramic samples derived from single-source-precursors with different PS content annealed at 1300, 1350 and 1400 °C (a, b, c) and from SM/Mo/PS 2-1-2 annealed at different temperatures (d).

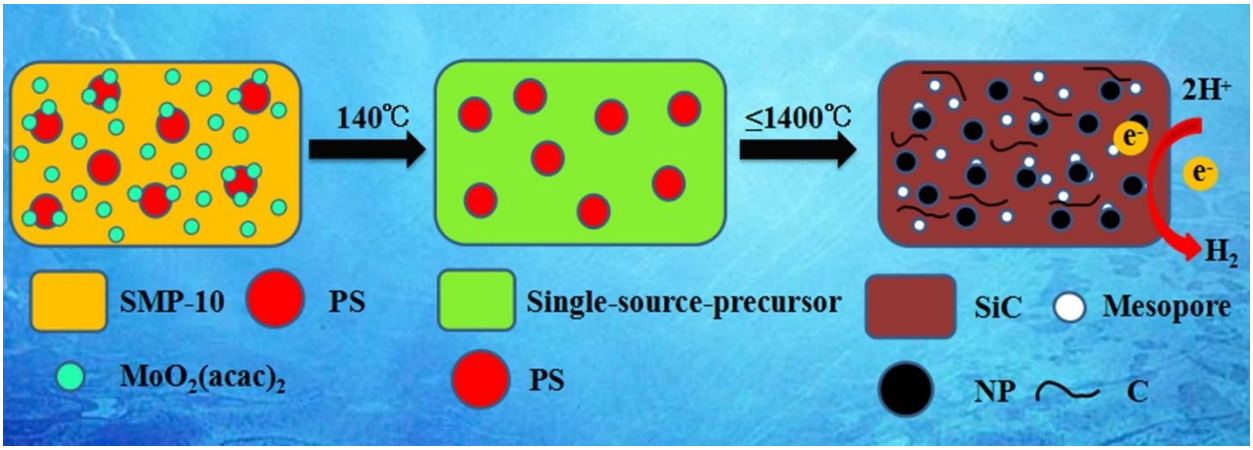

Figure 3. 8 Schematic illustration of the synthesis of porous NP/C/SiC-based ceramic nanocomposites based on spectroscopic, X-ray diffraction and electron microscopic studies.

same content of PS in the feed, the surface area of the obtained ceramics decreases significantly with increasing temperature, which is due to a partial collapse of pores after high-temperature annealing. As clearly shown in **Figure 3. 7** (d), when the annealing temperature increases from 1300 to 1400 °C, the surface area of SM/Mo/PS 2-1-2 derived ceramics decreases gradually from 80.37 m^2/g to 38.35 m^2/g. The specific surface area of all samples is listed in Table S1 (see supporting information). Moreover, **Figure 3. S1** shows the corresponding pore size distributions, calculated based on the desorption branches of the isotherms of the ceramic samples derived from SM/Mo/PS 2-1-2 and SM/Mo/PS 2-1-4 annealed at 1300 to 1400 °C. And the average pore diameter of samples is about 10-30 nm, which again confirms the NP/C/SiC ceramic nanocomposites have a mesoporous (2-50 nm in pore diameter) feature.

Based on the results concerning single-source-precursor characterization, phase composition, microstructure and porous feature of resultant ceramic nanocomposites, the synthesis procedure of the obtained porous NP/C/SiC-based ceramic nanocomposites is schematically depicted in **Figure 3. 8**.

3.1.2.3 Electrocatalytic performance

The electrocatalytic performance of the as-prepared NP/C/SiC nanocomposite was analyzed with respect to the HER in acidic conditions (0.5 M H_2SO_4). The working electrode was prepared by depositing the nanocomposite powders with a mass load of 0.95-1.00 mg cm^{-2} onto a glassy carbon electrode. As shown in **Figure 3. 9**, all samples containing different specific surface areas and annealed at different temperatures reveal electrocatalytic activity. Due to the fact, that SiC is a poor catalyst for hydrogen evolution [221], the measured electrocatalytic activity has to be attributed to the presence of the NP nanoparticles with a weight fraction of about 30 %. As shown in **Figure 3. 9** (a)-(c), the electrocatalytic performance of the samples annealed at the same temperature increases significantly with increasing surface area, since a porous network provides efficient transport pathways to the interior cavities enhancing the electrocatalytic activity of the catalyst. Particularly, as shown in **Figure 3. 9** (c), after annealing at 1400 °C for 2 h, the sample

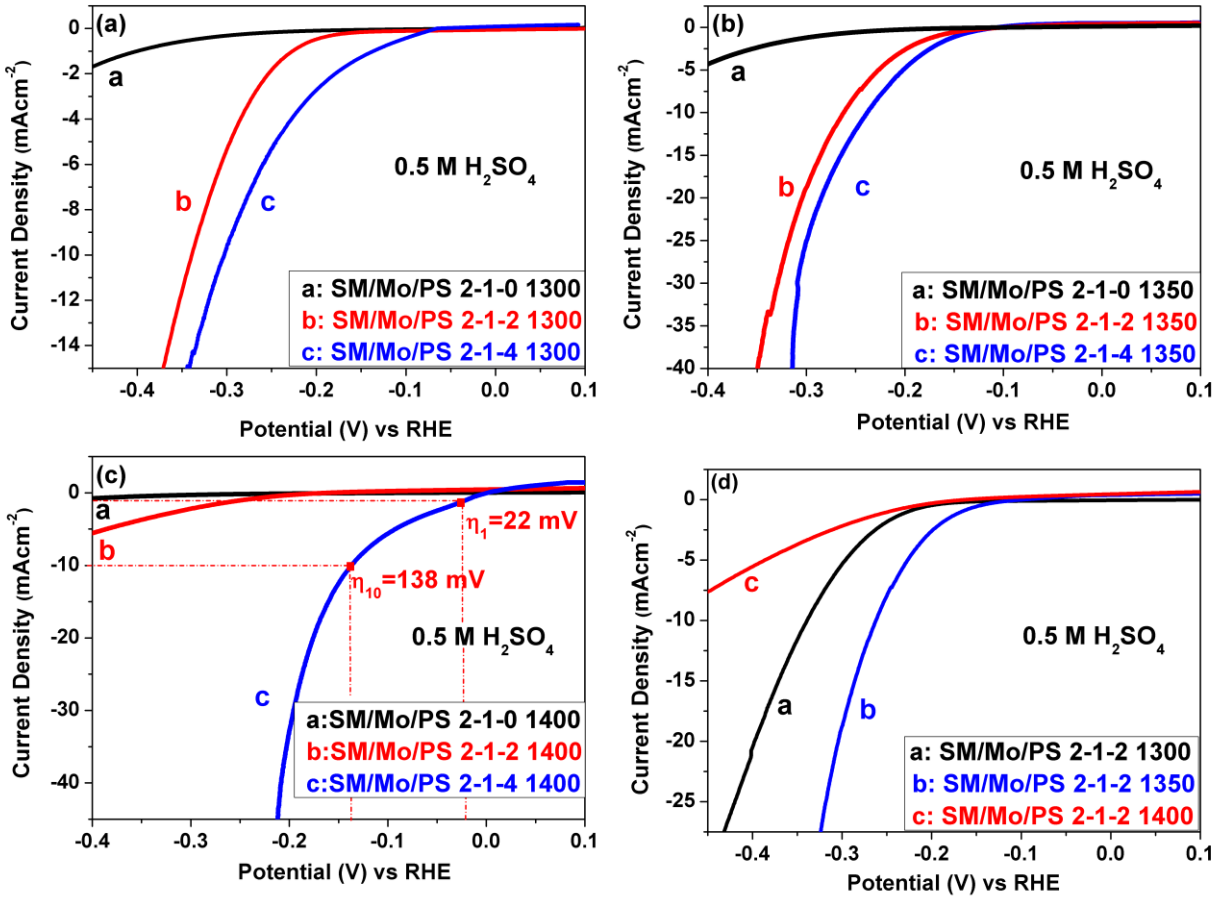

Figure 3. 9 Polarization curves (iR corrected, **Table 3. S1**) of ceramic samples derived from single-source-precursors with different PS content annealed at 1300-1400 °C (a, b, c) and of the sample derived from SM/Mo/PS 2-1-2 annealed at different temperatures (d).

SM/Mo/PS 2-1-4 1400 with high PS content in the precursor exhibits a strong improvement of the electrocatalytic activity in terms of the HER, reaching a current density of 1 mA cm^{-2} and 10 mA cm^{-2} at ultra-small overpotentials of 22 and 138 mV, respectively. In general, the sample SM/Mo/PS 2-1-4 1400 shows the highest electrocatalytic activity based on the overpotentials, as marked in **Figure 3. 9** (c). The electrocatalytic activity of the nanocomposite annealed at different temperatures is shown in **Figure 3. 9** (d). Accordingly, with the annealing temperature increasing from 1300 to 1350 °C, the overpotentials (η_1) driving current densities of 1 mA cm^{-2} of the NP/C/SiC ceramic decrease from 360 mV to 167 mV. In addition, overpotentials (η_{10}) of 338 and 262 mV are required for the samples annealed at 1300 and 1350 °C, respectively to drive current densities of 10 mA cm^{-2}. The results indicate that in the temperature range of 1300-1350 °C, the samples annealed at a higher temperature exhibit higher electrocatalytic activities. Although the increasing annealing temperature decreased the surface area [**Figure 3. 9** (d)], the higher annealing temperature significantly increased the crystallinity of the NP phase as proofed by the XRD results [**Figure 3. 4** (a)]. Moreover, the lattice parameters of the Nowotny phase change at annealing temperatures beyond 1350 °C and are significantly different from the literature values. As a consequence,

the composition of the NP varies between $Mo_{4.8}Si_3C_{0.6}$ in the samples annealed up to 1350 °C and $Mo_{4.5}Si_3C_{0.6}$ after heat-treatment at 1400 °C. However, the electrocatalytic activity of the sample with lower PS content in the precursor annealed at 1400 °C decreased remarkably, due to their lower surface area (38.35 m^2/g). Moreover, the linear portions of the Tafel plots at low overvoltage were shown in **Figure 3. S2** and the HER performance of all samples are shown in **Table 3. S1** (See Supporting Information).

In order to get further information about the active sites XPS experiments were performed before and after electrochemical treatment for different exposure times. The results and spectra are summarized in the supporting information (**Figure. 3. S3** and **S4**). As often observed in electrocatalysis the originally given surface composition is not the same as after elongated electrochemical activation within the electrolyte as also found for this composite material. The as prepared samples show in addition to the contributions of the Nowotny phase and the matrix SiC/C, their surface oxidation products as well as some small surface contamination of adventitious C. After extended electrochemical treatment the surface composition is dominated by spectral features related to the Nowotny phase, SiO_x, and MoO_2. Formation of $MoSi_2$ can be excluded as no signal appears in the expected binding energy range. With these results we would assign the active sites to the Nowotny phase entity as these remain mainly unchanged after electrochemical activation and after extended electrochemical stability treatment (further discussion can be found in the Supporting Information).

Stability in acidic media is another important criterion for an electrocatalyst. Therefore, the stability of the SM/Mo/PS 2-1-4 1400 sample was measured at a constant current density of 10 mA cm^{-2} in acidic media

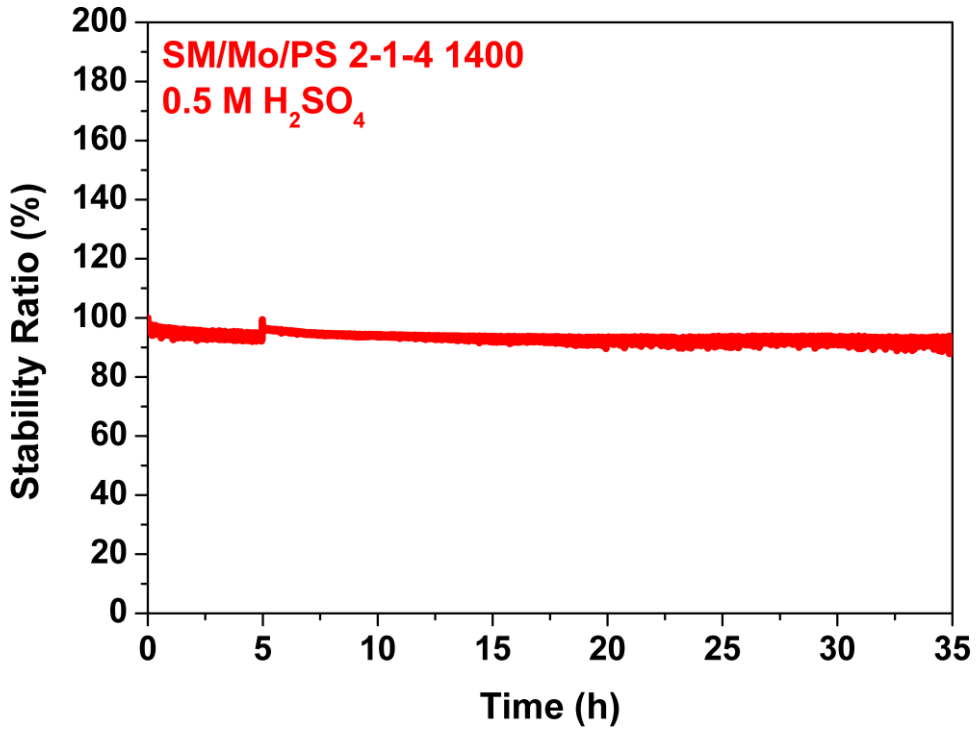

Figure 3. 10 Electrochemical stability test of the sample SM/Mo/PS 2-1-4 1400 in 0.5 M H_2SO_4 at constant current density of 10 mA cm^{-2}.

(0.5 M H_2SO_4) to obtain the time-dependent potentials of the electrode. **Figure 3. 10** reveals that the sample retains over 90 % of its original electrochemical activity after operating of the electrode for 35 h, demonstrating a robust and stable electrocatalytic performance of the material under acidic conditions.

3.1.3 Conclusions

In summary, single-source precursor derived mesoporous NP/C/SiC ceramic nanocomposites exhibit outstanding electrocatalytic properties suitable for the electrochemical hydrogen evolution. The obtained η_1 and η_{10} values of sample SM/Mo/PS 2-1-4 1400 amount to 22 and 138 mV in acidic media, respectively, which are superior to most of all previously reported molybdenum-based electrocatalysts (**Figure 3. S5**). Moreover, the material also shows excellent corrosion stability in acidic media. The analyzed exceptional electrocatalytic performance is based on i) catalytically active nanocrystalline ternary MoSiC Nowotny phase, dispersed and immobilized in a SiC-based ceramic matrix; ii) the presence of carbon improving the overall electric conductivity of the nanocomposites; iii) the highly porous network originated from the addition of PS as pore former enabling the efficient access of active sites of the MoSiC electrocatalyst. The single-source-precursor route allows to synthesize nanocomposites with all in-situ formed phases and advanced electrocatalytic performance for the HER. It is expected that a variety of further cutting-edge metal carbide-based nanocomposites can be achieved in future using the single-source-precursor approach as reported here.

3.1.4 Supporting information

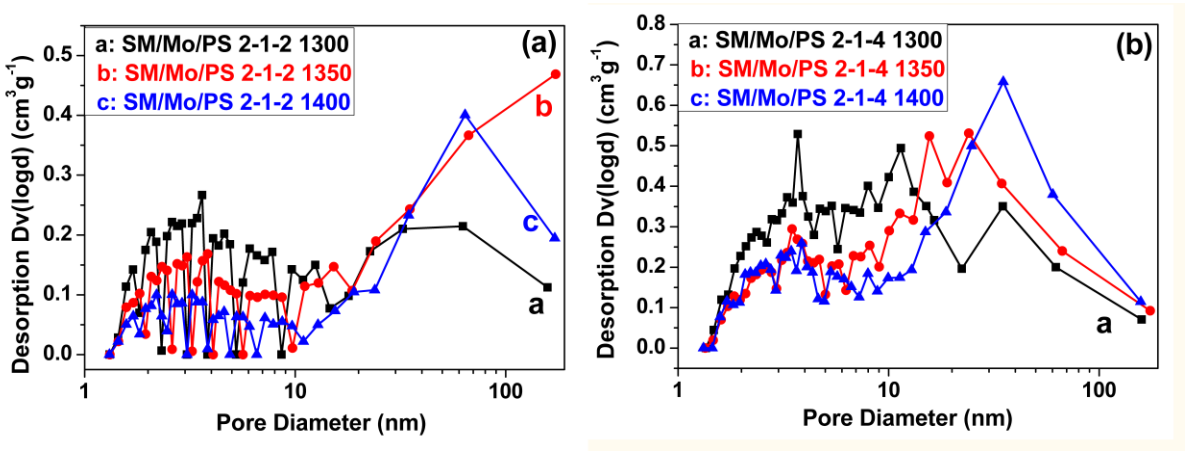

Figure 3. S1 Pore size distribution of the ceramic samples derived from SM/Mo/PS 2-1-2 (a) and SM/Mo/PS 2-1-4 (b) annealed at different temperatures.

To elucidate the HER mechanism, Tafel Plots were fitted to Tafel equation ($\eta = b \log(|j|) + a$, where j is the value of the current density after skipping the unit (mA/cm^2) and b is the Tafel slope), as shown **Figure 3. S2.** And the Tafel slopes of all samples were approximately 119.9-181.1 mV $decade^{-1}$, which suggests that the hydrogen evolution is based on the Volmer-Heyrovsky mechanism [11, 111].

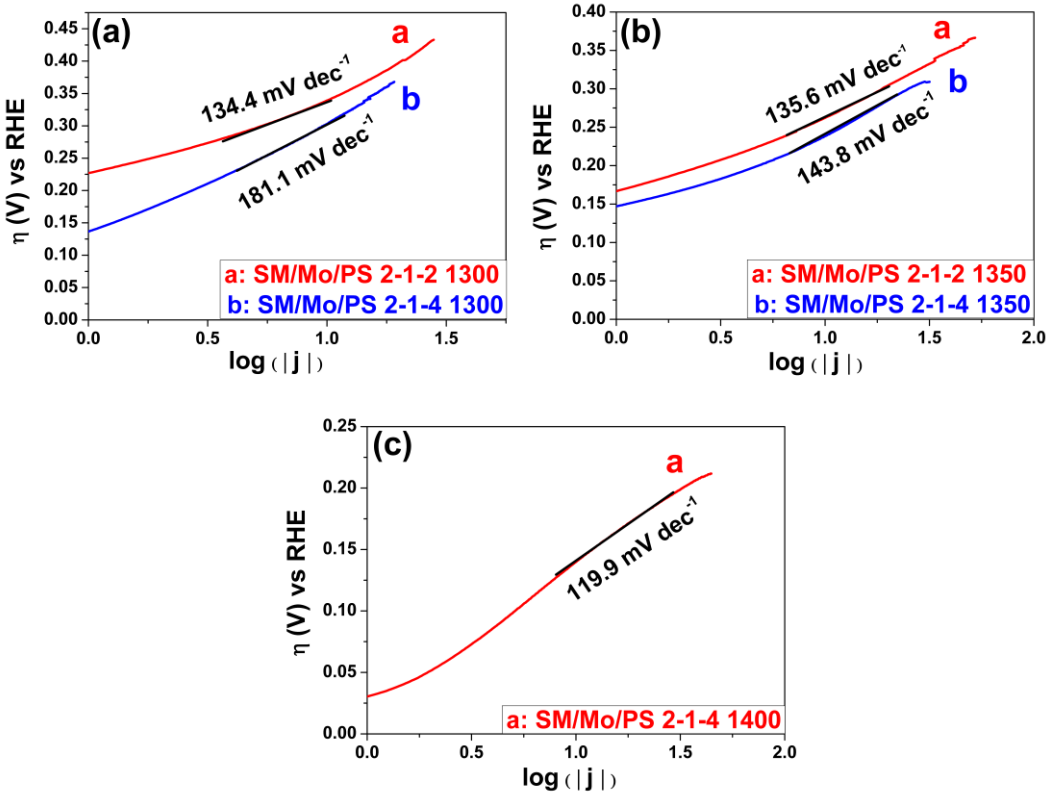

Figure 3. S2 Tafel slopes of ceramic samples derived from single-source-precursors with different PS content annealed at 1300 (a), 1350 (b) and 1400 °C (c).

Moreover, the HER performance measured in 0.5 M H_2SO_4 and surface area of all samples are listed in **Table 3. S1**.

Table 3. S1 The HER performance and surface area of all samples investigated.

Sample	η_1 Values (mV)	η_{10} Values (mV)	Tafel Slope (mV/dec)	Electrolyte Resistances (R) (Ω)	Specific Surface Area (SSA) (m^2/g)
SM/Mo/PS 2-1-0 1300	405	/	/	13.86	48.28
SM/Mo/PS 2-1-0 1350	289	/	/	21.23	25.14
SM/Mo/PS 2-1-0 1400	430	/	/	12.67	7.34
SM/Mo/PS 2-1-2 1300	220	338	94	14.74	80.37
SM/Mo/PS 2-1-2 1350	167	262	84	22.67	65.88
SM/Mo/PS 2-1-2 1400	250	/	/	19.19	38.35
SM/Mo/PS 2-1-4 1300	136	307	140	18.75	206.4
SM/Mo/PS 2-1-4 1350	148	239	71.6	14.68	178.7
SM/Mo/PS 2-1-4 1400	22	138	73.4	11.31	141.8

Electrolyte Resistances：R is the value for iR-correction

X-ray photoelectron spectroscopy (XPS) was performed to further analyze the chemical composition of the surface of the NP/C/SiC nanocomposites annealed at 1400 °C (denoted as sample SM/Mo/PS 2-1-4 1400) before and after the electrochemical measurements (**Figure 3. S3**). The sample before the electrochemical measurements contains Si, Mo, C and O [**Figure 3. S3** (a)]. As illustrated in **Figure 3. S3** (b), the C 1s emission features at about 283.1, 284.3, 285.0, 286.4 and 289.6 eV can be attributed to Si-C, C-C, C-O and C=O bonding, respectively [222]. Accordingly, the Si 2p emissions [**Figure 3. S3** (c)] at about 100.4 and 101.0 eV can be assigned to Si-C, while the other contributions of 101.7 and 102.8 eV results from oxidized species of Si (SiO_X) [223]. The Mo 3d photoemission line [**Figure 3. S3** (d)] shows two lines at 229.5 and 233.2 eV, which can be assigned to the Mo $3d^{5/2}$ and Mo $3d^{3/2}$ of Mo^{2+} related to Mo-C bonds. The two main emission lines at 232.7 and 235.5 eV are assigned to the Mo $3d^{5/2}$ and Mo $3d^{3/2}$ of Mo^{6+}, while the lines with binding energy of 231.3 and 233.9 eV have to be assigned to Mo^{4+} [26, 224]. The presence of Mo^{6+} and Mo^{4+} may be attributed to surface oxidation of the Mo species upon air exposure. After the electrochemical testing, the composition of the catalyst was again examined by XPS. Compared to the NP/C/SiC nanocomposites before the electrochemical measurements, additional characteristic emission lines of F (684.9 eV) and C-F (291.5 eV) are found in the XPS survey spectrum [**Figure 3. S3** (a')] and detail spectrum of C 1s [**Figure 3. S3** (b')], respectively. These emissions can be attributed to Nafion, which

was used for the electrode preparation as a binder material. Additionally, the C-C bonding feature in the C 1s peak is slightly increased, which is related to additional surface contaminations (adventitious carbon) during and after the electrochemical investigation. However, the characteristic emission features of Si 2p [**Figure 3. S3** (c')] are nearly unchanged - only a small oxidation of the Si can be detected (104 eV). The most significant change after the electrochemical testing is found for the Mo 3d photoemission line [**Figure 3. S3** (d')]. While the component of the Nowotny phase at 228.2 eV remains unchanged, the Mo oxide species are clearly reduced by the reducing conditions during the electrochemical reduction reaction. To confirm that the reduction of the Mo oxide species is due to the electrochemical testing an additional Mo 3d XPS spectrum after 2 h of stability testing was measured.

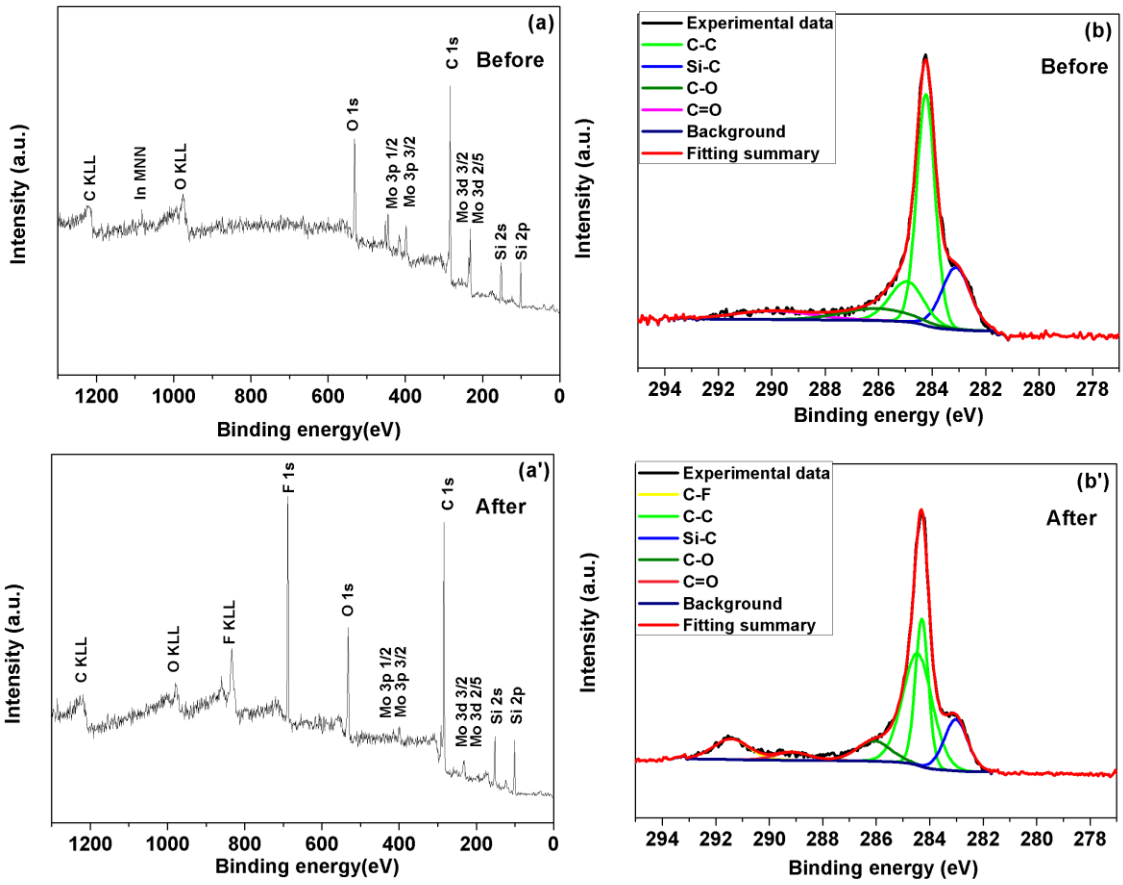

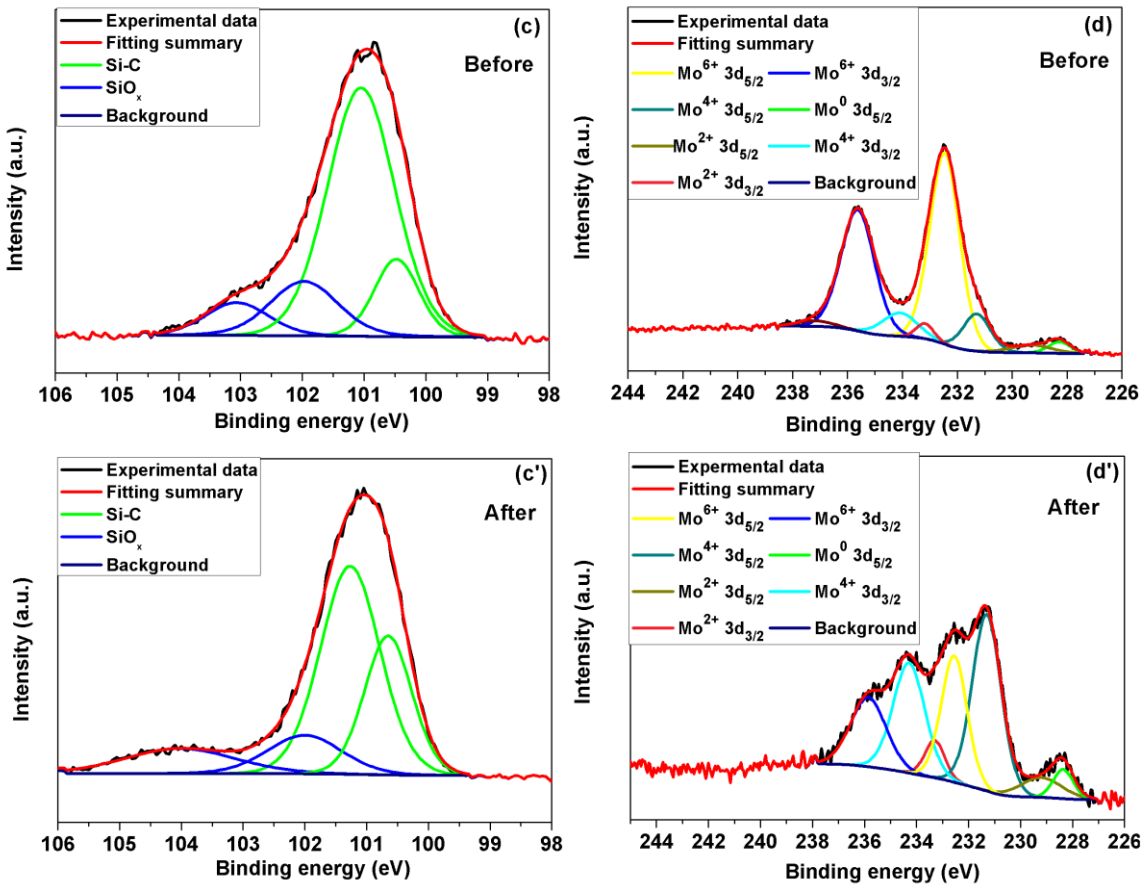

Figure 3. S3 XPS spectra of NP/C/SiC nanocomposites (SM/Mo/PS 2-1-4 1400) before the electrochemical measurements (a); High-resolution scans of C 1s (b), Si 2p (c) and Mo 3d (d) of SM/Mo/PS 2-1-4 1400 before the electrochemical measurements; XPS spectra of NP/C/SiC nanocomposites (SM/Mo/PS 2-1-4 1400) after the electrochemical measurements (a'); High-resolution scans of C 1s (b'), Si 2p (c') and Mo 3d (d') of SM/Mo/PS 2-1-4 1400 after the electrochemical measurements.

The comparison of the three Mo 3d measurements is shown in **Figure 3. S4**, normalized to the intensity of the Nowotny phase. During the 2 h stability measurement the Mo oxide species are further reduced in comparison to the Nowotny phase, leading to the assumption that the Nowotny phase is the active and stable phase in the compound. Furthermore, this assumption can be supported by Luo et al.[225], who showed that Mo (+VI) oxide is a poor HER catalyst in acidic solutions. These findings confirm, that the main chemical surface component of the NP/C/SiC nanocomposites - the Nowotny phase - remains unchanged before and after the electrochemical measurements, indicating excellent corrosion stability of the compound in acidic media.

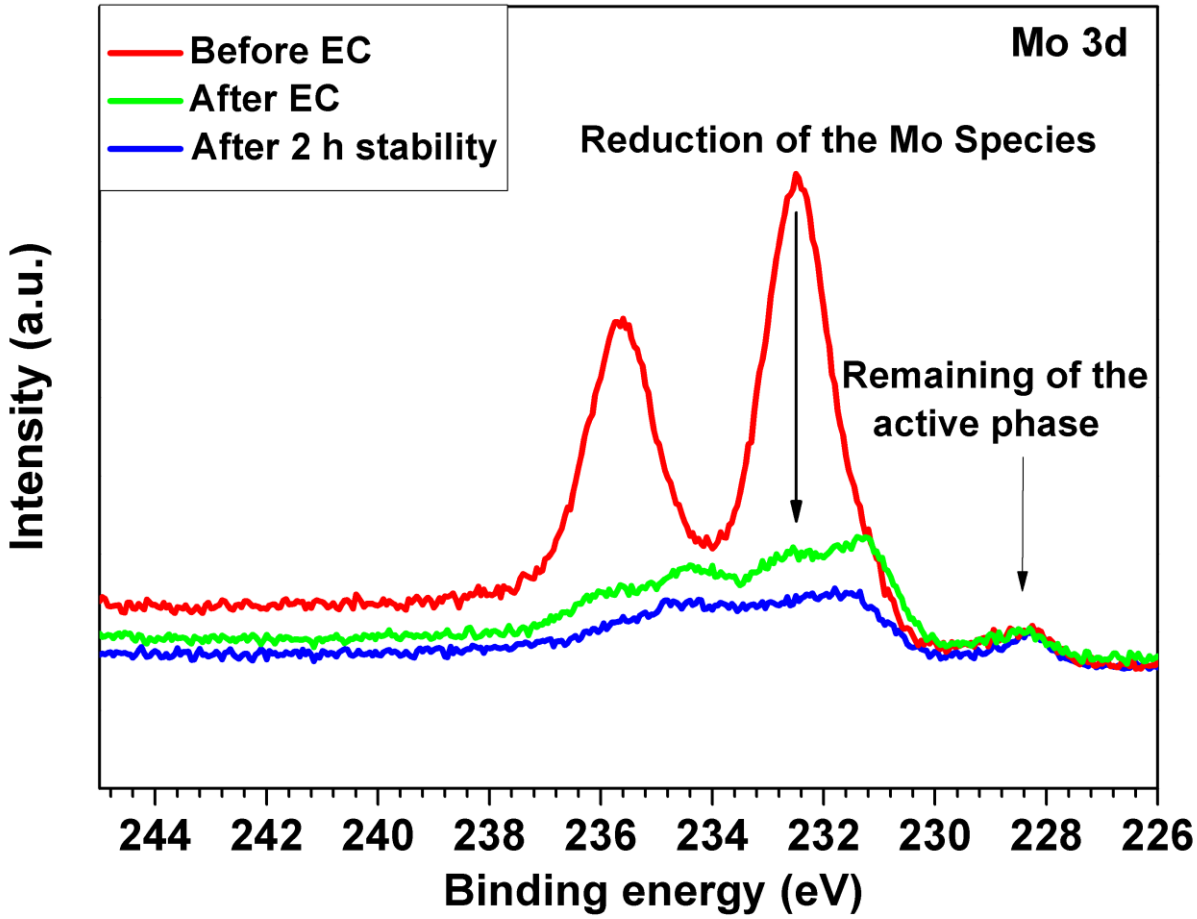

Figure 3. S4 The comparison of high-resolution scans of Mo 3d (SM/Mo/PS 2-1-4 1400) before and after the electrochemical measurements.

Figure 3. S5 shows the electrocatalytic properties of various Mo-based materials. The electrocatalytic activity of our novel NP/C/SiC nanocomposites is superior to most of all previously reported Mo-based electrocatalysts [20, 27, 31, 34, 101, 119, 124, 226-230].

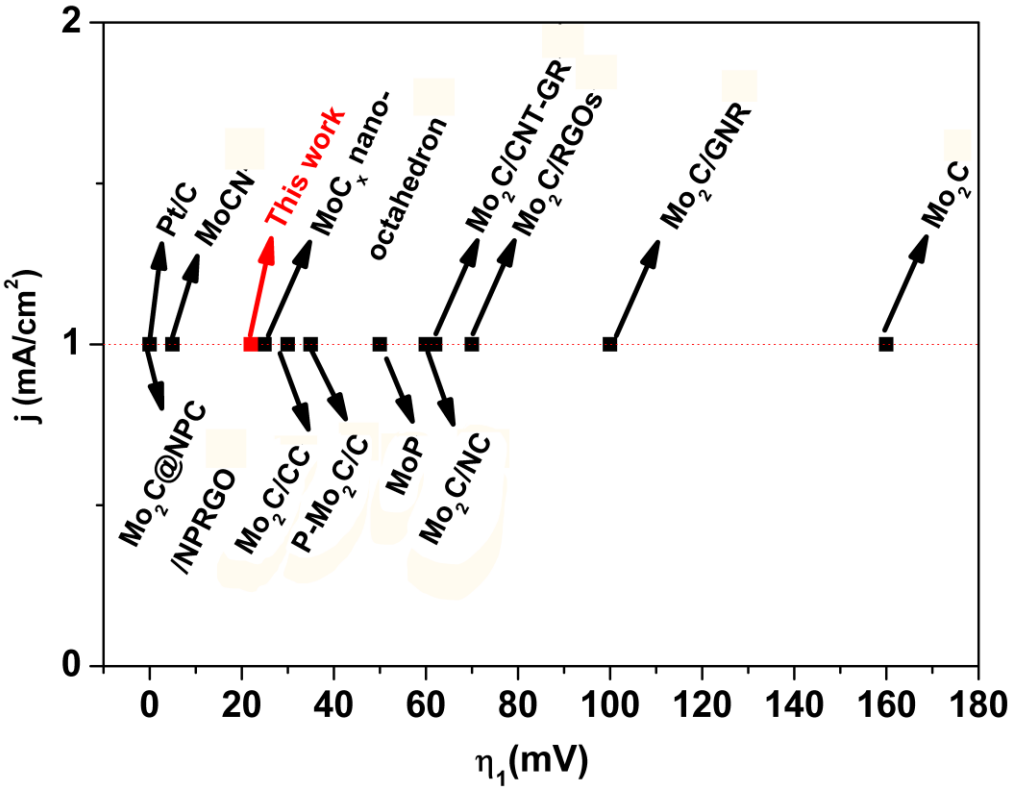

Figure 3. S5 Comparison of the electrochemical performance of the sample SM/Mo/PS 2-1-4 1400 with respect to η_1 with various Mo-based electrocatalysts in acidic solutions.

3.2 Enhanced hydrogen evolution reaction catalyzed by carbon-rich $Mo_{4.8}Si_3C_{0.6}$/C/SiC nanocomposites via a PDC approach

The content of this Chapter is published in:

2. Feng Y, Yu Z, Riedel R, Enhanced hydrogen evolution reaction catalyzed by carbon-rich $Mo_{4.8}Si_3C_{0.6}$/C/SiC nanocomposites via a PDC approach. *Journal of the American Ceramic Society*, 103 (2020) 1385–1395.

In our first part described in Chapter 3.1, for the first time we reported on the in-situ formation of a nano-sized Nowotny phase (NP) $Mo_{4.8}Si_3C_{0.6}$ embedded in a porous SiC/C-based matrix via a novel single-source-precursor approach. This is also the first time that the NP was discovered to possess electrocatalytic activity and excellent durability in terms of the HER. However, the poor electrical conductivity of SiC ceramics as catalyst support still limited the electrocatalytic activity of our NP/C/SiC ceramic nanocomposites. Therefore, to further improve the HER activity of the NP/C/SiC ceramic nanocomposites, DVB was used as a rich-carbon source to synthesize mesoporous NP/C/SiC ceramic nanocomposites with higher carbon content. The carbon-rich NP/C/SiC ceramic nanocomposites with high specific surface area were obtained at different pyrolysis temperatures. The obtained carbon-rich NP/C/SiC ceramic nanocomposite demonstrates superior HER performance with overpotentials as low as 119 mV vs. reversible hydrogen electrode at a current density of 10 mA cm^{-2} in acidic media.

3.2.1 Experimental section

3.2.1.1 Material synthesis

The Mo-containing precursor for the preparation of carbon-rich NP/C/SiC nanocomposites was synthesized using allylhydridopolycarbosilane (AHPCS, SMP-10, Starfire System Inc, Schenectady, NY) and bis(acetylacetonato) dioxomolybdenum (VI) [$MoO_2(acac)_2$] (Sigma Aldrich) as starting materials. Divinylbenzene (DVB, Sigma Aldrich) and polystyrene (PS, average Mw 35000, Sigma Aldrich) were used as the carbon-rich source and pore former, respectively. The synthesis procedure was carried out under an argon atmosphere (Schlenk technique) in order to prevent hydrolysis of the starting materials. 1.00 g $MoO_2(acac)_2$ was introduced into a 100 mL Schlenk flask in an argon atmosphere, and then 25 mL anhydrous toluene (Sigma Aldrich) was added to solve $MoO_2(acac)_2$ until a dark blue solution was obtained. Subsequently, 2.00 g SMP-10, 4.00 g PS and 2.00 g DVB were added to the Schlenk flask with stirring at room temperature for 30 min. After dispersing under ultrasound for another 10 min, the resultant solution was refluxed at 140 °C for 24 h in an argon atmosphere. Finally, a viscous dark yellow Mo-containing precursor was obtained after the solvent was stripped off under vacuum. The weight ratio of SMP-10/$MoO_2(acac)_2$/PS/DVB is 2/1/4/2 and the obtained samples are abbreviated as SM/Mo/PS/DVB 2-1-4-2.

Before pyrolysis, all Mo-containing precursors were cured at 170 °C for 2 h in an argon atmosphere. The pyrolysis of the as-cured precursors was then performed in a tube furnace. The cured sample was placed in an alumina boat and heated in a quartz glass tube under an argon flow. According to our previous work [72], after pyrolysis at 1100 °C for 2 h and subsequent annealing at elevated temperatures (1350-1600 °C) for 2 h in Ar, the NP/C/SiC ceramic nanocomposites with high carbon content were obtained.

3.2.1.2 Characterization of microstructure and composition

Attenuated total reflectance infrared (ATR-IR) spectra of the samples were recorded using a PerkinElmer Spectrum spotlight 200 Fourier transform infrared (FT-IR) spectrometer with a PerkinElmer single reflection UATR unit. The carbon and oxygen contents of the ceramics were measured by hot gas extraction techniques with a LECO C-200 and a LECO TC-436 analyzer (LECO Corporation, St. Joseph, MI), respectively. Mo and Si elemental contents were determined using Inductively Coupled Plasma-Atomic Emission Spectrometry (ICP-AES, Mikroanalytisches Labor Pascher, Remagen, Germany). Powder X-ray diffraction (XRD) experiments were recorded using a STADI P powder diffractometer (STOE & Cie GmbH, Darmstadt, Germany) with molybdenum Kα1 radiation source. Raman spectra were recorded from 400-4000 cm^{-1} employing a micro-Raman HR8000 spectrometer (Horiba JobinYvon, Bensheim, Germany) with a laser wavelength of 631.81 nm. The microstructural analysis of the nanocomposite powders was performed by scanning electron microscopy (SEM) on a Philips XL30 S-FEG microscope (FEI Company, Hillsboro, OR). Transmission electron microscopy (TEM) studies were conducted on ground powder samples using a JEM-2100 (JEOL Ltd, Tokyo, Japan) microscope at an acceleration voltage of 200 kV (wavelength 2.508 pm). The BET specific surface area of the ceramics was investigated by an Autosorb-3B Surface Area and Pore Size Analyzer (Quantachrome Instruments Corporation, Boynton Beach, FL) at -196 °C, after the powdered samples were out gassed at 100 °C for 24 h. The N_2 isotherm at -196 °C was used to calculate the specific surface area from the linear BET plots. The total pore volume was determined from the amount of vapor adsorbed at a relative pressure p/p_0 = 0.972. The micropore volume was calculated using de Boer's t-plot analysis.

3.2.1.3 Electrochemical measurements

Electrochemical characterization was carried out in a three-electrode setup using an Interface 1000 potentiostat from Gamry Instruments. All electrocatalysts were fixed by 5 wt% Nafion solutions on the top of glassy carbon electrodes with weight density of 0.95-1.00 mg/cm^2. Then, all catalysts were investigated in 0.5 M H_2SO_4 (Carl Roth, standard solution) as electrolyte according to a specified test procedure including the measurement of the open circuit potential (OCP), the electrochemical impedance spectroscopy (EIS) (10 Hz to 20 kHz) to obtain the setup resistance for iR compensation and the cyclic voltammogram (CV) recorded with a scan rate of 5 mV/s in the range of 0 V to -0.5 V. For comparison, measurements were also conducted using a commercial Pt/C catalyst exhibiting high HER catalytic performance. All potentials were referenced to a reversible hydrogen electrode (RHE), and the results were

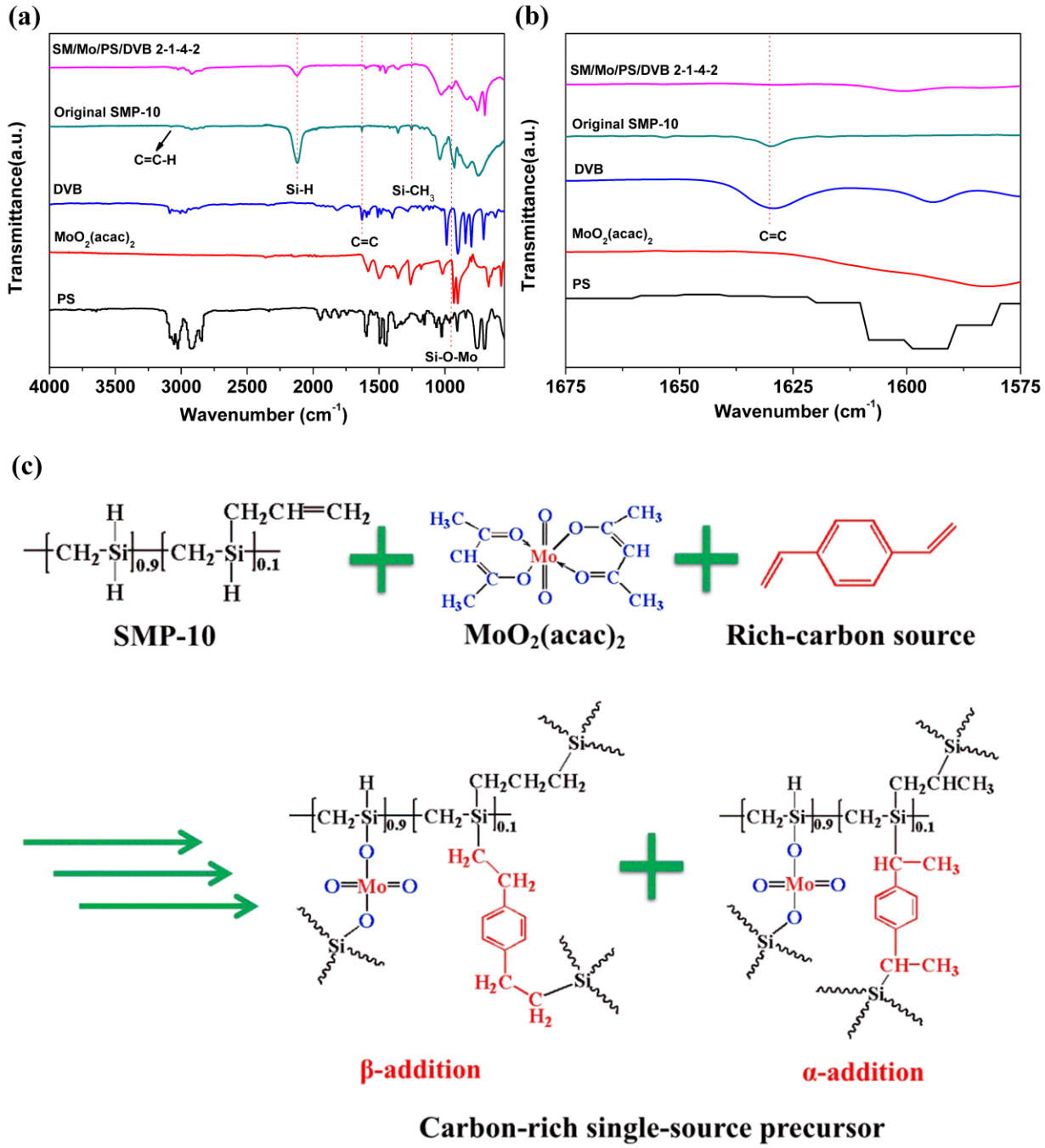

Figure 3. 11 FT-IR spectra of the original SMP-10, PS, $MoO_2(acac)_2$, DVB and the sample SM/Mo/PS/DVB 2-1-4-2 (a) with a magnification of the region between 1575 and 1675 cm^{-1} (b). Idealized reaction path (c) between SMP-10, $MoO_2(acac)_2$ and DVB to form the carbon-rich single-source precursor.

corrected for iR losses. Experimental EIS data were analyzed and fitted with the software of Zsimpwin to extract the series resistances (R_s) and charge-transfer resistances (R_{ct}). The double-layer capacitances (C_{dl}) were estimated by CV at various scan rates (10-50 mV s^{-1}) to evaluate the effective surface area of various catalysts. Other detailed process of electrochemical measurements was performed as same as described in our previous work [72].

3.2.2 Results and discussion

3.2.2.1 Characterization of the synthesized single-source precursor

The FT-IR spectra of SM/Mo/PS/DVB 2-1-4-2, $MoO_2(acac)_2$, PS, SMP-10 and DVB were measured, and the result is shown in **Figure 3. 11** (a). After annealing of the reaction mixture at 170°C for 2 h, the reaction between SMP-10 and $MoO_2(acac)_2$ results in the formation of Si-O-Mo bonds (950 cm^{-1}) by consuming Si-H groups (2136 cm^{-1}) of SMP-10, which has been discussed in our previous studies [72]. Besides, as compared with pure SMP-10 and DVB, the characteristic peaks of C=C (1627 cm^{-1}) in SM/Mo/PS/DVB 2-1-4-2 disappear [**Figure 3. 11** (b)], due to (i) hydrosilylation reaction (C=C/Si-H) between SMP-10 and DVB and (ii) self-hydrosilylation of SMP-10. PS as the pore former without functional groups cannot be involved in the chemical reaction between SMP-10, $MoO_2(acac)_2$ and DVB. Based on the FT-IR results and previous studies [72, 211], an idealized reaction scheme is shown in **Figure 3. 11** (c).

3.2.2.2 Composition of the ceramics

The elemental composition of the synthesized ceramics is shown in **Figure 3. 12**, including the weight fractions of carbon and oxygen contents of the ceramic samples derived from SM/Mo/PS/DVB 2-1-4-2 annealed at different temperatures, respectively. In our former study [72], the carbon contents of NP/C/SiC ceramic nanocomposites synthesized by Mo-containing precursors (SM/Mo/PS 2-1-4) without DVB in the feed at 1350 and 1400 °C are around 30 wt %, which is much lower than ca. 50 wt % of the present SM/Mo/PS/DVB 2-1-4-2 derived ceramic samples annealed at the same temperatures. The results clearly indicate that the much higher carbon content of the ceramics originates from the addition of DVB as the carbon source. Moreover, for the samples annealed between 1350 and 1600 °C, the carbon contents remain constant at ca. 52 wt%. The oxygen contents of the nanocomposites annealed at different temperatures is shown in **Figure 3. 12** (b). In the temperature range between 1350 and 1600 °C, the oxygen content of the samples (SM/Mo/PS/DVB 2-1-4-2) decreases from 5.22 wt % to 1.39 wt % with the increase of the annealing temperature due to the carbothermal reaction [214]. Additionally, taking the sample annealed at 1500 °C (denoted as sample SM/Mo/PS/DVB 2-1-4-2 1500) as an example, the Si and Mo contents amount 38.2 wt% and 9.48 wt%, respectively. Combining with the carbon (51.25 wt%) and oxygen (2.14 wt%) content of the ceramic sample SM/Mo/PS/DVB 2-1-4-2 1500, the free carbon content (35.98 wt%) can be calculated. Therefore, according to the reference [58], our SM/Mo/PS/DVB 2-1-4-2 derived ceramics can be defined as carbon-rich ceramics. Interestingly, the oxygen contents of the samples with DVB are lower than that of SM/Mo/PS 2-1-4 heat-treated at 1350 and 1400 °C, which could be explained by the fact that the higher free carbon content of the SM/Mo/PS/DVB 2-1-4-2 derived ceramic significantly enhances the carbothermal reaction (SiO_2+3C=SiC+2CO) to decrease the oxygen content.

The X-ray diffraction patterns of SM/Mo/PS/DVB 2-1-4-2 annealed at 1100-1600 °C are shown in **Figure 3. 13** (a). After pyrolysis at 1100 °C, the sample is X-ray amorphous. Annealing at elevated temperatures

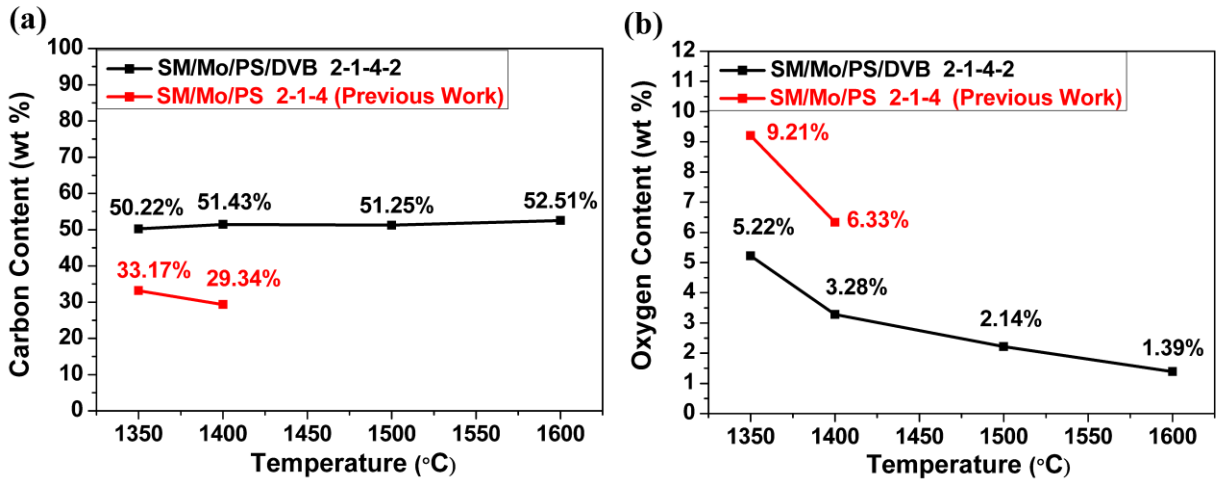

Figure 3. 12 Correlation between carbon content (a) and the oxygen content (b) with the corresponding annealing temperatures.

leads to the crystallization of the Nowotny phase (NP) [203] with a composition of $Mo_{4.8}Si_3C_{0.6}$ (JCPDS card no. 43-1199) and a sphalerite-type SiC (JCPDS card no. 49-1428). Similarly, to the previously reported NP/C/SiC ceramics with lower carbon content [72], increasing annealing temperature leads to a sharpening of the characteristic peaks of the NP and SiC, indicating an improved degree of crystallization. In addition, the characteristic diffraction peak of graphene-like carbon at 2θ = 12.06 ° (JCPDS card no.41-1487) is analyzed after annealing of the carbon-rich NP/C/SiC ceramics at 1350-1600 °C, due to the higher carbon content in the sample. Moreover, the weight fractions and average grain size of crystallized Nowotny and SiC phases at 1350-1600 °C are determined by Rietveld refinement of the XRD patterns of the ceramics with the Full Prof software. The peak shapes are modeled using Thompson-Cox-Hastings pseudo-Voigt function for average grain size and pseudo-Voigt function for weight fraction [231]. As depicted in **Figure 3. 13** (b), the weight fractions of NP significantly increase from 7.85 to 30.38 wt% with the increase of annealing temperature (1350-1500°C). However, annealing at higher temperature (1600 °C) leads to the decrease of the weight fraction of NP. On the other hand, as expected, the higher annealing temperature can lead to the growth of the average grain size, which is shown in **Figure 3. 13** (c). It is worth noting that, at 1600°C, the average crystallite sizes of the Nowotny phase (86.71 nm) and SiC phase (68.16 nm) increase but still remain smaller than 100 nm.

Raman spectra [**Figure 3. 13** (d)] of the samples pyrolyzed at 1100 °C and annealed at 1350-1600 °C reveal the presence of sp^2-bonded carbon at all temperatures. After annealing at 1350-1600 °C, the D (1350 cm^{-1}) and G (1580 cm^{-1}) bands show smaller line width than that of the sample pyrolyzed at 1100°C and the intensities of the G and 2D (2700 cm^{-1}) bands grow significantly, which indicates a progressive graphitization (increasing structural ordering) of the free carbon phase [218]. And the change in the intensities and the width of the Raman lines clearly indicate increasing order of carbon which is expected to improve the electronic conductivity of the electrocatalyst. The improvement of the electronic conductivity is the

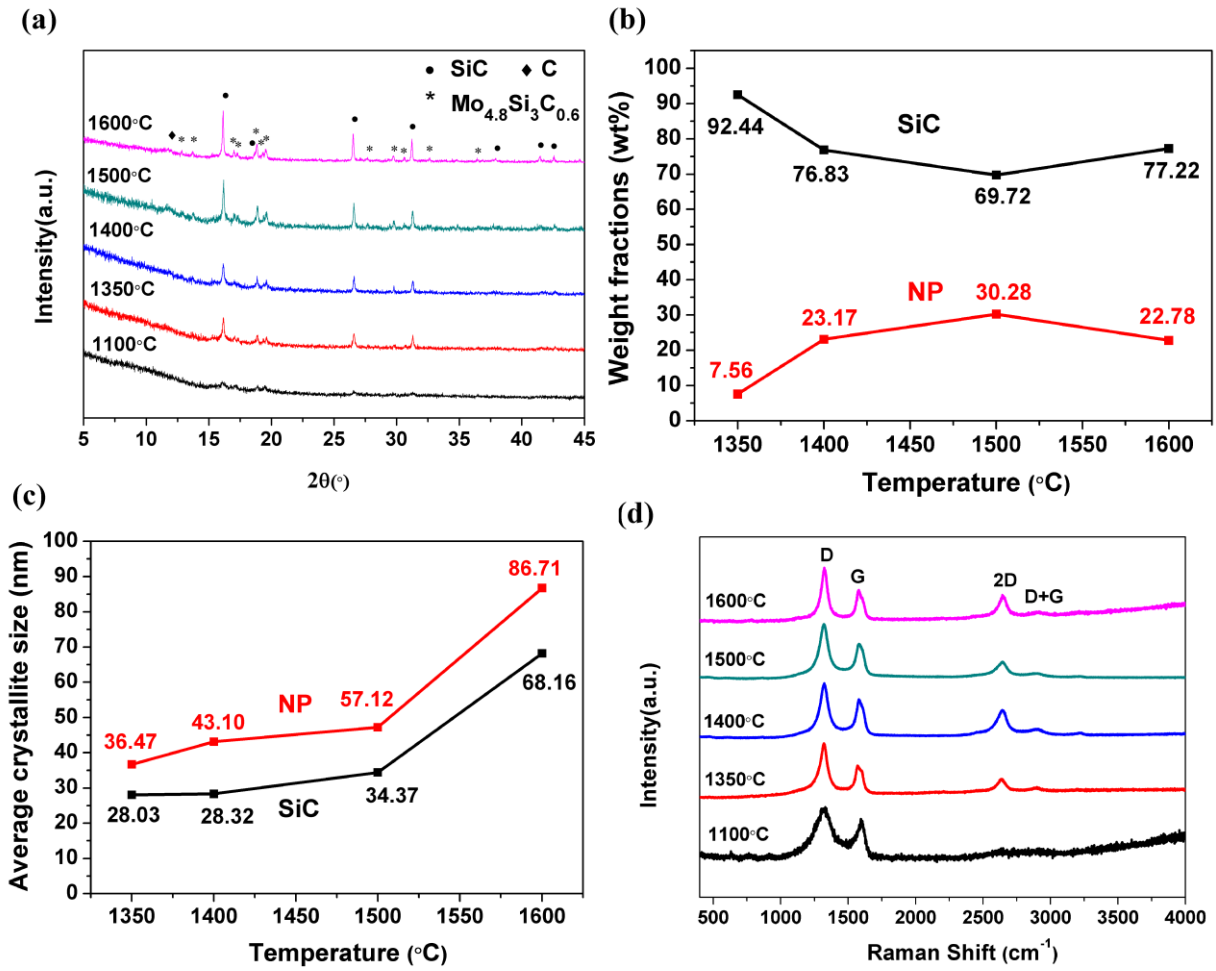

Figure 3. 13 (a) XRD patterns, (b) weight fractions, (c) average grain size and (d) Raman spectra of SM/Mo/PS/DVB 2-1-4-2 derived carbon-rich NP/C/SiC nanocomposites annealed at different temperatures.

goal of the present work and it's a significant requirement to enhance the electrocatalytic activity.

3.2.2.3 Microstructure of the ceramic nanocomposites

The synthesized carbon-rich NP/C/SiC ceramic nanocomposites annealed at 1500 °C were further studied by means of SEM and TEM (**Figure 3. 14**) in order to assess the microstructure at high temperatures. In **Figure 3. 14** (a, b), the SEM images of the ceramic prepared at 1500 °C shows an aerogel-like morphology, due to the porous structure which will be further confirmed via N_2 adsorption isothermal analysis. Moreover, the SEM images of samples annealed at different temperatures are presented in **Figure 3. S6**, which show that the porous morphology of carbon-rich NP/C/SiC ceramic nanocomposites is well maintained after annealing at different temperatures.

Similar to our previous work, the TEM image [**Figure 3. 14** (c)] of SM/Mo/PS/DVB 2-1-4-2 annealed at

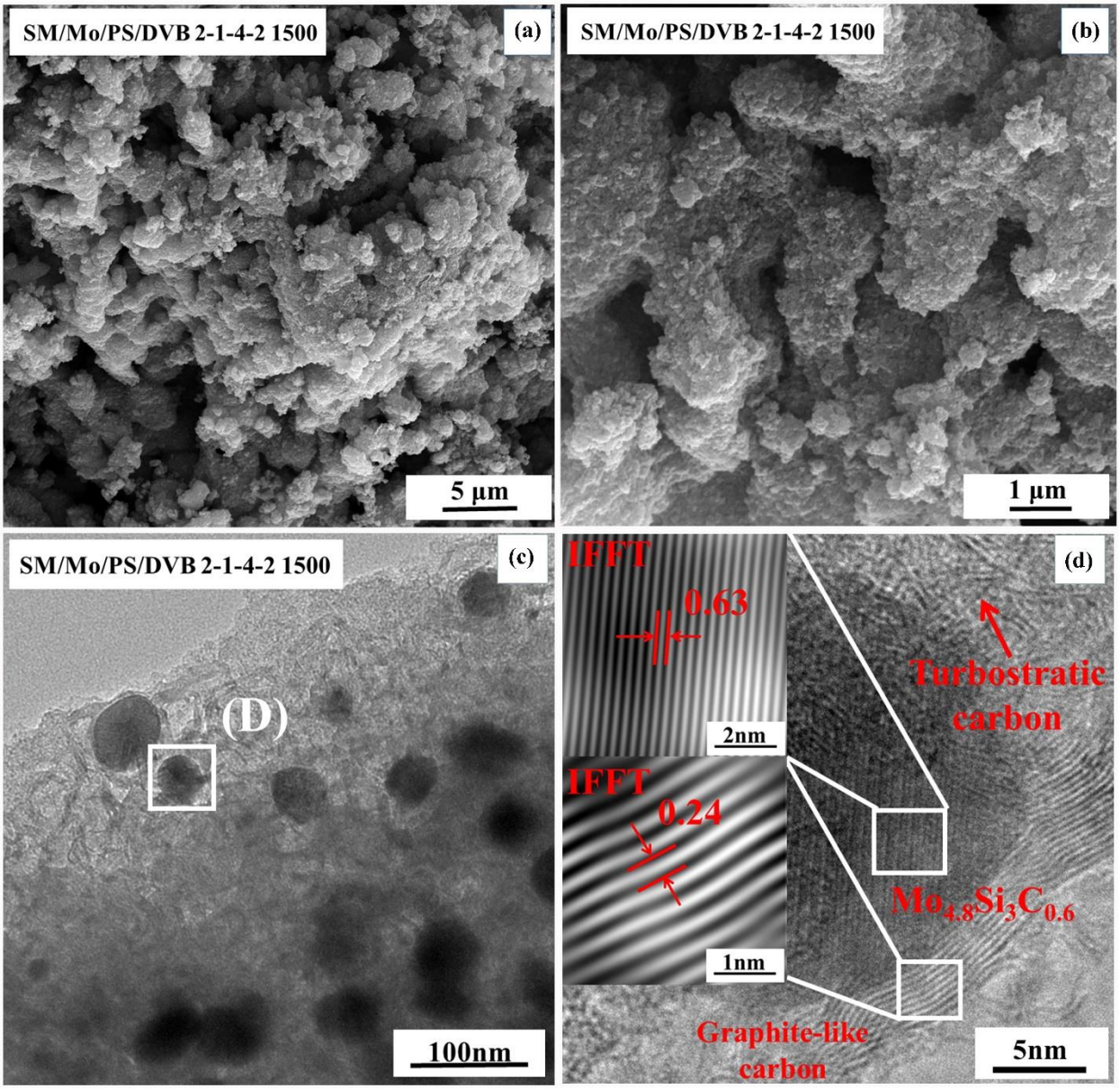

Figure 3. 14 SEM images (a, b), TEM (c) image and HRTEM image (d) of carbon-rich NP/C/SiC-based nanocomposites annealed at 1500 °C.

1500 °C reveals the presence of NP nanoparticles (dark contrast) with the size of < 100 nm embedded homogeneously within the β-SiC matrix. As depicted in **Figure 3. 14** (d), the high-resolution image shows a NP crystallite (lattice spacing of ca. 0.63 nm) with a size of about 20-30 nm, which reflects the nanoscaled microstructure and fulfills the definition of nanocomposites. Besides, the nano-sized NP core is encapsulated by plenty of graphite-like carbon shell (lattice spacing of ca. 0.34 nm) with an average thickness of ca. 4-5 nm. Moreover, some poorly organized turbostratic carbon is dispersed in an amorphous SiC matrix. As reported in the literature [232-233], the electrical conductivity of graphite-like carbon (10^3-10^5 S/m) is much higher than that of SiC (10^{-4}-10^{-2} S/m), thus the higher content of graphite-like carbon is expected to significantly improve the overall electrical conductivity and, thus, the electrocatalytic performance of the carbon-rich NP/C/SiC nanocomposites.

3.2.2.4 Porosity characteristics

According to the N_2 adsorption-desorption measurements, the SM/Mo/PS/DVB 2-1-4-2 derived carbon-rich NP/C/SiC nanocomposites heat-treated at different temperatures [**Figure 3. 15** (a)] reveal an intermediate characteristic type-IV isotherms, indicating the presence of meso-porosity. The specific surface area (SSA) of SM/Mo/PS/DVB 2-1-4-2 annealed at 1100 °C amounts 167.7 m^2/g, which is due to the decomposition and elimination of PS resulting in the formation of pores. Furthermore, increasing the temperature to 1350 °C, the SSA of the sample significantly increases to 304.0 m^2/g , since the higher free carbon content of carbon-rich NP/C/SiC ceramic increases the evolution of gas as a result/product of the carbothermal reaction which is the key factor in the formation of the porous structure [234]. Although the higher annealing temperature (1400~1600 °C) leads to viscous flow of the material decreasing the SSA [235-236], the sample (SM/Mo/PS/DVB 2-1-4-2 1600) annealed at 1600 °C still maintains a high SSA (214.6 m^2/g). Especially, after annealing at 1400 °C, the carbon-rich NP/C/SiC ceramics with DVB as

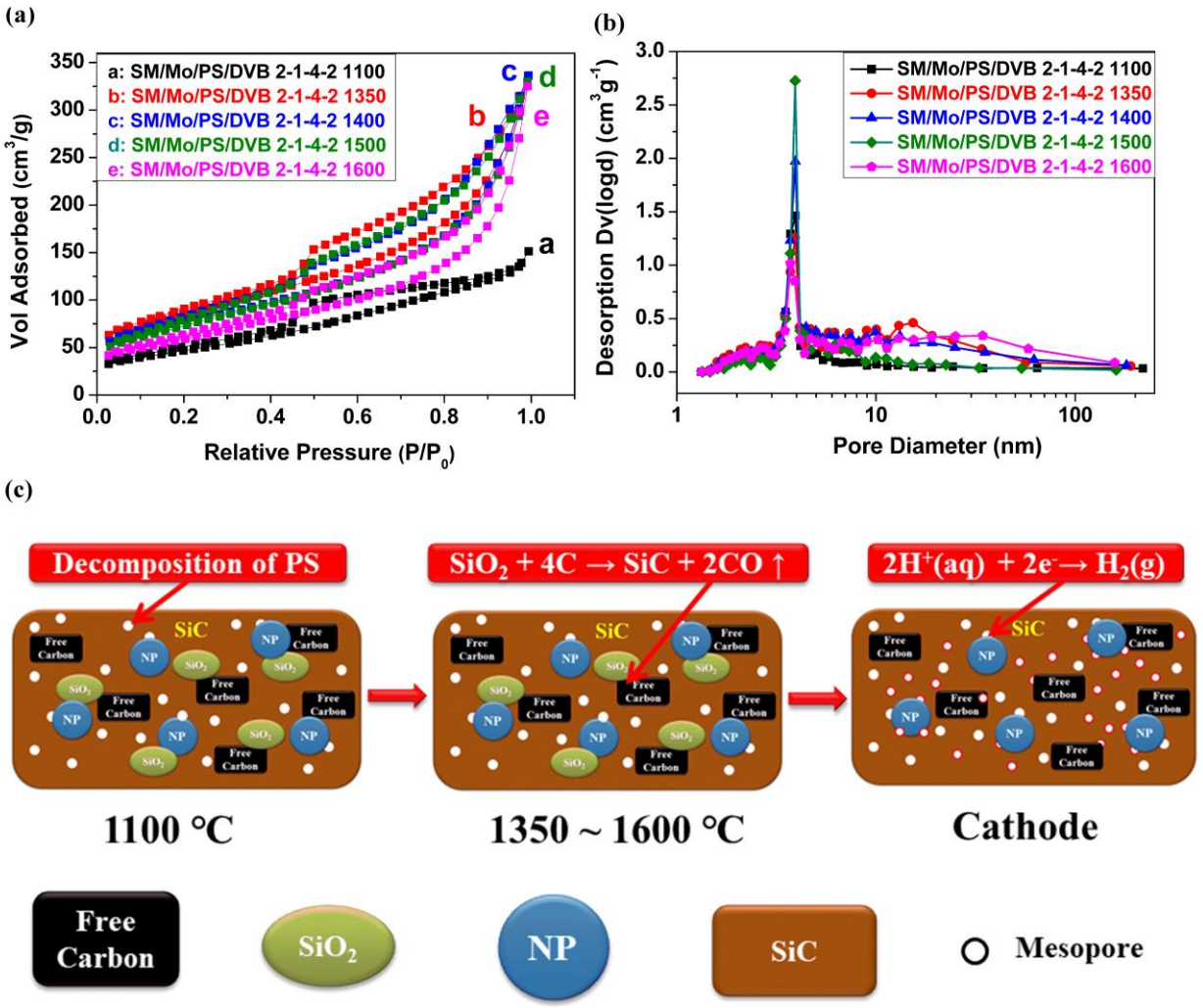

Figure 3. 15 N_2 adsorption-desorption isotherms (a) and pore size distribution (b) of the ceramic samples derived from SM/Mo/PS/DVB 2-1-4-2 annealed at different temperatures, schematic illustration (c) of the formation of the porous structure.

starting material maintains a higher SSA (SM/Mo/PS/DVB 2-1-4-2 1400, 268.3 m^2/g) as compared to that of the sample without DVB (SM/Mo/PS 2-1-4 1400, 141.8 m^2/g) in our previous work [72]. Moreover, **Figure 3. 15** (b) shows the corresponding pore size distributions, calculated based on the desorption branches of the isotherms of the ceramic samples derived from SM/Mo/PS/DVB 2-1-4-2 annealed at 1100 to 1600 °C. The average pore diameter of the samples is about 5-10 nm, which again confirms that the carbon-rich NP/C/SiC ceramic nanocomposites have a mesoporous (2-50 nm in pore diameter) feature. The specific surface area and average pore diameter of all samples are listed in **Table 3. S2**. In summary [**Figure 3. 15** (c)], the high SSA of the carbon-rich NP/C/SiC ceramic nanocomposites is due to (i) the decomposition of PS causing pore formation during pyrolysis below 1100 °C and (ii) the high amount of free carbon which increases the evolution of the carbothermal reaction in the temperature range between 1350 and 1600 °C. As reported in the case of other Mo-based electrocatalysts [220, 237-238], the high SSA is expected to significantly increase the number of additional active sites and to improve the electrocatalytic performance.

3.2.2.5 Electrocatalytic performance

The HER performance of the carbon-rich NP/C/SiC nanocomposites was evaluated using a typical three-electrode system in acidic conditions (0.5 M H_2SO_4). The optimized mass loading of the carbon-rich NP/C/SiC nanocomposites catalyst on a glassy carbon electrode was determined to 0.95-1.00 mg cm^{-2}. **Figure 3. 16** (a) shows polarization curves of samples annealed at different temperatures and that of commercial 20 wt% Pt/C. As a benchmark electrocatalyst, 20 wt% Pt/C exhibits the highest electrochemical activity for HER with a nearly zero onset over-potential. Moreover, all samples annealed at different temperatures reveal electrocatalytic activities. **Figure 3. 16** (b) shows the strong correlation between the electrocatalytic performance and the annealing temperature of the samples. Accordingly, with the annealing temperature increasing from 1350 to 1500 °C, the enhanced crystallinity of the NP phase as proofed by the XRD results leads to overpotentials (η_{10}) driving current densities of 10 mA cm^{-2} of the carbon-rich NP/C/SiC ceramic decreasing from 144 mV to 119 mV, although the increasing annealing temperature leads to a slight decrease of the SSA from 304 to 265.1 m^2/g. According to the results of the Rietveld refinement [**Figure 3. 13** (c)] and BET [**Figure 3. 15** (a)], the higher annealing temperature (1600 °C) can lead to growth of the average grain size (NP phase) and a remarkable decrease of the SSA (214.6 m^2/g), which explains the reducing electrocatalytic activity (η_{10}=205 mV). Particularly, compared to the best HER performance of the sample without DVB (SM/Mo/PS 2-1-4 1400, η_{10}=138 mV) from our previous work, after annealing at 1500 °C for 2 h, the sample SM/Mo/PS/DVB 2-1-4-2 1500 with DVB in the feed exhibits a strong improvement of the electrocatalytic activity in terms of the HER, reaching a current density of 10 mA cm^{-2} at ultra-small overpotentials of 119 mV.

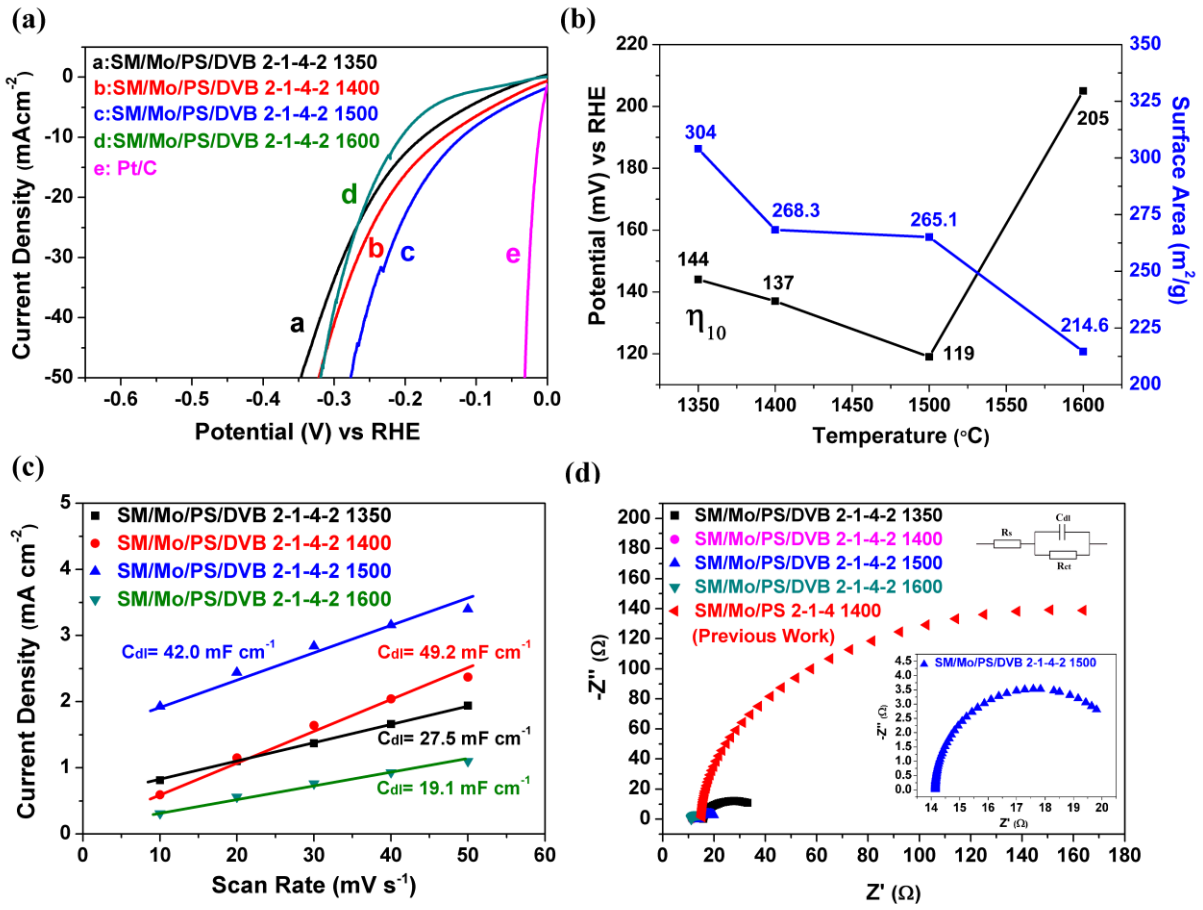

Figure 3. 16 Polarization curves (iR corrected) of the sample derived from SM/Mo/PS/DVB 2-1-4-2 annealed at different temperatures (a), correlation between overpotentials (η10) and BET specific surface area and the corresponding annealing temperatures from 1350 to 1600 °C (b), estimation of Cdl by plotting the current density variation against scan rate to fit a linear regression (c), Nyquist plots of the above electrocatalysts (d).

Electrochemical active surface area (ECSA) can be visualized through evaluating the double-layer capacitances (C_{dl}) derived from cyclic voltammograms (CVs, **Figure 3. S7**) curves due to their proportional relationship. As shown in **Figure 3. 16** (c), the capacitance values of the sample annealed at 1500 °C (SM/Mo/PS/DVB 2-1-4-2 1500) in 0.5 M H_2SO_4 is estimated to be 42 mF cm^{-2}, which is much higher than that of the C_{dl} of the sample annealed at 1350 (27.5 mF cm^{-2}) and 1600 °C (19.1 mF cm^{-2}). The large active surface may be ascribed to its porous structure with high BET area. To gain further insight into the electrochemical activity of carbon-rich NP/C/SiC nanocomposites for HER, EIS data of all samples and NP/C/SiC ceramic nanocomposites without DVB (SM/Mo/PS 2-1-4 1400) from our previous work are compared and the charge-transfer resistance values (R_{ct}) are obtained by utilizing the Zview software [**Figure 3. 16** (d) and **Table 3. S2**]. Compared with the Nyquist plot and R_{ct} value of the sample without DVB (SM/Mo/PS 2-1-4 1400 R_{ct} = 272.73 Ω), carbon-rich NP/C/SiC nanocomposites show much smaller semicircles. The R_{ct} of the sample with the best HER performance (SM/Mo/PS/DVB 2-1-4-2 1500) is only

7.46 Ω. The results imply good electron transport ability due to the existence of free carbon reducing the electrical resistance, and therefore accelerate the electron transfer. Besides, the linear portions of the Tafel plots are shown in **Figure 3. S8** and the HER performance of all samples are shown in **Table 3. S2**.

In summary, the results clearly indicate that the electrocatalytic performance of the novel NP/C/SiC nanocomposites catalyst can be enhanced via the addition of DVB as an additional carbon source due to following two contributions: (i) the increase of free carbon with the form as graphite-like carbon and turbostratic carbon (as proofed by the XRD, Raman spectra and TEM results) improves the overall electronic conductivity of the nanocomposites [239-240]; (ii) the enhanced carbothermal reaction increases the SSA (265.1 m^2/g) at higher temperatures, which enables the formation of additional active sites of the MoSiC electrocatalysts. Moreover, the obtained low overpotential of η_{10} (119 mV) is excellent if compared with that of Mo-related HER catalysts reported in the literature (**Table 3. S3**).

3.2.3 Conclusions

Within this work, mesoporous carbon-rich NP/C/SiC ceramic nanocomposites with both high total carbon content (above 50 wt %) and high free carbon content (36 wt%) has been synthesized via a polymer-derived ceramic route with the addition of DVB as additional carbon source. When annealed at high temperatures (1350-1600 °C), the carbon-rich NP/C/SiC ceramic nanocomposites still retain a high BET surface area in the range of 214.6-304 m^2/g due to the carbothermal reaction, leading to an excellent HER performance. The obtained η_{10} values of the sample SM/Mo/PS/DVB 2-1-4-2 1500 amounts 119 mV in acidic media, which are superior to that of NP/C/SiC ceramic nanocomposites without DVB (SM/Mo/PS 2-1-4 1400, η_{10}=138 mV) prepared in our previous work. In summary, the present study provides a promising strategy to develop porous materials with Nowotny phase ($Mo_{4.8}Si_3C_{0.6}$) as electrocatalyst for hydrogen evolution. The special charm of the developed method is based on suitable single source precursors, providing the electrocatalyst immobilized in a stable electronically conductive ceramic matrix with high porosity in one step. The process is considered to be adjusted or extended in future to various transition metal systems which are electrocatalytically active.

3.2.4 Supporting information

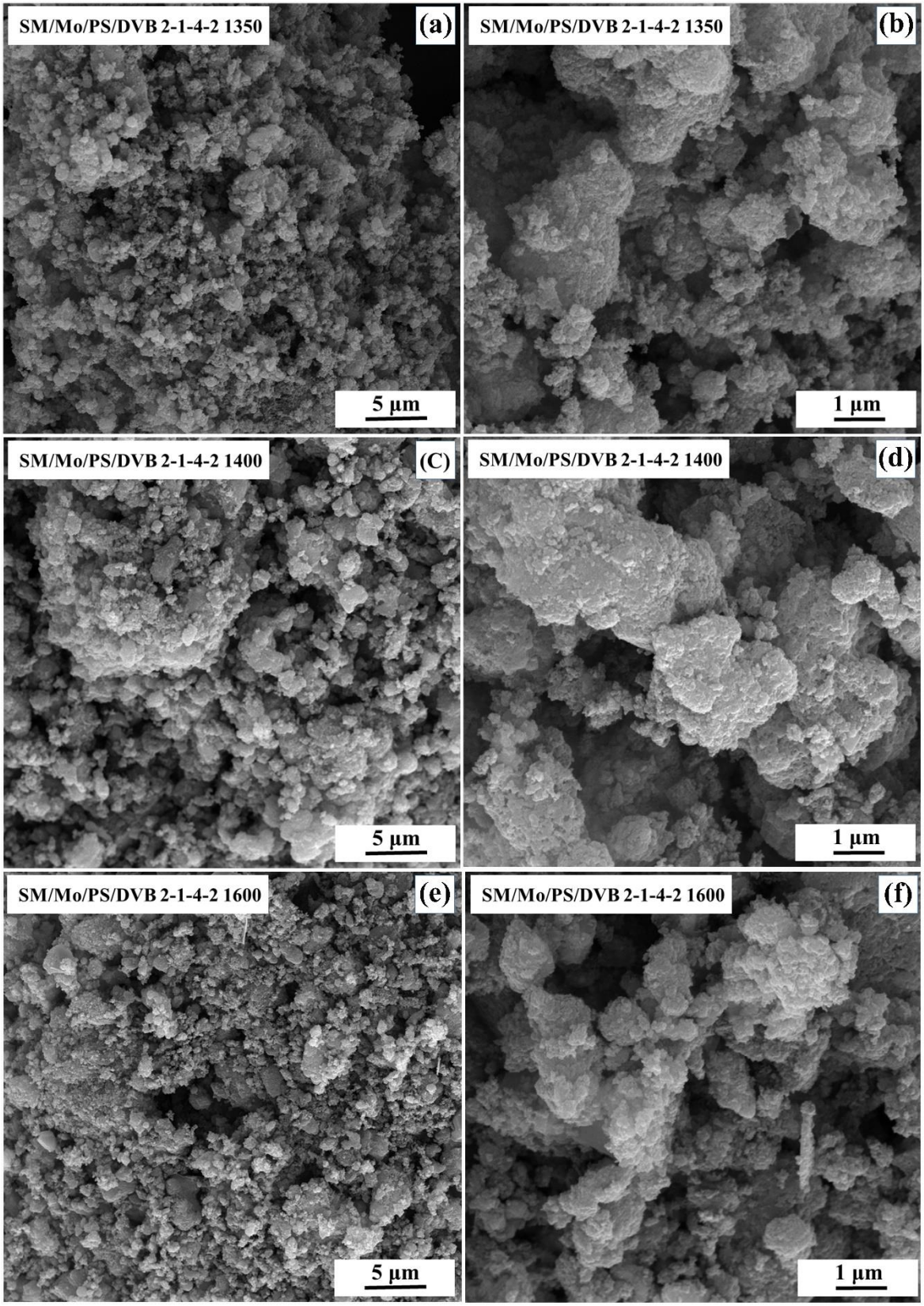

Figure 3. S6 SEM images of carbon-rich NP/C/SiC-based nanocomposites annealed at different temperatures.

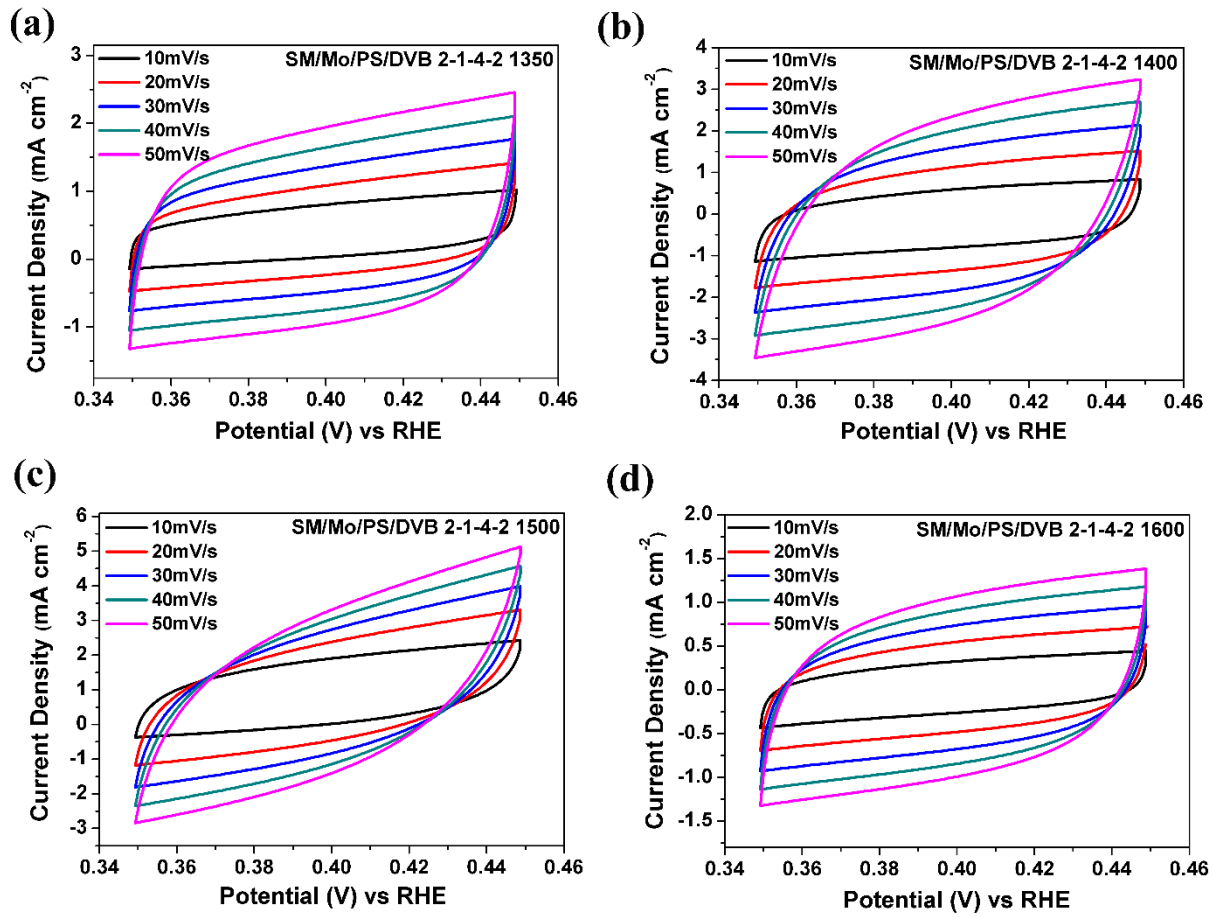

Figure 3. S7 Cyclic voltammograms (CVs) of carbon-rich NP/C/SiC-based nanocomposites annealed at 1350 (a), 1400 (b) 1500 (c) and 1600 °C (d) without redox current density peaks in 0.5 M H2SO4.

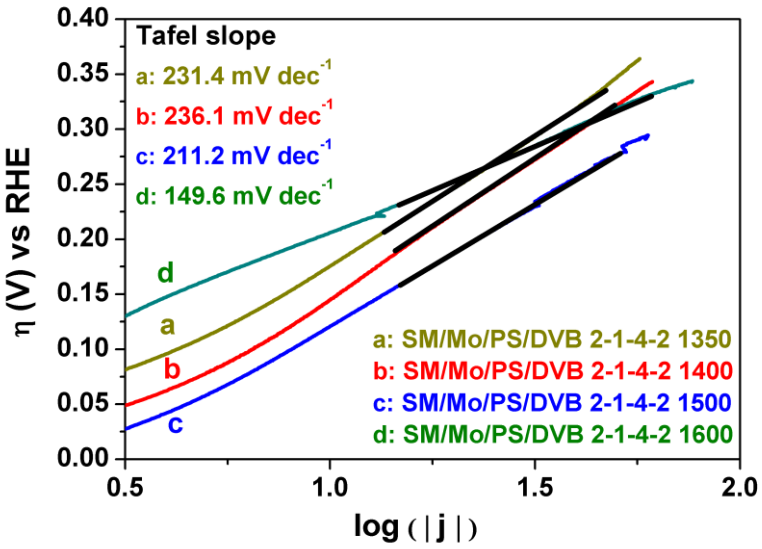

Figure 3. S8 Tafel slopes of carbon-rich NP/C/SiC-based nanocomposites at different temperatures.

Table 3. S2 HER performance and porosity of carbon-rich NP/C/SiC-based nanocomposites

Sample	η_{10} (mV)	Tafel Slope (mV/dec)	R_s (Ω)	R_{ct} (Ω)	SSA (m^2/g)	D_p (nm)
SM/Mo/PS/DVB 2-1-4-2 1100	/	/	/	/	167.7	5.59
SM/Mo/PS/DVB 2-1-4-2 1350	144	231.4	12.82	24.42	304.0	7.75
SM/Mo/PS/DVB 2-1-4-2 1400	137	236.1	11.26	3.34	268.3	7.74
SM/Mo/PS/DVB 2-1-4-2 1500	119	211.2	14.12	7.46	265.1	5.82
SM/Mo/PS/DVB 2-1-4-2 1600	205	149.6	10.72	6.42	214.6	9.37

R_s: Series Resistance R_{ct}: Charge-transfer Resistance

SSA: Specific Surface Area D_p: Average Pore Diameter

Table 3. S3 Comparison of HER activity of carbon-rich NP/C/SiC-based nanocomposites with the reported Mo-related electrocatalysts in acidic solution.

Electrocatalyst	Loading (mg cm^{-2})	η_{10} (mV)	Electrolyte solution
SM/Mo/PS/DVB 2-1-4-2 1500	0.95-1.00	119	0.5 M H_2SO_4
SM/Mo/PS 2-1-4 1400 [72]	0.95-1.00	138	0.5 M H_2SO_4
Mo/MoC_{1-x} nanorods [241]	2.1	140	0.5 M H_2SO_4
$Fe_{1.89}Mo_{4.11}O_7$ /MoO_2 [242]	/	125	0.5 M H_2SO_4
Mo_2C@NC@MoS_x [243]	~0.2	189	0.5 M H_2SO_4
Mo_xC-IOL [244]	~2.2	117	0.5 M H_2SO_4
Mo_2C-NCNTs [245]	~3	147	0.5 M H_2SO_4
Mo_2C@NC [27]	0.28	124	0.5 M H_2SO_4
Mo_2C/GCSs [28]	0.36	~200	0.5 M H_2SO_4
Mo_2C [20]	/	210	1 M H_2SO_4

3.3 Dielectric properties and electromagnetic wave absorbing performance of single-source-precursor synthesized $Mo_{4.8}Si_3C_{0.6}/SiC/C_{free}$ nanocomposites with an in-situ formed Nowotny phase.

The content of this Chapter is published in:

[3] Feng Y, Yang Y, Wen Q, Riedel R, Yu Z, Dielectric properties and electromagnetic wave absorbing performance of single-source-precursor synthesized $Mo_{4.8}Si_3C_{0.6}/SiC/C_{free}$ nanocomposites with an in-situ formed Nowotny phase. *ACS Applied Materials & Interfaces*, 2 (2020) 16912-16921.

In our first and second part described in Chapters 3.1 and 3.2, a porous $Mo_{4.8}Si_3C_{0.6}/SiC/C_{free}$ ceramic nanocomposite with in-situ formed $Mo_{4.8}Si_3C_{0.6}$ nanoparticles embedded in a β-SiC matrix was prepared via a single-source-precursor route. The as-synthesized $Mo_{4.8}Si_3C_{0.6}/SiC/C_{free}$ ceramic nanocomposites were discovered to possess excellent electrocatalytic activity and durability in terms of the hydrogen evolution reaction. Nevertheless, there is a lack of knowledge concerning the phase evolution of in-situ formed $Mo_{4.8}Si_3C_{0.6}$ in SiC/C-based ceramics [246]. Therefore, in this work, the chemical/phase composition as well as the microstructural evolution of $Mo_{4.8}Si_3C_{0.6}$/SiC-based nanocomposites annealed at 1100 - 1600 °C were studied in more detail. Besides, for the first time, we investigated the dielectric properties of the $Mo_{4.8}Si_3C_{0.6}/SiC/C_{free}$ nanocomposites and evaluated their EMA performance. The correlation between the free carbon (C_{free}) content and in-situ formation of $Mo_{4.8}Si_3C_{0.6}$ as well as their influence on the dielectric properties of the formed $Mo_{4.8}Si_3C_{0.6}/SiC/C_{free}$ nanocomposites is discussed.

3.3.1 Experimental section

3.3.1.1 Synthesis of Mo-containing composition

Figure 3. 17 shows the fabrication process of Mo-containing compositions by a single-source precursor approach starting from the reactions between allylhydridopolycarbosilane (SMP-10, Starfire, Schenectady, NY), $MoO_2(acac)_2$ (Sigma Aldrich, Merck KGaA, St. Louis, Missouri, USA) and divinylbenzene (DVB, Sigma Aldrich). Taking SMC-D1-1500 ºC as an example, typical synthesis process of the $Mo_{4.8}Si_3C_{0.6}/SiC/C$ nanocomposites is described as follows: initially, 1.00 g $MoO_2(acac)_2$ was placed into a Schlenk flask (100 mL) under the Ar atmosphere, and then 25 mL anhydrous toluene purchased from Sigma Aldrich was introduced to dissolve $MoO_2(acac)_2$ until a well-mixed solution (dark blue) was obtained. Afterward, SMP-10 (2.00 g) and DVB (1.00 g) were added to the above as-prepared blue solution. Then, it is stirred at room temperature for 30 min and sonicated for a further 10 min to obtain a well-distributed solution. The resultant solution was heated at 140 °C for 24 h under the Ar atmosphere. After removal of toluene in vacuum, a viscous Mo-containing single-source precursor (dark yellow) was synthesized. Finally, after pyrolysis at 1100 °C for 2 h and subsequent annealing at 1500 °C for 2 h in Argon, $Mo_{4.8}Si_3C_{0.6}/SiC/C_{free}$ nanocomposites (SMC-D1-1500 ºC) were obtained. Other detailed synthesis conditions can be found in Chapter 3.1 and 3.2. Sample notations, weight ratio of the reactants as well as

the annealing temperature are listed in **Table 3.1**.

Table 3. 1 Sample notations, weight ratio of the reactants and final annealing temperature applied for the synthesis of ceramic nanocomposites.

Sample	Weight ratios in the feed for precursor synthesis			Annealing Temperature
	SMP-10	$MoO_2(acac)_2$	DVB [a]	
SMC-1100 ºC	2	1	/	1100 ºC
SMC-1300 ºC	2	1	/	1300 ºC
SMC-1400 ºC	2	1	/	1400 ºC
SMC-1500 ºC	2	1	/	1500 ºC
SMC-1600 ºC	2	1	/	1600 ºC
SMC-D1-1500 ºC	2	1	1	1500 ºC
SMC-D2-1500 ºC	2	1	2	1500 ºC
SC-1500 ºC [b]	1	/	/	1500 ºC
SC-D2-1500 ºC [b]	1	/	1	1500 ºC

a: To investigate the influence of C_{free} content on the phase composition of the ceramics, divinylbenzene (DVB, Sigma Aldrich) was used as a carbon source [73].

b: For the sake of comparison, two ceramic samples (SC-1500 ºC and SC-D2-1500 ºC) without Mo have been synthesized using pure precursor (SMP10) and carbon-rich precursor (SMP10/DVB: 1/1), respectively.

3.3.1.2 Characterization

The crystal structures of the samples were tested by an X-ray diffraction (XRD) with a STADI P powder diffractometer (STOE & Cie GmbH, Germany) using Mo radiation source. A micro-Raman HR8000 spectrometer (Horiba JobinYvon, Germany) was employed to record Raman spectra (500 - 4000 cm^{-1}). The O and C contents of the samples were analyzed by means of hot gas extraction and combustion analysis using a LECO TC-436 and a LECO C-200 analyzer (LECO, St. Joseph, MI), respectively. Mo and Si contents were analyzed using Inductively Coupled Plasma-Atomic Emission Spectrometry (ICP-AES, Mikroanalytisches Labor Pascher, Germany). The morphology of typical ground powder samples was studied by transmission electron microscopy (TEM, JEM-2100, JEOL Ltd, Japan). The electrical conductivity of the samples (thickness: 2 mm, diameter:10 mm, ceramic/paraffin wax: 4/6) has been measured by a Solartron 1260 Impedance Analyzer with 1287 Electrochemical Interface in the frequency range of 0.1 Hz - 1 MHz.

3.3.1.3 Dielectric measurements

The dielectric measurements of the Mo-containing ceramics are shown in **Figure 3. 17**. The complex permittivity has been determined by the coaxial transmission/reflection method in the range of 2 - 18 GHz. The samples used for measurements were prepared by mixing molten paraffin wax (60 wt%) with the ceramic powders (40 wt%) and then pressing into hollow cylinder-shaped coaxial rings (external diameter:

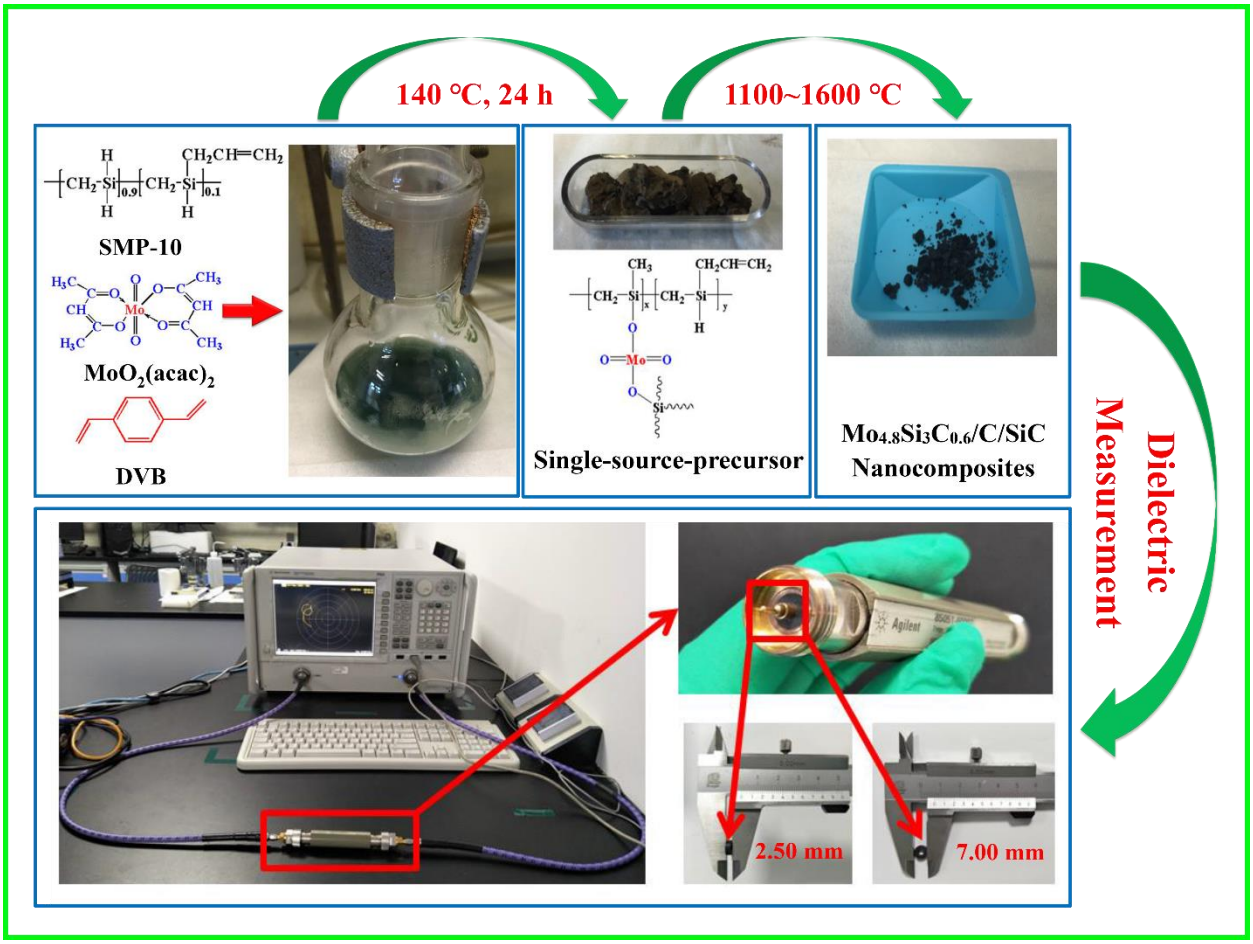

Figure 3. 17 Schematic illustration of dielectric measurements of as-obtained Mo-containing ceramics.

0.70 cm, inner diameter:3.04 mm, thickness: 2.50 mm). The pure paraffin wax is an insulator whose real and imaginary parts of the permittivity are around 2.26 and 0, respectively [247]. The volume percent of the ceramic powders within the ceramic-paraffin composites amount ca. 15 vol%. In order to remove adsorbed water, all ceramic powders were ball-milled and then placed into an oven (60 °C) for 24 h. The complex permittivity (ε'-$j\varepsilon''$) and permeability (μ'-$j\mu''$) of the samples were calculated from the scattering parameters corresponding to reflection (S_{11} and S_{22}) and transmission (S_{21} and S_{12}) determined on a Vector Network Analyzer (N5222A PNA-X, Agilent, CA). As shown in Figure 1, the hollow cylinder-shaped samples with an external diameter of 7.00 mm and inner diameter of 3.04 mm were tightly installed in the 50 Ω Airline (85051-60007, Agilent). An electronic calibration module (N4696-60004, 300 kHz-18 GHz, Agilent) was used to calibrate the dielectric measurements. The experimental errors of all scattering parameters are less 3%.

3.3.2 Results and discussion

3.3.2.1 Composition of the synthesized ceramics

The chemical analysis data and phase composition of the as-prepared Mo-containing ceramics are shown in **Table 3.2**.

Table 3. 2 Elemental analysis data and empirical chemical composition of the synthesized Mo-containing SiC-based nanocomposite ceramics.

Content (wt%)					
Sample	**Si**	**Mo**	**C**	**O**	**Empirical Formula**
SMC-1300 ºC	53.84[a]	16.59[a]	18.98	10.59	$SiMo_{0.09}C_{0.82}O_{0.34}$
SMC-1400 ºC	58.10	17.85	19.47	3.83	$SiMo_{0.09}C_{0.78}O_{0.12}$
SMC-1500 ºC	59.60	18.40	19.53	1.56	$SiMo_{0.09}C_{0.76}O_{0.05}$
SMC-1600 ºC	60.71[a]	18.71[a]	20.09	0.49	$SiMo_{0.09}C_{0.77}O_{0.01}$
SMC-D1-1500 ºC	51.25	15.50	30.66	1.01	$SiMo_{0.09}C_{1.40}O_{0.30}$
Phase Composition (wt%) [b]					
Sample	**SiC**	**$MoSi_2$**	**$Mo_{4.8}Si_3C_{0.6}$**	**SiO_2**	**Free Carbon**
SMC-1300 ºC	59.37	/	19.87	19.84	0.92
SMC-1400 ºC	64.05	26.15	1.96	7.18	0.66
SMC-1500 ºC	67.00	29.99	/	3.01	/
SMC-1600 ºC	69.02	30.03	/	0.95	/
SMC-D1-1500 ºC	68.99	/	18.87	1.93	10.21

a: As proven by the elemental analysis of samples SMC-1400 ºC and SMC-1600 ºC, no loss of Mo has been detected and the atomic ratio of Si/Mo remains constant during the fabrication process of ceramics. Therefore, the atomic ratio of Si to Mo as well as Si and Mo content of SMC-1400 ºC and SMC-1600 ºC can be determined from the atomic ratio of Si/Mo of SMC-1400 ºC and SMC-1500 ºC.

b: The phase composition of the Mo-containing ceramics is calculated based on the elemental analysis and XRD results.

The C and O contents of the SMC-1300 ºC, SMC-1400 ºC, SMC-1500 ºC, SMC-1600 ºC ceramics are shown in **Figure 3. 18** (a). When the heat temperature increases from 1300 to 1600 °C, the C content remains around 20 wt%, while the O content decreases significantly from 10.59 wt% to 0.49 wt% with increasing annealing temperature. The decreasing oxygen content is because of the carbothermal reaction which occurs between C_{free} and oxygen containing phase (such as SiC_xO_y) [248]. **Figure 3. 18** (b) shows that the addition of DVB leads to a remarkable increase of the carbon content from 19.53 wt% to 43.55 wt%. The C_{free} content of sample SMC-D1-1500 ºC reveals that the addition of 25 wt% DVB in the feed, effectively enhanced the C_{free} content by ca. 10 wt%.

The XRD patterns of SMC ceramics obtained at 1100 - 1600 °C are presented in **Figure 3. 19** (a). The SMC-1100 ºC is amorphous. Within the SMC-1300 ºC, reflection peaks of the β-SiC and $Mo_{4.8}Si_3C_{0.6}$ (JCPDS card, no. 43-1199) [203] are identified. However, after annealing at 1400 and 1500 ºC, the $Mo_{4.8}Si_3C_{0.6}$ phase gradually transformed into $MoSi_2$. The weight fractions of crystallized $Mo_{4.8}Si_3C_{0.6}$,

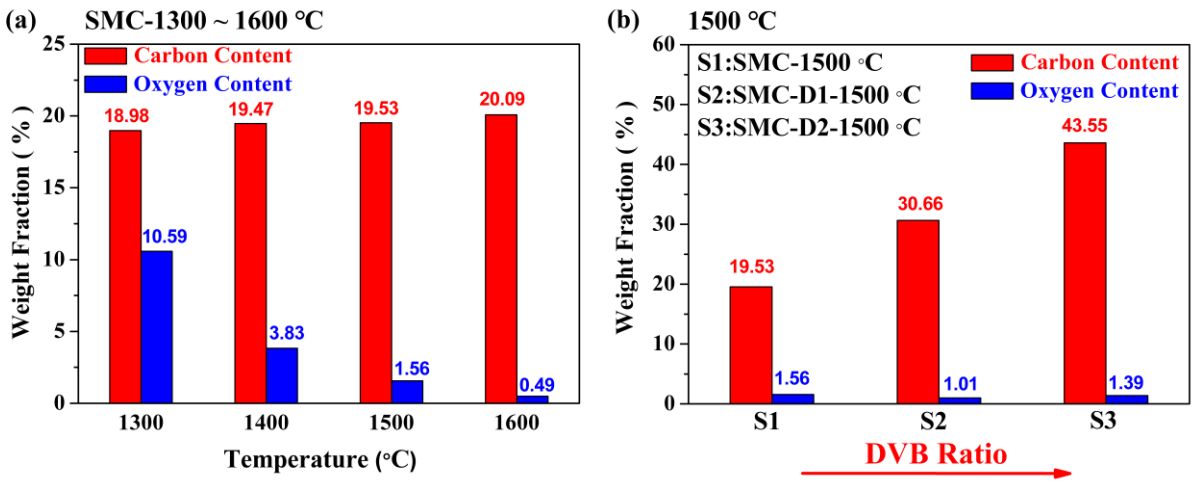

Figure 3. 18 Correlation of the annealing temperatures (a) and different DVB contents in the feed (b) with the corresponding O and C content of samples.

$MoSi_2$ and SiC phases formed in the temperature range from 1300 to 1600 °C are determined according to the results of Rietveld refinement and shown in **Figure 3. 19** (b) (detailed information is given in **Figure 3. S9**). The peak shapes modeled for weight fractions are based on pseudo-Voigt function [231]. As shown in **Figure 3. 19** (b), annealing at 1300 - 1500 °C decreases the weight fraction of $Mo_{4.8}Si_3C_{0.6}$ from ca. 27 to ca. 0 wt%, while the weight fractions of $MoSi_2$ remarkably increase from ca. 0 to ca. 31 wt% with the increase of the heating temperature (1300 - 1600 °C). The $Mo_{4.8}Si_3C_{0.6}$ phase completely disappeared after annealing at temperatures beyond 1500 °C. Interestingly, as shown in **Figure 3. 19** (c), when DVB was introduced into the preceramic precursors, $Mo_{4.8}Si_3C_{0.6}$ is stable even at 1500 °C, and no $MoSi_2$ was detected. After further increasing the DVB ratio in the feed, the $Mo_{4.8}Si_3C_{0.6}$ content increases to 35.15 wt% [**Figure 3. 19** (d)]. The results suggest that the existence of C_{free} strongly suppresses the phase decomposition of $Mo_{4.8}Si_3C_{0.6}$ into $MoSi_2$, which can be explained based on the following equilibrium reaction [206].

$$6.6\ SiC + Mo_{4.8}Si_3C_{0.6} \leftrightharpoons 4.8\ MoSi_2 + 7.2\ C \qquad \textbf{Eq. (3.1)}$$

As shown in **Table 3. 2**, the C_{free} content of the samples SMC-1400 ºC (0.66 wt%) and SMC-1500 ºC (ca. 0 wt%) are becoming rather low due to the carbothermal reaction during annealing. Therefore, the equilibrium of reaction equation **Eq. (3.1)** is shifted to the $MoSi_2$ product side, while in the presence of C_{free} as in the DVB containing samples, the Nowotny phase is stabilized. In summary, the phase evolution between $Mo_{4.8}Si_3C_{0.6}$ and $MoSi_2$ during annealing at 1300 - 1600 °C can be rationalized by the schematic illustration shown in **Figure 3. 19** (e). The C_{free} content plays a key role in the formation and thermal stabilization of the Nowotny phase $Mo_{4.8}Si_3C_{0.6}$. As the C_{free} content can be tailored via molecular design of the precursors (e.g. DVB addition), the phase composition of the $Mo_{4.8}Si_3C_{0.6}/SiC/C_{free}$ can be adjusted accordingly.

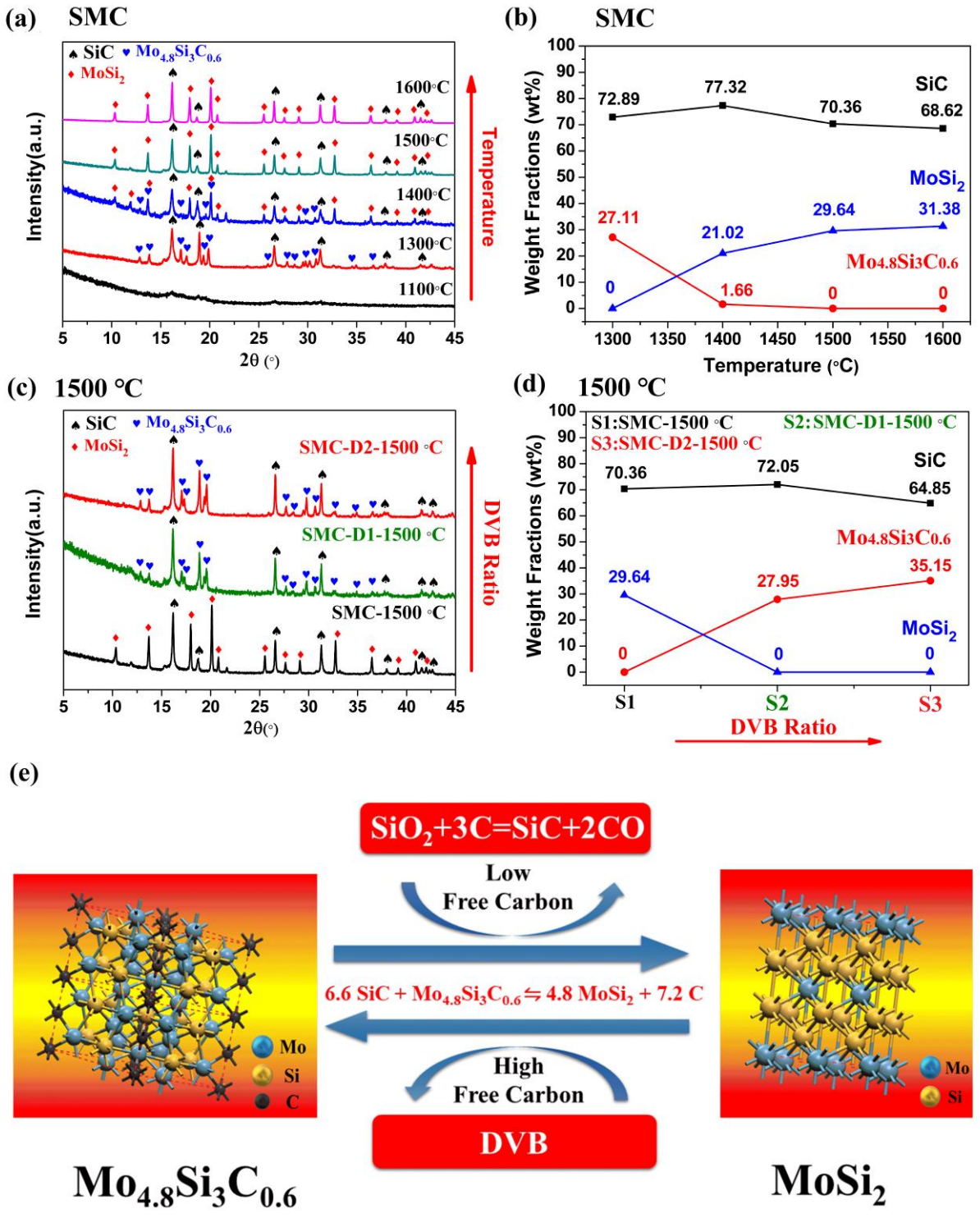

Figure 3. 19 XRD patterns (a, c) and weight fractions (b, d) of SMC ceramics annealed at different temperatures and with different DVB contents, respectively, schematic illustration (e) of the phase evolution between $Mo_{4.8}Si_3C_{0.6}$ and $MoSi_2$.

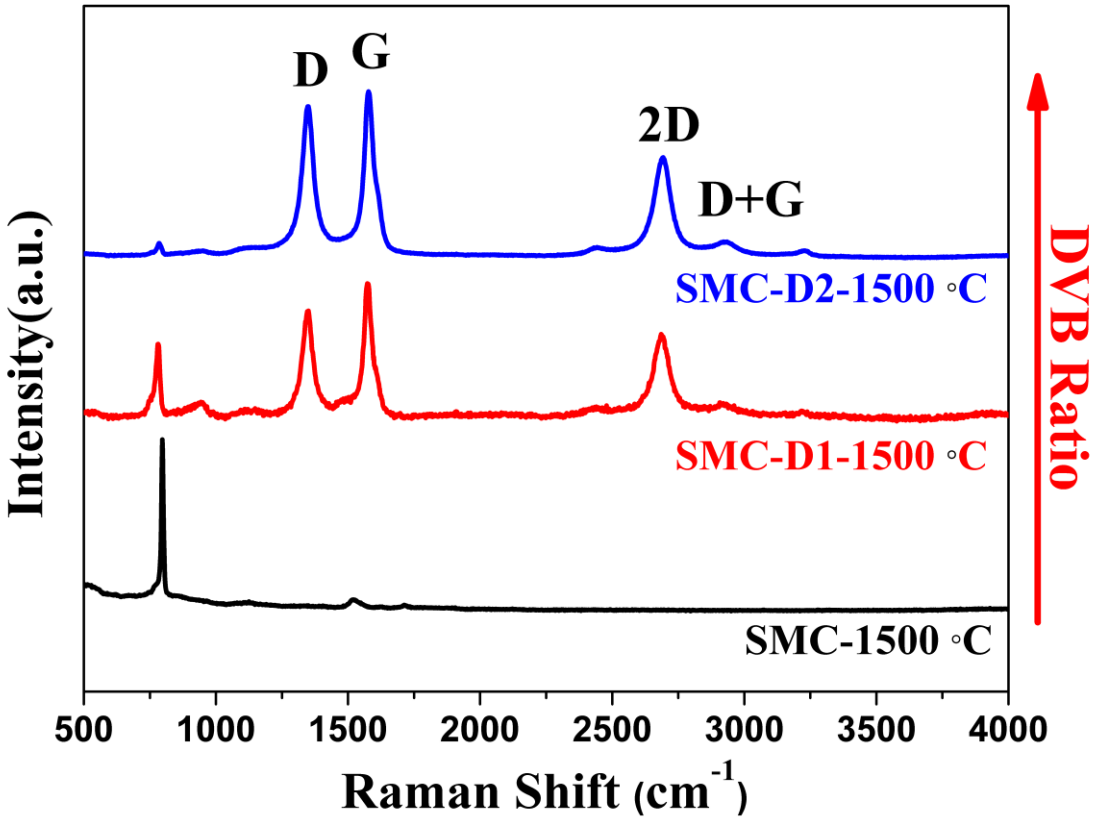

Figure 3. 20 Raman spectra of the synthesized ceramics prepared without and with different DVB contents in the feed.

3.3.2.2 Raman spectra

Raman spectra of the ceramic samples prepared with different DVB in the feed (i.e., SMC-1500 ºC, SMC-D1-1500 ºC and SMC-D2-1500 ºC) are shown in **Figure 3. 20**. In the Raman spectra of sample SMC-1500ºC, no signals for D (1350 cm^{-1}) and G (1580 cm^{-1}) bands can be detected, indicating the low C_{free} content, which is consistent with the phase composition presented in **Table 3. 2**. While, the high intensity of D (1350 cm-1), G (1580 cm^{-1}) and 2D (2700 cm^{-1}) bands in the Raman spectra of SMC-D1-1500 ºC and SMC-D2-1500 ºC clearly reveal the existence of C_{free} in both samples [218]. Moreover, in the spectra of all three samples, a band of 796 cm^{-1} can be assigned to the transverse optical (TO) phonon mode of β-SiC [249]. From the Raman spectra of the samples SMC-1500 ºC, SMC-D1-1500 ºC and SMC-D2-1500 ºC, it can be found that the relative intensity of the TO band for SiC decreases gradually, indicating the improved C_{free} content with increasing DVB in feed.

3.3.2.3 TEM characterization

The phase transformation between $Mo_{4.8}Si_3C_{0.6}$ and $MoSi_2$ affected by C_{free} can be further supported by TEM studies. The TEM images of the sample SMC-1500 ºC are shown in **Figure 3. 21** (a, b), confirming

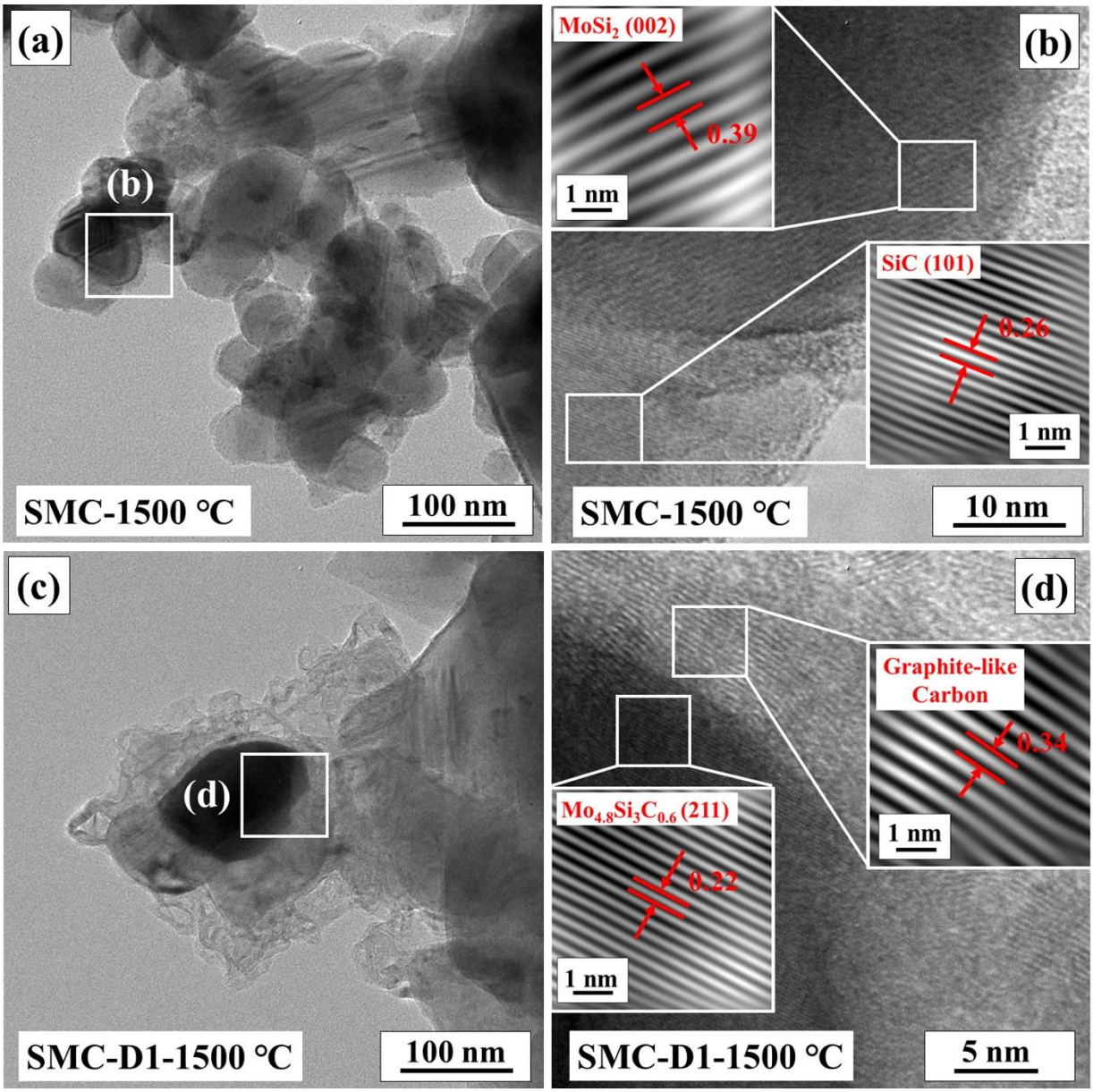

Figure 3. 21 TEM images showing (a) and (b) the microstructure of SMC-1500ºC and (c) and (d) that of SMC-D1-1500ºC. (b) and (d) are high resolution TEM images taken from the white rectangular in (a) and (c), respectively.

the formation of nanocomposites with $MoSi_2$ nanoparticles (dark contrast and the grain size < 100 nm) homogeneously embedded within the SiC-based matrix. However, C_{free} can be rarely found in this sample. In comparison, in the TEM images of the sample SMC-D1-1500 ºC [**Figure 3. 21** (c, d)], the Nowotny phase ($Mo_{4.8}Si_3C_{0.6}$) and C_{free} can be clearly detected. This is because the addition of DVB in the preceramic polymer enhanced the C_{free} content in the resultant ceramics, which ensured the formation of the $Mo_{4.8}Si_3C_{0.6}$ phase. The existence of the graphite-like carbon found within the sample SMC-D1-1500 ºC ceramic, is consistent with the Raman spectra shown in **Figure 3. 20**. In addition, the TEM images prove that the average grain size of the $Mo_{4.8}Si_3C_{0.6}$ is less than 100 nm, which is in accordance with the XRD

refinement (**Table 3. S4**). The XRD and TEM results suggest that 1500 °C is a crucial annealing temperature where the phase evolution between $Mo_{4.8}Si_3C_{0.6}$ and $MoSi_2$ can be tailored by the amount of C_{free}. Consequently, 1500 °C is adopted as the annealing temperature for the further investigation of EMW absorption properties of the Mo-containing ceramics.

3.3.2.4 Dielectric properties of the synthesized ceramics

To investigate the EMW absorption properties of the produced Mo-containing ceramics, the complex permittivity ($\varepsilon_r = \varepsilon' - j\varepsilon''$) and permeability ($\mu_r = \mu' - j\mu''$) of the paraffin-ceramic samples are measured by a VNA. The values of complex permeability (μ_r) are rather low and almost constant (see **Figure 3. S10**), indicating that only dielectric properties of the materials should be considered. Thus, their EMW absorption properties are dominated by the complex permittivity (ε_r). The complex permittivity (ε_r) of the Mo-containing ceramics in the 2-18 GHz are depicted in **Figure 3. 22**. The real part (ε') and imaginary part (ε'') of the permittivity reveals the polarization capacity and dielectric loss ability of the absorber material, respectively [48]. As shown in **Figure 3. 22** (a), the molybdenum-free sample derived from pure SMP-10 (i.e. SC-1500 ºC) shows the lowest average ε' around 6.47, while the ε' values of the Mo-containing ceramics are in the range between 5.7 and 19.2. Generally, the ε′ value of β-SiC with monocrystalline structure is around 10 [250]. The Maxwell Garnett rule [251] can be used to estimate the ε′ of a monocrystalline β-SiC/paraffin wax mixture (4:6), and the ε′ value is less than 4 [54]. Compared with this reference, all the 1500 ºC ceramics exhibit enhanced ε'-values [**Figure 3. 22** (a)], which could be explained by the interfacial polarization of the β-SiC matrix with polycrystalline structure and the existence of the graphite- like carbon with higher ε' (in the order of 10^2) [252].

The ε″ values of samples annealed at 1500 ºC are presented in **Figure 3. 22** (b). In case of composites with conductive fillers (such as carbon or other high conducting components), the electronic transport could be

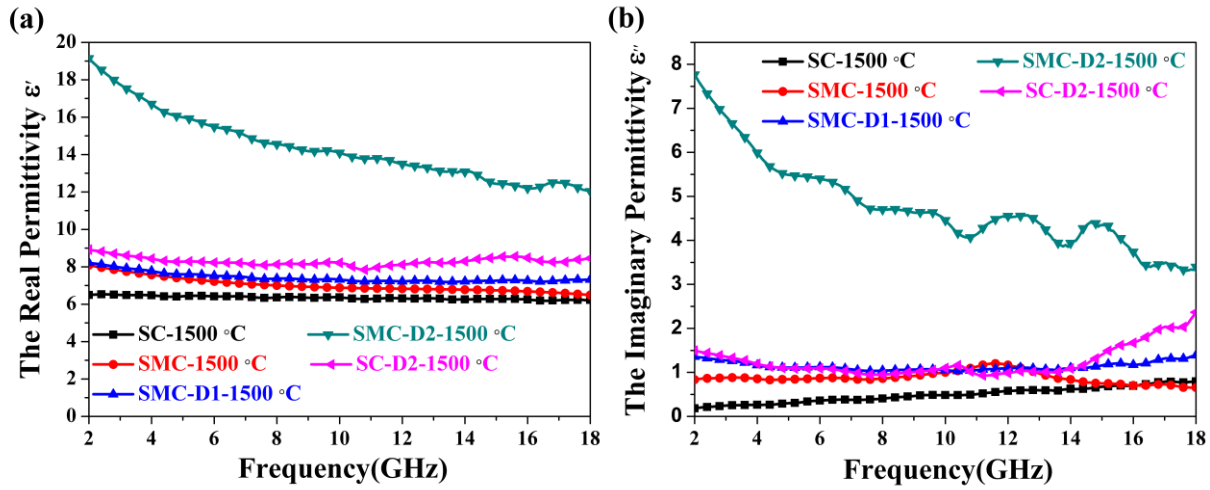

Figure 3. 22 Frequency-dependent the real part (a) and imaginary part (b) of the permittivity of the Mo-containing ceramics (SMC) and SMP-10 derived SiC annealed at 1500 °C (SC-1500 ºC).

approximated by the free electron theory. Therefore, based on the Debye theory, ε'' can be expressed briefly by the equation [149, 154] as follows:

$$\varepsilon'' \approx \frac{\sigma}{2\pi f \varepsilon_0} \qquad \textbf{Eq. (3.2)}$$

where, σ and f are the electrical conductivity of the dielectric material and the frequency of the incident EMW, respectively. ε_0 is the permittivity of free space, and it has a constant value (8.85×10^{-12} F/m). According to **Eq. (3.2)**, the enhanced electric conductivity of the composites can lead to the increase of ε″. **Figure 3. 22** (b) shows that the ε'' values of the sample SMC-1500 ºC (≈1.07) is higher than that of SC-1500 ºC (≈ 0.47), despite that the free carbon content is rather low in SMC-1500 ºC. This behavior is explained by the contribution of in-situ formed conductive $MoSi_2$ nanoparticles dispersed within the matrix of sample SMC-1500 ºC. Increasing C_{free} content accelerates the generation of more conductive $Mo_{4.8}Si_3C_{0.6}$ phase and forms a percolating conductive network. Therefore, the samples SMC-D1-1500 ºC and SMC-D2-1500 ºC exhibit even higher ε'' values (3.41-7.84). Compared with sample SC-D2-1500 ºC (average ε'' ≈ 1.5) prepared using the same amount of DVB, the value of the sample of SMC-D2-1500 ºC with an average $\varepsilon''\approx$ 5.6 is more than 2 times higher, indicating the important role of the in situ formed $Mo_{4.8}Si_3C_{0.6}$ nanoparticles in the enhanced imaginary permittivity of the SMC ceramics. The discussion of the imaginary

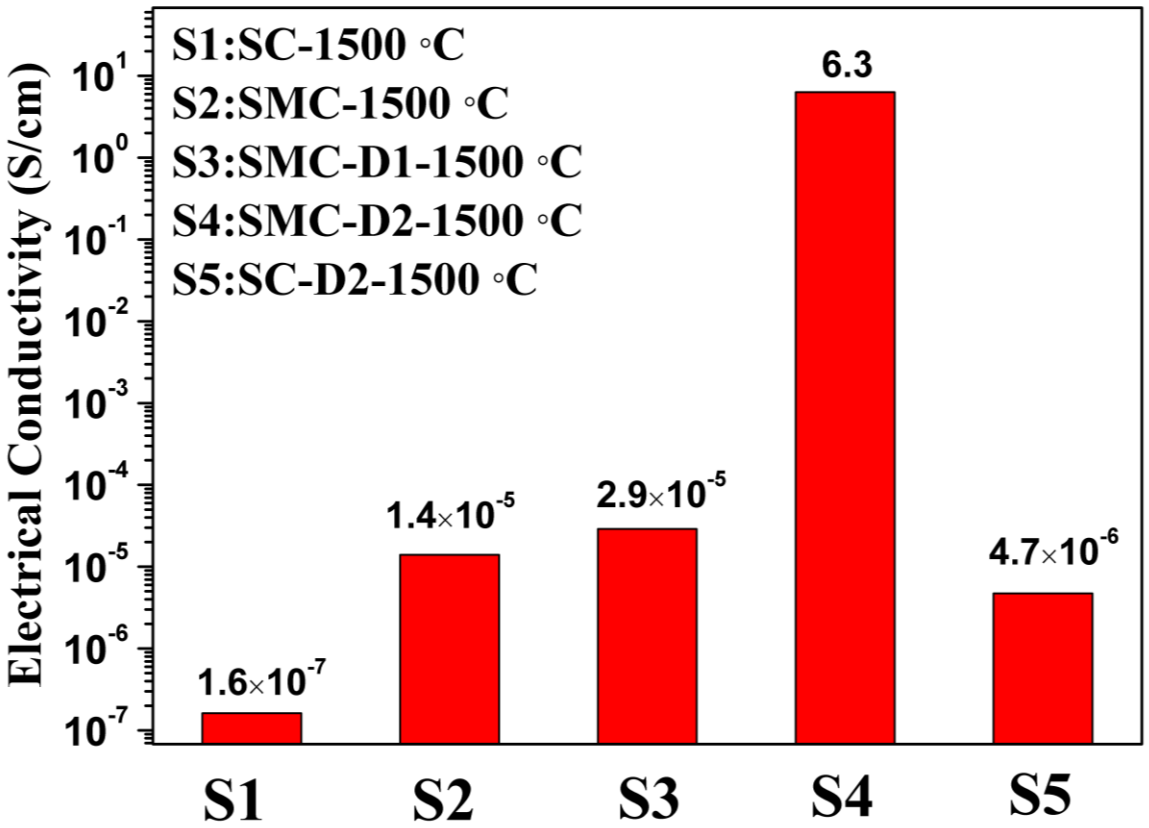

Figure 3. 23 Electrical conductivity of the ceramics annealed at 1500 °C and mixed with paraffin wax.

part ε'' is supported by the results of the DC electrical conductivity shown in **Figure 3. 23**. The DC electrical conductivity values were measured from the ceramic/paraffin wax mixtures with the 4:6 ratio. The DC electrical conductivity of the sample SMC-1500 ºC is much higher than that of the Mo-free SC-1500 ºC mixture due to the in situ formed conductive $MoSi_2$ nanoparticle ($\sigma \approx 2 \times 10^5$ S/cm at room temperature) [253]. As aforementioned, when DVB was added as the carbon source to increase the C_{free} content, the $MoSi_2$ phase converted into the $Mo_{4.8}Si_3C_{0.6}$ phase, leading to a jump of the electrical conductivity from 1.4×10^{-5} S/cm (SMC-1500 ºC) to 6 S/cm (SMC-D2-1500 ºC). The significantly increased electrical conductivity is attributed to two reasons. One is the phase transformation between $MoSi_2$ and $Mo_{4.8}Si_3C_{0.6}$. However, it is not clear whether the $Mo_{4.8}Si_3C_{0.6}$ exhibits higher DC electrical conductivity than that of the $MoSi_2$ or not. Comparing the electrical conductivity of SMC-D2-1500 ºC and SC-D2-1500 ºC, the presence of $Mo_{4.8}Si_3C_{0.6}$ strongly improves the electrical conductivity of the Mo-containing material. The second reason is the formation of a percolating network due to the enhanced free carbon content, which is considered to be more reasonable to explain the strong rise of the electrical conductivity [232].

Besides, the ε' and ε'' values of the samples annealed at 1300, 1400 and 1600 ℃ were also measured (**Figure 3. S11**). Compared with the above-discussed samples (SMC-1500 ℃, SMC-D1-1500 ℃ and SMC-D2-1500 ℃), the ε' and ε'' of the other samples are much lower and close to each other. Normally, the increasing graphitization/structural ordering of C_{free} in polymer-derived ceramics with the annealing temperature leads to an increase of the real and imaginary part of the permittivity [54]. However, in this study, the annealing temperature caused a serial of complicated and multiple influence on the microstructural evolution of the nanocomposites, such as the decrease of C_{free}, phase transformation of $Mo_{4.8}Si_3C_{0.6}$ into $MoSi_2$ (if no more C_{free} is present) as well as the improved degree of crystallization of $Mo_{4.8}Si_3C_{0.6}$, $MoSi_2$ and SiC, which can affect the dielectric properties in different ways. Therefore, the influence of annealing temperature on the dielectric properties of the Mo-containing ceramics cannot be discussed here.

The loss tangent values ($\tan\delta = \varepsilon''/\varepsilon'$) can be used to evaluate the dielectric loss of materials in the associated frequency range. In general, a higher tan δ value implies higher attenuation ability, when the EMA materials are under the impedance-matching condition. Thus, **Figure 3. 24** (a) presents the tan δ of samples calculated by using the measured values of ε'' and ε'. The tan δ of all samples show a similar trend with the results of ε'' discussed above. The SMC-D2-1500 ºC sample exhibits the highest value of $\tan\delta \approx 0.35$, which is about two and three times higher than that of sample SC-1500 ºC (tan δ below 0.17), indicating that the formed $Mo_{4.8}Si_3C_{0.6}$/SiC/C_{free} nanocomposites have a superior dielectric loss. Despite the increased carbon content via addition of DVB, the tan δ of the SC-D2-1500 ºC ($\tan\delta \approx 0.24$) without the Nowotny phase $Mo_{4.8}Si_3C_{0.6}$ is still lower than that of the sample SMC-D2-1500 ºC. In summary, as shown in **Figure 3. 24** (b), the EMW absorption mechanisms can be mainly ascribed to two factors: 1) interfacial polarization 2) ohmic loss, due to the unique microstructure of our $Mo_{4.8}Si_3C_{0.6}$/SiC/C_{free} nanocomposites comprised of the conducting $Mo_{4.8}Si_3C_{0.6}$ nanoparticles and graphite-like carbon. Moreover, because the wavelength of the incident EM wave is much greater than the particle dimension of the $Mo_{4.8}Si_3C_{0.6}$ nanocrystallites and free carbon (in

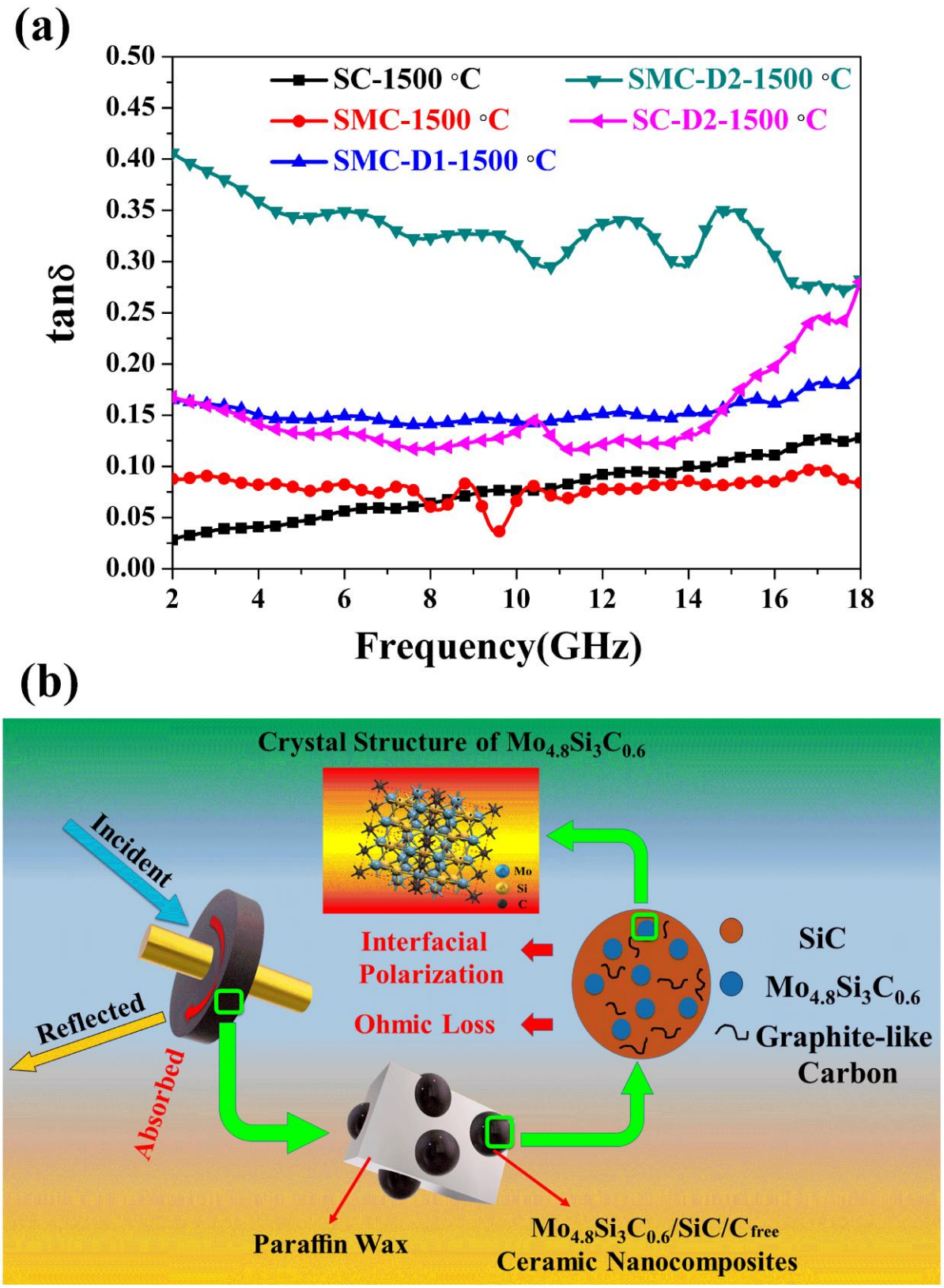

Figure 3. 24 Loss tangent (a) of the Mo-containing ceramics (SMC) and SMP-10 derived SiC annealed at 1500 °C (SC-1500 ºC) and schematic EMW absorption mechanism (b) of the $Mo_{4.8}Si_3C_{0.6}/SiC/C_{free}$ ceramic nanocomposites.

this scenario cm with respect to nm of materials), the interactions of EM wave with the nano-sized conductive particles could be ignored [254]. Therefore, the multiple reflection loss are not considered as the absorption mechanism for the $Mo_{4.8}Si_3C_{0.6}/SiC/C_{free}$ ceramic nanocomposites.

3.3.2.5 Electromagnetic wave absorption

The EMW absorbing performance can be described by the reflection loss (RL) calculated from ε_r and μ_r values based on a metal back-panel model [255-257].

$$RL = \log_{10}|(Z_{in} - Z_0)/(Z_{in} - Z_0)| \quad \textbf{Eq. (3.3)}$$

$$Z_0 = (\mu_0/\varepsilon_0)^{1/2} \quad \textbf{Eq. (3.4)}$$

$$Z_{in} = Z_0(\mu_r/\varepsilon_r)^{1/2} tanh[j(2\pi fd/c)(\mu_r/\varepsilon_r)^{1/2}] \quad \textbf{Eq. (3.5)}$$

where Z_{in} is the input impedance at the air-absorber interface, Z_0 is the intrinsic impedance of free space, f

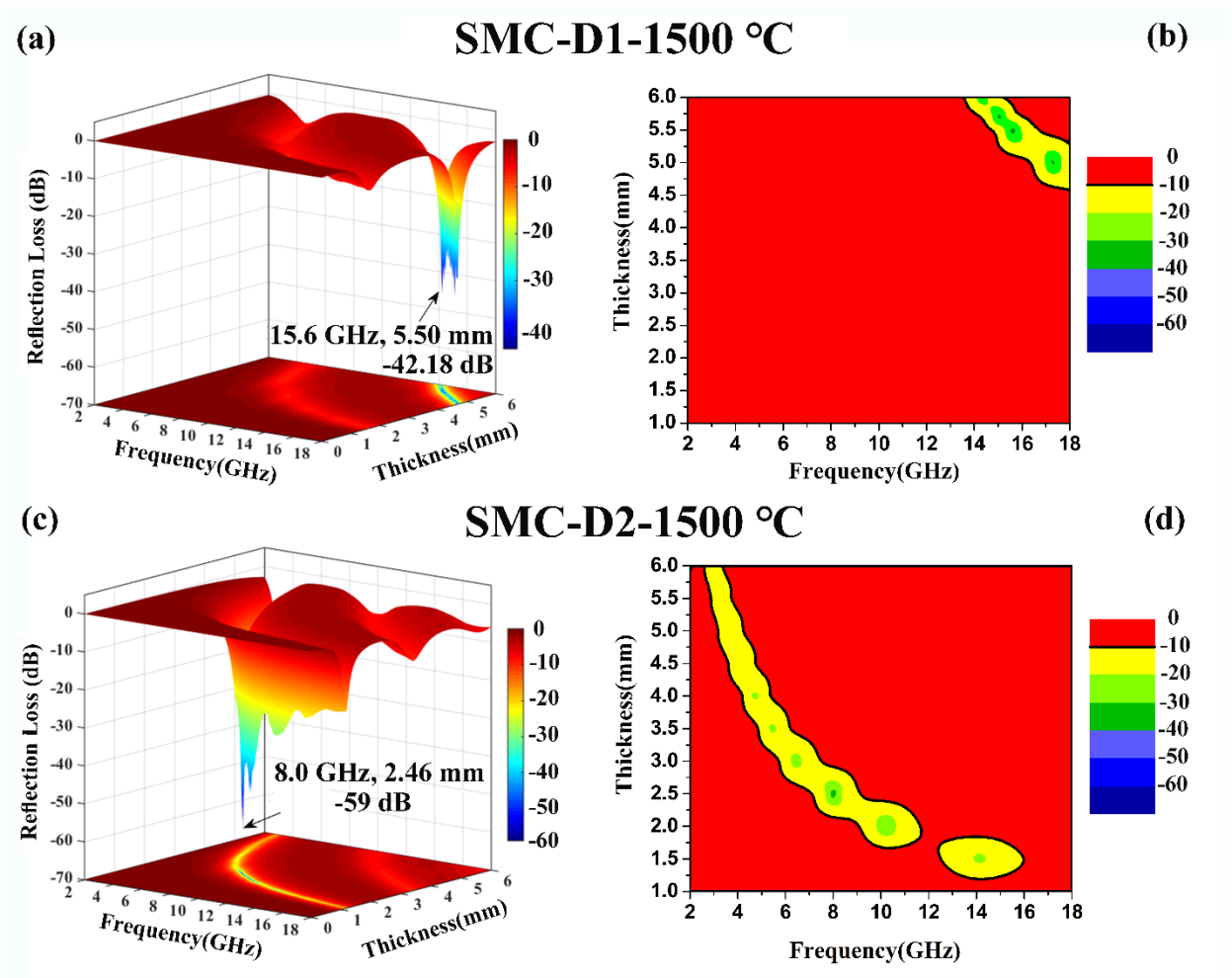

Figure 3. 25 Simulated three-dimensional RL patterns (a, c) and contour maps (b, d) of absolute values of the bandwidth (<−10 dB) of $Mo_{4.8}Si_3C_{0.6}/SiC/C_{free}$ ceramic nanocomposites.

is the frequency of the incident EMW, *c* is the velocity of light in free space, and d is the thickness of the absorber. In addition, the effective absorption bandwidth (EAB) can be defined as the corresponding frequency range of RL < -10 dB, which means more than 90 % of the EMA energy is absorbed while less than 10% of the energy is reflected. **Figure 3. 25** and **Figure 3. S12** present the RL calculated by using **Eq (3.3-3.5)**. As shown in **Figure 3. S12**, the effective EMW absorption ability (RL <-10 dB) of SC-1500 ºC and SMC-1500 ºC is poor, whereas a significant improvement of the RL values is observed for the sample SMC-D1-1500 ºC [**Figure 3. 25** (a)] due to the increasing content of the C_{free} and the formation of $Mo_{4.8}Si_3C_{0.6}$. Specifically, the minimum RL (RL_{min}) of SMC-D1-1500 ºC with a 5.5 mm thickness is - 42.18 dB at 15.6 GHz. The EAB (RL < -10 dB) amounts to 3 GHz when the absorber thickness is 5.3 mm. This RL is further optimized in the sample SMC-D2-1500 ºC with more free carbon [**Figure 3. 25** (c)], where the RL_{min} value further decreases to -59 dB at 8 GHz with 2.46 mm absorber thickness. The sample SMC-D2-1500 ºC is able to cover a broad EAB = 12.55 GHz (2.53-11.64 GHz and 12.56-16 GHz) through tuning the thickness between 1 and 6 mm [**Figure 3. 25** (d)]. Moreover, with 1.5 mm thickness, the EAB is significantly increased by about 3.44 GHz (12.56-16 GHz). In addition, sample SC-D2-1500 ºC without Mo also shows EMW absorbing capability [**Figure 3. S12** (c)], but its RL_{min} value is still much lower than that of the $Mo_{4.8}Si_3C_{0.6}/SiC/C_{free}$ nanocomposites discussed above. Compared to other reported SiC-based materials (**Figure 3. 26**), the $Mo_{4.8}Si_3C_{0.6}/SiC/C_{free}$ ceramic nanocomposites exhibit superior EM absorbing

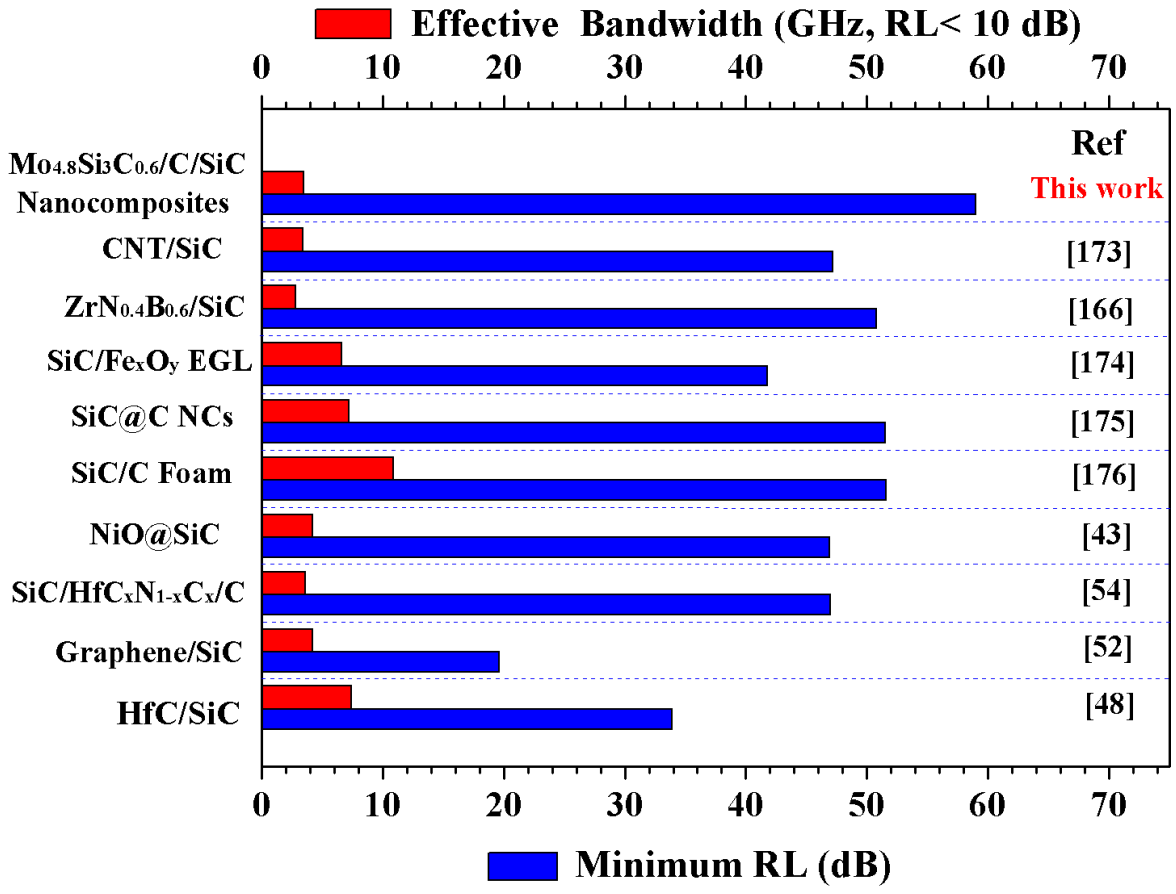

Figure 3. 26 Comparison of the RLmin and EAB with representative SiC-based related composites.

performance (RL = -59 dB) at a rather thin thickness (2.46 mm). Moreover, the EAB of $Mo_{4.8}Si_3C_{0.6}$/SiC/C_{free} nanocomposites is not broad enough, while it is still in the range of other reported materials (**Figure 3. 26**) [43, 48, 52, 54, 166, 173-176]. Therefore, increasing the effective bandwidth could be considered as a target in our future research on optimizing the EM absorbing performance of $Mo_{4.8}Si_3C_{0.6}$/SiC/C_{free} nanocomposites.

3.3.3 Conclusions

In this work, $Mo_{4.8}Si_3C_{0.6}$/SiC-based ceramic nanocomposites with the Nowotny phase ($Mo_{4.8}Si_3C_{0.6}$) embedded in a β-SiC matrix were successfully synthesized by a single-source-precursor approach. We demonstrated that the phase transformation between $Mo_{4.8}Si_3C_{0.6}$ and $MoSi_2$ is strongly controlled by the C_{free} content. Specifically, lack of C_{free}, the $Mo_{4.8}Si_3C_{0.6}$ phase decomposes into $MoSi_2$ during annealing at elevated temperatures, while in the presence of excess C_{free}, the Nowotny phase is stabilized. Therefore, the phase composition of the SiC/ $Mo_{4.8}Si_3C_{0.6}$-based ceramic nanocomposites can be easily tuned via adjusting the amount of DVB during the single-source-precursor synthesis process. Compared to $MoSi_2$/SiC nanocomposites (sample SMC-1500 ºC), the as-prepared Nowotny-phase-containing $Mo_{4.8}Si_3C_{0.6}$/SiC/C nanocomposites (samples SMC-D1-1500 ºC and SMC-D2-1500 ºC) exhibit an enhanced EM absorbing performance due to improved dielectric loss. In conclusion, this study provides a controllable and promising strategy to develop SiC-based nanocomposites with the presence of a Nowotny phase. The outstanding EM absorbing performance of the $Mo_{4.8}Si_3C_{0.6}$/SiC/C_{free} nanocomposites paves a new road in two different directions, namely i) for electrocatalysis in the field of electrochemical hydrogen evolution reaction and ii) for advanced EM absorbing materials suitable for application in hostile environments.

3.3.4 Supporting information

The weight fractions and average grain size (**Table 3. S4**) of crystallized $Mo_{4.8}Si_3C_{0.6}$, $MoSi_2$ and SiC phases are determined by Rietveld refinement of the XRD patterns of the ceramics with the FullProf software [257]. The peak shapes are modeled using Thompson-Cox-Hastings pseudo-Voigt function for average grain size and pseudo-Voigt function for weight fraction [258]. The Rietveld refinement results are shown in **Figure 3. S9**.

Table 3. S4 Average grain size of Mo-containing ceramics by Rietveld refinement of the XRD patterns.

Sample	SiC	$MoSi_2$	$Mo_{4.8}Si_3C_{0.6}$
SMC-1500ºC	31.07 nm	36.45 nm	/
SMC-D1-1500ºC	28.44 nm	/	42.89 nm
SMC-D2-1500ºC	27.25 nm	/	48.97 nm

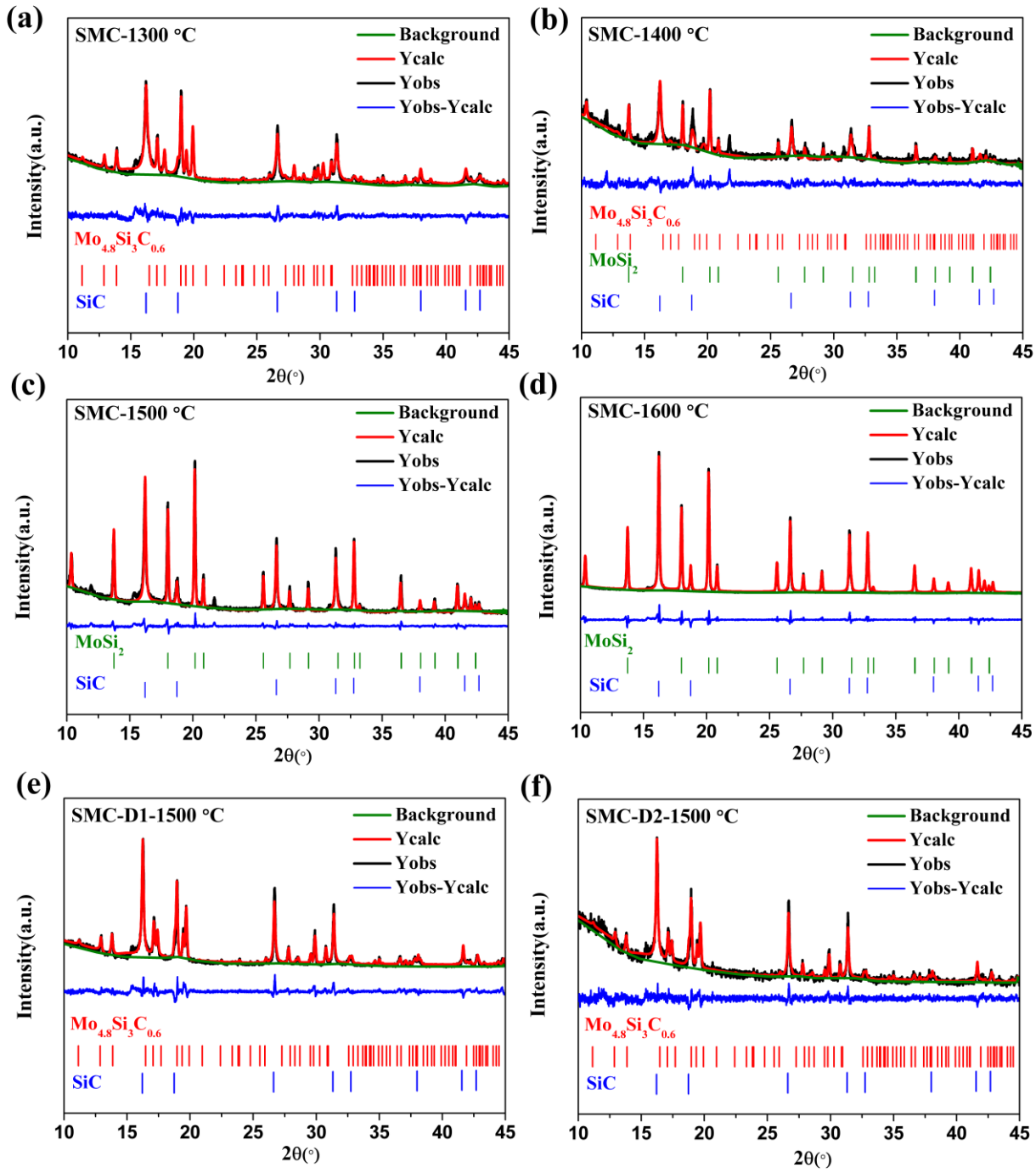

Figure 3. S9 Diffraction pattern of the Mo-containing ceramic samples annealed at different temperatures (a-d) and with different DVB contents in the feed (e, f) with the result of Rietveld refinement. Y_{obs} and Y_{calc} represent the observed and calculated profiles respectively; the green line represents the background; the blue line (Y_{obs}-Y_{calc}) at the bottom denotes the intensity difference between the observed and calculated profiles.

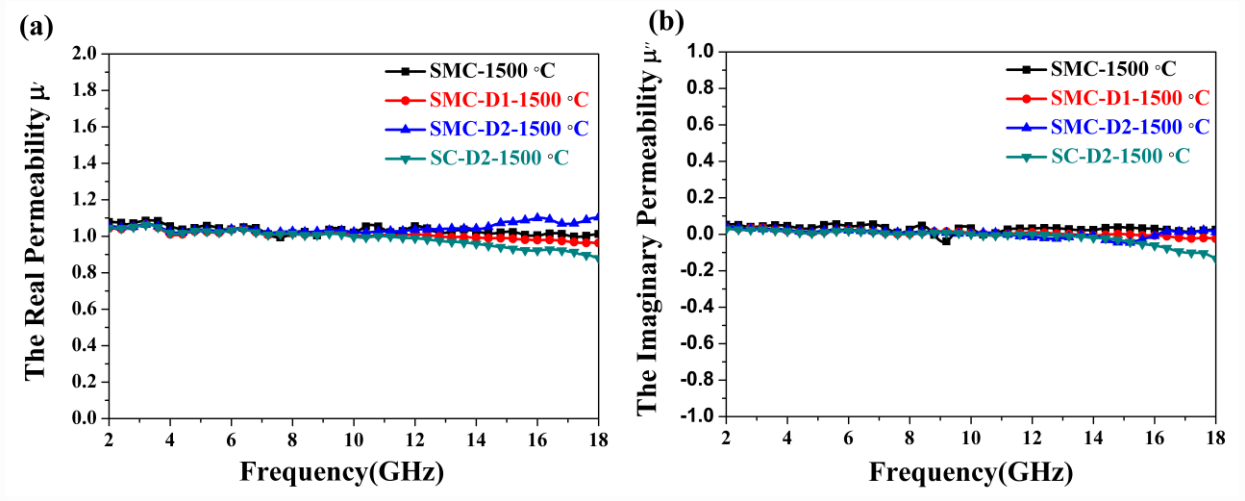

Figure 3. S10 Frequency dependent (a, b) complex permeability ($\mu_r = \mu' - j\mu''$) of the Mo-containing ceramics annealed at 1500 °C.

Normally, the increasing graphitization/structural ordering of free carbon in polymer-derived ceramics with the annealing temperature leads to an increase of the imaginary part ε'' [38]. However, in our study, the annealing temperature caused a serial of complicated influence on the microstructural evolution of the nanocomposites, such as the decrease of free carbon, phase transformation of $Mo_{4.8}Si_3C_{0.6}$ into $MoSi_2$ (if no more free carbon is present) as well as the improved degree of crystallization of $Mo_{4.8}Si_3C_{0.6}$, $MoSi_2$ and SiC, which can affect the dielectric properties in different ways. Moreover, we measured all dielectric properties of the SMC samples without DVB (please see **Figure 3. S11**). The results indicate that the real part (ε') and imaginary part (ε'') of the permittivity of the samples annealed at different temperatures (SMC-1300 ℃, SMC-1400 ℃ and SMC-1600 ℃) are much lower than that of samples (SMC-1500 ℃, SMC-D1-1500 ℃ and SMC-D2-1500 ℃) which we discussed in our manuscript, and the curves are very close to each other. It is too complex to clarify the effect of the annealing temperature on the dielectric properties

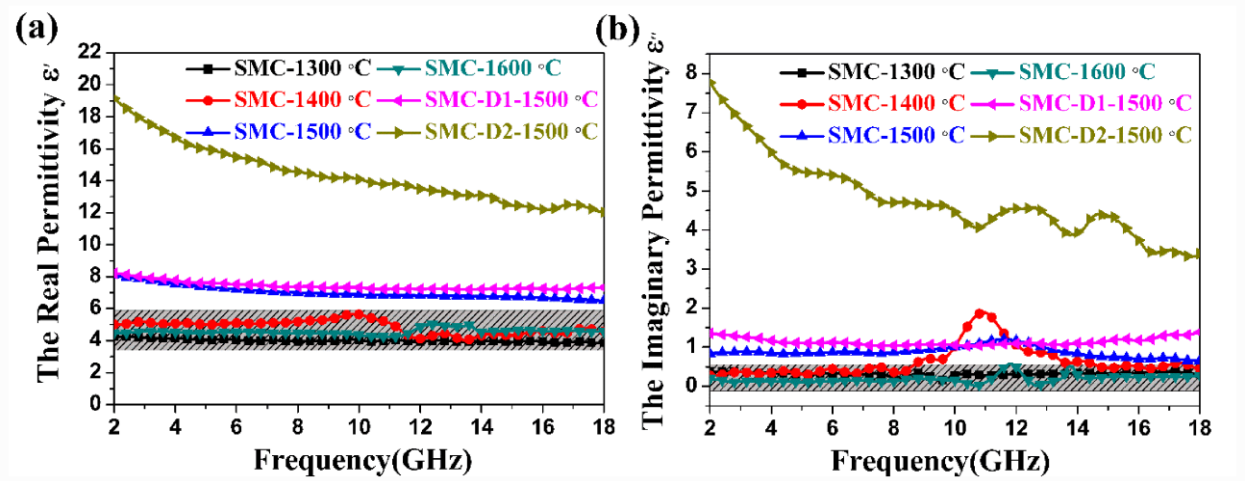

Figure 3. S11 Frequency-dependent (a, b) complex permittivity ($\varepsilon_r = \varepsilon' - j\varepsilon''$) of the Mo-containing ceramics annealed at different temperatures.

of our samples. This would require a separate study. Therefore, the influence of the annealing temperature on the dielectric properties has not been discussed in this study.

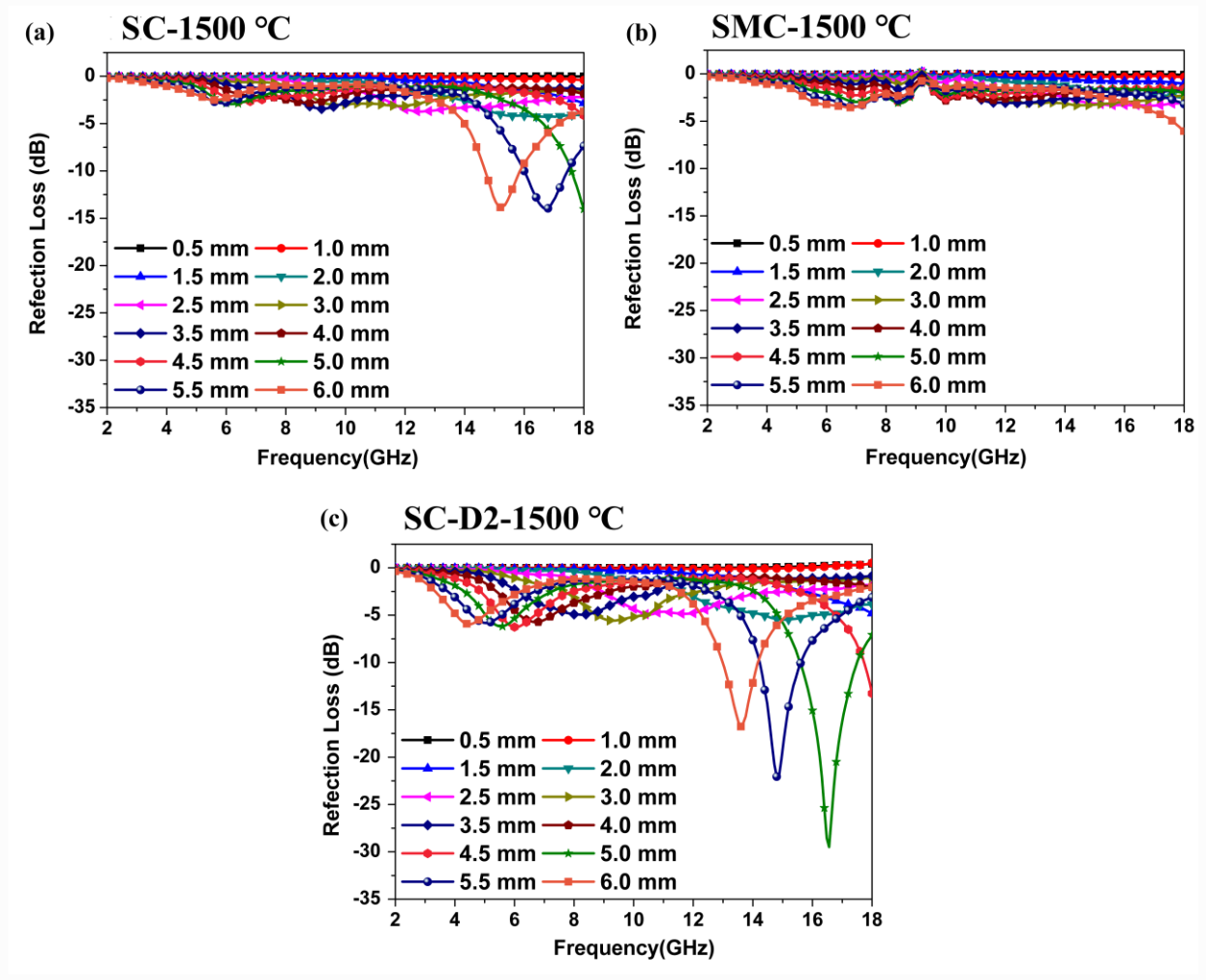

Figure 3. S12 Reflection loss at RT of the SC-1500 °C (a), SMC-1500 °C (b) and SC-D2-1500 °C (c) samples with respect to thickness variation.

4 Conclusion and outlook

4.1 Conclusion

The Nowotny phase ($Mo_{4.8}Si_3C_{0.6}$) embedded in a porous SiC/C nanocomposite matrix is synthesized via a single-source-precursor approach which involves the reaction of allylhydridopolycarbosilane with $MoO_2(acac)_2$. Thermal treatment of the single-source-precursor up to 1400~1600 °C in a protective atmosphere results in the in-situ formation of nanocrystalline $Mo_{4.8}Si_3C_{0.6}$ immobilized in a thermally and corrosion resistant SiC/C matrix. High-temperature phase evolution of the nanocomposites reveals that free carbon (C_{free}) plays a crucial role in the in-situ formation of the Nowotny phase, indicating that the microstructure of the nanocomposites can be tailored via molecular design of the single-source precursors. For the first time, the NP is discovered i) to possess excellent electrocatalytic activity and durability in terms of the HER in the field of water splitting and ii) outstanding dielectric properties and electromagnetic wave (EMW) absorbing performance for application in telecommunication field.

The first part (Chapter 3.1) of this work is focused on the synthesis, characterization and electrocatalytic activity of $Mo_{3+2x}Si_3C_{0.6}$/C/SiC nanocomposites. The obtained η_1 and η_{10} values of sample SM/Mo/PS 2-1-4 1400 amount to 22 and 138 mV in acidic media, respectively, which are superior to most of all previously reported molybdenum-based electrocatalysts. The sample also retains over 90 % of its original electrochemical activity after operating of the electrode for 35 h, demonstrating a robust and stable electrocatalytic performance of the material under acidic conditions. Moreover, the material also shows excellent corrosion stability in acidic media. The analyzed exceptional electrocatalytic performance is based on i) catalytically active nanocrystalline ternary MoSiC Nowotny phase, dispersed and immobilized in a SiC-based ceramic matrix; ii) the presence of carbon improving the overall electrical conductivity of the nanocomposites; iii) the highly porous network originated from the addition of PS as pore former enabling the efficient access of active sites of the MoSiC electrocatalyst.

In the scorned part (Chapter 3.2) of this work, to further improve the HER activity of the $Mo_{4.8}Si_3C_{0.6}$/C/SiC ceramic nanocomposites, DVB was used as a carbon source to synthesize mesoporous $Mo_{4.8}Si_3C_{0.6}$/C/SiC ceramic nanocomposites with high total carbon content (above 50 wt %) and high free carbon content (36 wt%). When annealed at high temperatures (1350-1600 °C), the carbon-rich $Mo_{4.8}Si_3C_{0.6}$/C/SiC ceramic nanocomposites still retain a high BET surface area in the range of 214.6-304 m^2/g due to the carbothermal reaction, leading to an excellent HER performance. The carbon-rich samples synthesized at 1500°C, denoted as SM/Mo/PS/DVB 2-1-4-2 1500 exhibit enhanced electrocatalytic performance with ultra-low overpotentials of 119 mV vs. reversible hydrogen electrode at a current density of 10 mA cm^{-2} in acidic media, which is superior to that of the $Mo_{4.8}Si_3C_{0.6}$/C/SiC ceramic (138 mV) with lower carbon content reported in the first part of this work.

The third part (Chapter 3.3) of this thesis is concerned with the dielectric properties and electromagnetic wave (EMW) absorbing performance of single-source-precursor derived $Mo_{4.8}Si_3C_{0.6}$/SiC/C_{free} ceramic

nanocomposites. The chemical/phase composition as well as the microstructural evolution of the $Mo_{4.8}Si_3C_{0.6}$/SiC-based nanocomposites annealed at 1100 - 1600 °C were studied in detail, which reveals that the phase transformation between $Mo_{4.8}Si_3C_{0.6}$ and $MoSi_2$ is strongly controlled by the C_{free} content. Specifically, lack of C_{free} results in the decomposition of the $Mo_{4.8}Si_3C_{0.6}$ phase to form $MoSi_2$ during annealing, while in the presence of excess C_{free}, the Nowotny phase is stabilized. Therefore, the phase composition of the SiC/$Mo_{4.8}Si_3C_{0.6}$-based ceramic nanocomposites can be easily tuned via adjusting the amount of DVB during the single-source-precursor synthesis process. Compared with SiC/C_{free} and $MoSi_2$/SiC/C_{free} nanocomposites obtained under the same conditions, the $Mo_{4.8}Si_3C_{0.6}$/SiC/C_{free} nanocomposites exhibit significantly enhanced EMW absorbing performance. A minimum reflection loss (RL) of -59 dB was achieved at 8 GHz for the thickness of 2.46 mm, proving the superiority of the $Mo_{4.8}Si_3C_{0.6}$/SiC/C_{free} nanocomposite as an outstanding EMW absorbing material.

In summary, the present results impressively reveal that porous $Mo_{4.8}Si_3C_{0.6}$/SiC/C ceramic nanocomposites with in-situ formed $Mo_{4.8}Si_3C_{0.6}$ nanoparticles embedded in a β-SiC matrix have to be considered as novel multifunctional materials. In the frame of the present studies, the NP-based nanocomposites have been discovered to show excellent performance in two different fields including electrochemical water splitting and EMW absorption.

4.2 Outlook

The Nowotny phase embedded in a porous SiC/C nanocomposite matrix was synthesized via a single-source-precursor approach. Then, in order to improve the conductivity of the SiC-bases matrix, mesoporous carbon-rich NP/C/SiC ceramic nanocomposites with high free carbon content (36 wt%) have been synthesized via the addition of DVB as additional carbon source. However, the poor electrical conductivity of SiC as catalyst supports still limited the electrocatalytic activity of the Nowotny phase. Therefore, the challenge is whether we can synthesize pure $Mo_{4.8}Si_3C_{0.6}$ nanoparticles or generate $Mo_{4.8}Si_3C_{0.6}$ nanoparticles on the surface of some catalyst supports with high electrical conductivity (such as carbon or CNT). One possible way is the ammonolysis of transition-metal hexamethyldisilylamides $M(N(SiMe_3)_2)_n$, where M is Mo or W [259]. The initially formed products are hydrocarbon-insoluble powders which are commonly used as molecular precursors for the formation of pure transition metal alloys after thermal decomposition. Thus, the ammonolysis of transition-metal hexamethyldisilylamides should be applied on the synthesis of pure $Mo_{4.8}Si_3C_{0.6}$ nanoparticles in following studies. Besides, some catalyst supports with high surface area and high electrical conductivity can be introduced during the ammonolysis to avoid aggregation and densification of $Mo_{4.8}Si_3C_{0.6}$ nanoparticles. The molecular route for the synthesis of NP has been proved to be a promising way to boost the electrocatalytic activity of NP-containing HER catalysts.

Some evidences were found to indicate the possible presence of other Nowotny-type phases containing e.g. W (like $W_{4.8}Si_3C_{0.6}$). Gnesin and co-works attempted the reactions of W_5Si_3 or W_5Si_3 + WSi_2 eutectic powder mixtures with carbon to form a W-derivative of the NP via solid state reactions and melt-quenching methods [205]. Thus, it could be an interesting topic whether the SiC/C nanocomposite matrix with the W-containing Nowotny phase can be synthesized via a single-source-precursor approach. Additionally, potential applications of W-containing Nowotny phases should be explored as inorganic W-compounds have been already reported to exhibit excellent functional properties.

Although the Nowotny phase was identified long time ago, possible applications of this phase are still limited. In this Ph.D. work, for the first time, we prepared NP-containing ceramic nanocomposites via a single-source-precursor approach and explored two functional applications of NP. Based on this work, other potential applications of NP-containing materials should be further investigated.

5 Reference

[1] X. Zou; Y. Zhang, *Chemical Society Reviews* **2015,** 44 (15), 5148-5180.

[2] T. Hayashi; K. Ito; K. Tanaka, *Intermetallics* **2003,** 11 (8), 835-840.

[3] F. Qin; C. Brosseau, *Journal of Applied Physics* **2012,** 111 (6), 4.

[4] E. Ionescu; H. J. Kleebe; R. Riedel, *Chemical Society Reviews* **2012,** 41 (15), 5032-5052.

[5] J. K. Nørskov; T. Bligaard; A. Logadottir; J. Kitchin; J. G. Chen; S. Pandelov; U. Stimming, *Journal of The Electrochemical Society* **2005,** 152 (3), J23-J26.

[6] J. O. M. Bockris, *International journal of Hydrogen Energy* **2002,** 27 (7-8), 731-740.

[7] J. Ran; J. Zhang; J. Yu; M. Jaroniec; S. Z. Qiao, *Chemical Society Reviews* **2014,** 43 (22), 7787-7812.

[8] N. Armaroli; V. Balzani, *Angewandte Chemie International Edition* **2007,** 46 (1-2), 52-66.

[9] A. J. Esswein; D. G. Nocera, *Chemical Reviews* **2007,** 107 (10), 4022-4047.

[10] P. Du; R. Eisenberg, *Energy & Environmental Science* **2012,** 5 (3), 6012-6021.

[11] C. G. Morales-Guio; L. A. Stern; X. Hu, *Chemical Society Reviews* **2014,** 43 (18), 6555-6569.

[12] R. Michalsky; Y. J. Zhang; A. A. Peterson, *ACS Catalysis* **2014,** 4 (5), 1274-1278.

[13] X. Li; X. Hao; A. Abudula; G. Guan, *Journal of Materials Chemistry A* **2016,** 4 (31), 11973-12000.

[14] J. Greeley; T. F. Jaramillo; J. Bonde; I. Chorkendorff; J. K. Nørskov, *Nature Materials* **2006,** 5 (11), 909-913.

[15] W. Sheng; M. Myint; J. G. Chen; Y. Yan, *Energy & Environmental Science* **2013,** 6 (5), 1509-1512.

[16] M. G. Walter; E. L. Warren; J. R. McKone; S. W. Boettcher; Q. Mi; E. A. Santori; N. S. Lewis, *Chemical Reviews* **2010,** 110 (11), 6446-6473.

[17] Y. Zheng; Y. Jiao; Y. Zhu; L. H. Li; Y. Han; Y. Chen; A. Du; M. Jaroniec; S. Z. Qiao, *Nature Communications* **2014,** 5 (1), 1-8.

[18] Q. Lu; G. S. Hutchings; W. Yu; Y. Zhou; R. V. Forest; R. Tao; J. Rosen; B. T. Yonemoto; Z. Cao; H. Zheng, *Nature Communications* **2015,** 6 (1), 1-8.

[19] C. Wan; Y. N. Regmi; B. M. Leonard, *Angewandte Chemie International Edition* **2014,** 53 (25), 6407-6410.

[20] H. Vrubel; X. Hu, *Angewandte Chemie International Edition* **2012,** 51 (51), 12703-12706.

[21] J. Masa; P. Weide; D. Peeters; I. Sinev; W. Xia; Z. Sun; C. Somsen; M. Muhler; W. Schuhmann, *Advanced Energy Materials* **2016,** 6 (6), 1502313.

[22] E. J. Popczun; J. R. McKone; C. G. Read; A. J. Biacchi; A. M. Wiltrout; N. S. Lewis; R. E. Schaak, *Journal of the American Chemical Society* **2013,** 135 (25), 9267-9270.

[23] Z. Huang; Z. Chen; Z. Chen; C. Lv; H. Meng; C. Zhang, *ACS Nano* **2014,** 8 (8), 8121-8129.

[24] J. R. Kitchin; J. K. Nørskov; M. A. Barteau; J. G. Chen, *Catalysis Today* **2005,** 105 (1), 66-73.

[25] A. P. Murthy; J. Madhavan; K. Murugan, *Journal of Power Sources* **2018,** 398, 9-26.

[26] R. Ma; Y. Zhou; Y. Chen; P. Li; Q. Liu; J. Wang, *Angewandte Chemie International Edition* **2015,** 54 (49), 14723-14727.

[27] Y. Liu; G. Yu; G. D. Li; Y. Sun; T. Asefa; W. Chen; X. Zou, *Angewandte Chemie International Edition*

2015, 54 (37), 10752-10757.

[28] W. Cui; N. Cheng; Q. Liu; C. Ge; A. M. Asiri; X. Sun, *ACS Catalysis* **2014,** 4 (8), 2658-2661.

[29] W. F. Chen; C. H. Wang; K. Sasaki; N. Marinkovic; W. Xu; J. T. Muckerman; Y. Zhu; R. Adzic, *Energy & Environmental Science* **2013,** 6 (3), 943-951.

[30] M. Seol; D. H. Youn; J. Y. Kim; J. W. Jang; M. Choi; J. S. Lee; K. Yong, *Advanced Energy Materials* **2014,** 4 (4), 1300775.

[31] D. H. Youn; S. Han; J. Y. Kim; J. Y. Kim; H. Park; S. H. Choi; J. S. Lee, *ACS Nano* **2014,** 8 (5), 5164-5173.

[32] C. He; J. Tao, *Chemical Communications* **2015,** 51 (39), 8323-8325.

[33] Y. Li; H. Wang; L. Xie; Y. Liang; G. Hong; H. Dai, *Journal of the American Chemical Society* **2011,** 133 (19), 7296-7299.

[34] J. S. Li; Y. Wang; C. H. Liu; S. L. Li; Y. G. Wang; L. Z. Dong; Z. H. Dai; Y. F. Li; Y. Q. Lan, *Nature Communications* **2016,** 7 (1), 1-8.

[35] X. Yin; L. Kong; L. Zhang; L. Cheng; N. Travitzky; P. Greil, *International Materials Reviews* **2014,** 59 (6), 326-355.

[36] G. Wang; Z. Gao; S. Tang; C. Chen; F. Duan; S. Zhao; S. Lin; Y. Feng; L. Zhou; Y. Qin, *ACS Nano* **2012,** 6 (12), 11009-11017.

[37] H. Sun; R. Che; X. You; Y. Jiang; Z. Yang; J. Deng; L. Qiu; H. Peng, *Advanced Materials* **2014,** 26 (48), 8120-8125.

[38] M. Q. Ning; M. M. Lu; J. B. Li; Z. Chen; Y. K. Dou; C. Z. Wang; F. Rehman; M. S. Cao; H. B. Jin, *Nanoscale* **2015,** 7 (38), 15734-15740.

[39] M. Han; X. Yin; H. Wu; Z. Hou; C. Song; X. Li; L. Zhang; L. Cheng, *ACS Applied Materials & Interfaces* **2016,** 8 (32), 21011-21019.

[40] Z. M. Dang; T. Zhou; S. H. Yao; J. K. Yuan; J. W. Zha; H. T. Song; J. Y. Li; Q. Chen; W. T. Yang; J. Bai, *Advanced Materials* **2009,** 21 (20), 2077-2082.

[41] P. C. Watts; W. K. Hsu; A. Barnes; B. Chambers, *Advanced Materials* **2003,** 15 (7-8), 600-603.

[42] Y. Duan; Z. Liu; H. Jing; Y. Zhang; S. Li, *Journal of Materials Chemistry* **2012,** 22 (35), 18291-18299.

[43] H. Yang; M. Cao; Y. Li; H. Shi; Z. Hou; X. Fang; H. Jin; W. Wang; J. Yuan, *Advanced Optical Materials* **2014,** 2 (3), 214-219.

[44] H. J. Yang; J. Yuan; Y. Li; Z. L. Hou; H. B. Jin; X. Y. Fang; M. S. Cao, *Solid State Communications* **2013,** 163, 1-6.

[45] J. G. Hartnett; D. Mouneyrac; J. Krupka; J. M. Le Floch; M. E. Tobar; D. Cros, *Journal of Applied Physics* **2011,** 109 (6), 064107.

[46] D. Li; H. B. Jin; M. S. Cao; T. Chen; Y. K. Dou; B. Wen; S. Agathopoulos, *Journal of the American Ceramic Society* **2011,** 94 (5), 1523-1527.

[47] X. Su; Y. Jia; J. Wang; J. Xu; X. He; C. Fu; S. Liu, *Ceramics International* **2013,** 39 (4), 3651-3656.

[48] Y. Hou; L. Cheng; Y. Zhang; Y. Yang; C. Deng; Z. Yang; Q. Chen; X. Du; C. Zhao; L. Zheng, *ACS*

Applied Materials & Interfaces **2018,** 10 (35), 29876-29883.

[49] B. Zhang; J. Li; J. Sun; S. Zhang; H. Zhai; Z. Du, *Journal of the European Ceramic Society* **2002,** 22 (1), 93-99.

[50] S. Sarkar; J. Zou; J. Liu; C. Xu; L. An; L. Zhai, *ACS Applied Materials & Interfaces* **2010,** 2 (4), 1150-1156.

[51] L. P. Rajukumar; M. Belmonte; J. E. Slimak; A. L. Elías; E. Cruz-Silva; N. Perea-López; A. Morelos-Gómez; H. Terrones; M. Endo; P. Miranzo, *Advanced Functional Materials* **2015,** 25 (31), 4985-4993.

[52] M. Han; X. Yin; Z. Hou; C. Song; X. Li; L. Zhang; L. Cheng, *ACS Applied Materials & Interfaces* **2017,** 9 (13), 11803-11810.

[53] J. Yuan; H. J. Yang; Z. L. Hou; W. L. Song; H. Xu; Y. Q. Kang; H. B. Jin; X. Y. Fang; M. S. Cao, *Powder Technology* **2013,** 237, 309-313.

[54] Q. Wen; Y. Feng; Z. Yu; D. L. Peng; N. Nicoloso; E. Ionescu; R. Riedel, *Journal of the American Ceramic Society* **2016,** 99 (8), 2655-2663.

[55] X. Liu; Z. Yu; R. Ishikawa; L. Chen; X. Liu; X. Yin; Y. Ikuhara; R. Riedel, *Acta Materialia* **2017,** 130, 83-93.

[56] W. Verbeek, Production of shaped articles of homogeneous mixtures of silicon carbide and nitride. Google Patents: 1974.

[57] G. D. Winter; W. D. Verbeek; M. D. Mansmann, Formkoerper aus homogenen mischungen von siliciumcarbid und siliciumnitrid und verfahren zu ihrer herstellung. Google Patents: 1974.

[58] P. Colombo; G. Mera; R. Riedel; G. D. Soraru, *Journal of the American Ceramic Society* **2010,** 93 (7), 1805-1837.

[59] M. Benaissa; J. Werckmann; G. Ehret; E. Peschiera; J. Guille; M. Ledoux, *Journal of Materials Science* **1994,** 29 (18), 4700-4707.

[60] W. Yang; H. Miao; Z. Xie; L. Zhang; L. An, *Chemical Physics Letters* **2004,** 383 (5-6), 441-444.

[61] Y. Feng; S. Lai; L. Yang; R. Riedel; Z. Yu, *Ceramics International* **2018,** 44 (7), 8562-8569.

[62] M. Hojamberdiev; R. M. Prasad; K. Morita; Y. Zhu; M. A. Schiavon; A. Gurlo; R. Riedel, *Applied Catalysis B: Environmental* **2012,** 115, 303-313.

[63] M. Hojamberdiev; R. M. Prasad; K. Morita; M. A. Schiavon; R. Riedel, *Microporous and Mesoporous Materials* **2012,** 151, 330-338.

[64] G. D. Sorarù; S. Modena; E. Guadagnino; P. Colombo; J. Egan; C. Pantano, *Journal of the American Ceramic Society* **2002,** 85 (6), 1529-1536.

[65] H. Nowotny; E. Parthe; R. Kieffer; F. Benesovsky, *Monatshefte für Chemie und verwandte Teile anderer Wissenschaften* **1954,** 85 (1), 255-272.

[66] Y. Suzuki; K. Niihara, *Intermetallics* **1998,** 6 (1), 7-13.

[67] Q. Zhu; K. Shobu; E. Tani; K. Kishi; S. Umebayashi, *Journal of the American Ceramic Society* **1999,** 82 (8), 2276-2278.

[68] Q. Zhu; K. Shobu, *Journal of Materials Science Letters* **2000,** 19 (17), 1529-1531.

[69] A. A. Buchheit; G. E. Hilmas; W. G. Fahrenholtz; D. M. Deason; H. Wang, *Intermetallics* **2008,** 16 (7), 854-859.

[70] Q. Zhu; K. Shobu; E. Tani; K. Kishi; S. Umebayashi, *Journal of Materials Science* **2000,** 35 (4), 863-872.

[71] V. Sadagapan; H. Gatos, *Journal of Physics and Chemistry of Solids* **1966,** 27 (2), 235-238.

[72] Y. Feng; Z. Yu; J. Schuch; S. Tao; L. Wiehl; C. Fasel; W. Jaegermann; R. Riedel, *Journal of the American Ceramic Society* **2020,** 103 (1), 508-519.

[73] Y. Feng; Z. Yu; R. Riedel, *Journal of the American Ceramic Society* **2020,** 103 (2), 1385-1395.

[74] Y. Feng; Y. Yang; Q. Wen; R. Riedel; Z. Yu, *ACS Applied Materials & Interfaces* **2020**.

[75] N. S. Lewis; D. G. Nocera, *Proceedings of the National Academy of Sciences* **2006,** 103 (43), 15729-15735.

[76] A. Landman; H. Dotan; G. E. Shter; M. Wullenkord; A. Houaijia; A. Maljusch; G. S. Grader; A. Rothschild, *Nature Materials* **2017,** 16 (6), 646-651.

[77] S. Trasatti, *Journal of Electroanalytical Chemistry* **1999,** 476 (1), 90-91.

[78] J. M. Bockris; E. Potter, *Journal of The Electrochemical Society* **1952,** 99 (4), 169-186.

[79] B. Conway; B. Tilak, *Electrochimica Acta* **2002,** 47 (22-23), 3571-3594.

[80] T. Bligaard; J. K. Nørskov; S. Dahl; J. Matthiesen; C. H. Christensen; J. Sehested, *Journal of Catalysis* **2004,** 224 (1), 206-217.

[81] M. A. Lukowski; A. S. Daniel; F. Meng; A. Forticaux; L. Li; S. Jin, *Journal of the American Chemical Society* **2013,** 135 (28), 10274-10277.

[82] M. Miles; M. Thomason, *Journal of the Electrochemical Society* **1976,** 123 (10), 1459.

[83] I. A. Raj, *Journal of Materials Science* **1993,** 28 (16), 4375-4382.

[84] F. Rosalbino; D. Maccio; E. Angelini; A. Saccone; S. Delfino, *Journal of Alloys and Compounds* **2005,** 403 (1-2), 275-282.

[85] W. F. Chen; J. T. Muckerman; E. Fujita, *Chemical Communications* **2013,** 49 (79), 8896-8909.

[86] Y. N. Regmi; G. R. Waetzig; K. D. Duffee; S. M. Schmuecker; J. M. Thode; B. M. Leonard, *Journal of Materials Chemistry A* **2015,** 3 (18), 10085-10091.

[87] D. Merki; S. Fierro; H. Vrubel; X. Hu, *Chemical Science* **2011,** 2 (7), 1262-1267.

[88] X. Ren; Q. Ma; H. Fan; L. Pang; Y. Zhang; Y. Yao; X. Ren; S. F. Liu, *Chemical Communications* **2015,** 51 (88), 15997-16000.

[89] K. Wang; C. Zhou; D. Xi; Z. Shi; C. He; H. Xia; G. Liu; G. Qiao, *Nano Energy* **2015,** 18, 1-11.

[90] D. Voiry; H. Yamaguchi; J. Li; R. Silva; D. C. Alves; T. Fujita; M. Chen; T. Asefa; V. B. Shenoy; G. Eda, *Nature Materials* **2013,** 12 (9), 850-855.

[91] P. Liu; J. A. Rodriguez, *Journal of the American Chemical Society* **2005,** 127 (42), 14871-14878.

[92] C. G. Read; J. F. Callejas; C. F. Holder; R. E. Schaak, *ACS Applied Materials & Interfaces* **2016,** 8 (20), 12798-12803.

[93] E. J. Popczun; C. G. Read; C. W. Roske; N. S. Lewis; R. E. Schaak, *Angewandte Chemie International*

Edition **2014,** 53 (21), 5427-5430.

[94] Y. Zheng; Y. Jiao; L. H. Li; T. Xing; Y. Chen; M. Jaroniec; S. Z. Qiao, *ACS Nano* **2014,** 8 (5), 5290-5296.

[95] W. Cui; Q. Liu; N. Cheng; A. M. Asiri; X. Sun, *Chemical Communications* **2014,** 50 (66), 9340-9342.

[96] Y. Liu; H. Yu; X. Quan; S. Chen; H. Zhao; Y. Zhang, *Scientific Reports* **2014,** 4, 6843.

[97] B. Zhang; Z. Wen; S. Ci; J. Chen; Z. He, *RSC Advances* **2014,** 4 (90), 49161-49164.

[98] A. B. Laursen; S. Kegnæs; S. Dahl; I. Chorkendorff, *Energy & Environmental Science* **2012,** 5 (2), 5577-5591.

[99] L. Sun; T. Wang; L. Zhang; Y. Sun; K. Xu; Z. Dai; F. Ma, *Journal of Power Sources* **2018,** 377, 142-150.

[100] R. Li; L. Yang; T. Xiong; Y. Wu; L. Cao; D. Yuan; W. Zhou, *Journal of Power Sources* **2017,** 356, 133-139.

[101] P. Xiao; M. A. Sk; L. Thia; X. Ge; R. J. Lim; J. Y. Wang; K. H. Lim; X. Wang, *Energy & Environmental Science* **2014,** 7 (8), 2624-2629.

[102] Z. Xing; Q. Liu; A. M. Asiri; X. Sun, *Advanced Materials* **2014,** 26 (32), 5702-5707.

[103] J. M. McEnaney; J. C. Crompton; J. F. Callejas; E. J. Popczun; A. J. Biacchi; N. S. Lewis; R. E. Schaak, *Chemistry of Materials* **2014,** 26 (16), 4826-4831.

[104] H. Tributsch; J. Bennett, *Journal of Electroanalytical Chemistry and Interfacial Electrochemistry* **1977,** 81 (1), 97-111.

[105] B. Hinnemann; P. G. Moses; J. Bonde; K. P. Jørgensen; J. H. Nielsen; S. Horch; I. Chorkendorff; J. K. Nørskov, *Journal of the American Chemical Society* **2005,** 127 (15), 5308-5309.

[106] Y. Yan; B. Xia; X. Ge; Z. Liu; J. Y. Wang; X. Wang, *ACS Applied Materials & Interfaces* **2013,** 5 (24), 12794-12798.

[107] N. Liu; L. Yang; S. Wang; Z. Zhong; S. He; X. Yang; Q. Gao; Y. Tang, *Journal of Power Sources* **2015,** 275, 588-594.

[108] J. Kibsgaard; T. F. Jaramillo, *Angewandte Chemie International Edition* **2014,** 53 (52), 14433-14437.

[109] X. D. Wang; Y. F. Xu; H. S. Rao; W. J. Xu; H. Y. Chen; W. X. Zhang; D. B. Kuang; C. Y. Su, *Energy & Environmental Science* **2016,** 9 (4), 1468-1475.

[110] J. Xie; H. Zhang; S. Li; R. Wang; X. Sun; M. Zhou; J. Zhou; X. W. Lou; Y. Xie, *Advanced Materials* **2013,** 25 (40), 5807-5813.

[111] L. Liao; S. Wang; J. Xiao; X. Bian; Y. Zhang; M. D. Scanlon; X. Hu; Y. Tang; B. Liu; H. H. Girault, *Energy & Environmental Science* **2014,** 7 (1), 387-392.

[112] P. Xiao; Y. Yan; X. Ge; Z. Liu; J.-Y. Wang; X. Wang, *Applied Catalysis B: Environmental* **2014,** 154, 232-237.

[113] J. Kibsgaard; Z. Chen; B. N. Reinecke; T. F. Jaramillo, *Nature Materials* **2012,** 11 (11), 963.

[114] K. Zhang; H. J. Kim; J. T. Lee; G. W. Chang; X. Shi; W. Kim; M. Ma; K. j. Kong; J. M. Choi; M. S. Song, *ChemSusChem* **2014,** 7 (9), 2489-2495.

[115] X. J. Lv; G. W. She; S. X. Zhou; Y. M. Li, *RSC Advances* **2013,** 3 (44), 21231-21236.

[116] X. Sun; J. Dai; Y. Guo; C. Wu; F. Hu; J. Zhao; X. Zeng; Y. Xie, *Nanoscale* **2014,** 6 (14), 8359-8367.

[117] J. Xie; J. Zhang; S. Li; F. Grote; X. Zhang; H. Zhang; R. Wang; Y. Lei; B. Pan; Y. Xie, *Journal of the American Chemical Society* **2013,** 135 (47), 17881-17888.

[118] W. Zhou; D. Hou; Y. Sang; S. Yao; J. Zhou; G. Li; L. Li; H. Liu; S. Chen, *Journal of Materials Chemistry A* **2014,** 2 (29), 11358-11364.

[119] Z. Shi; K. Nie; Z. J. Shao; B. Gao; H. Lin; H. Zhang; B. Liu; Y. Wang; Y. Zhang; X. Sun, *Energy & Environmental Science* **2017,** 10 (5), 1262-1271.

[120] B. Šljukić; D. M. Santos; M. Vujković; L. Amaral; R. P. Rocha; C. A. Sequeira; J. L. Figueiredo, *ChemSusChem* **2016,** 9 (10), 1200-1208.

[121] K. Zhang; Y. Zhao; S. Zhang; H. Yu; Y. Chen; P. Gao; C. Zhu, *Journal of Materials Chemistry A* **2014,** 2 (44), 18715-18719.

[122] S. Wang; L. Liao; Z. Shi; J. Xiao; Q. Gao; Y. Zhang; B. Liu; Y. Tang, *ChemElectroChem* **2016,** 3 (12), 2110-2115.

[123] L. Ma; Y. Hu; G. Zhu; R. Chen; T. Chen; H. Lu; Y. Wang; J. Liang; H. Liu; C. Yan, *Chemistry of Materials* **2016,** 28 (16), 5733-5742.

[124] H. B. Wu; B. Y. Xia; L. Yu; X. Y. Yu; X. W. D. Lou, *Nature Communications* **2015,** 6 (1), 1-8.

[125] X. Y. Yu; H. Hu; Y. Wang; H. Chen; X. W. Lou, *Angewandte Chemie International Edition* **2015,** 54 (25), 7395-7398.

[126] F. X. Ma; H. B. Wu; B. Y. Xia; C. Y. Xu; X. W. Lou, *Angewandte Chemie International Edition* **2015,** 54 (51), 15395-15399.

[127] L. Ma; L. R. L. Ting; V. Molinari; C. Giordano; B. S. Yeo, *Journal of Materials Chemistry A* **2015,** 3 (16), 8361-8368.

[128] S. T. Hunt; T. Nimmanwudipong; Y. Román‐Leshkov, *Angewandte Chemie International Edition* **2014,** 53 (20), 5131-5136.

[129] C. Wan; B. M. Leonard, *Chemistry of Materials* **2015,** 27 (12), 4281-4288.

[130] L. Kong; Z. Li; L. Liu; R. Huang; M. Abshinova; Z. Yang; C. Tang; P. Tan; C. Deng; S. Matitsine, *International Materials Reviews* **2013,** 58 (4), 203-259.

[131] K. J. Vinoy; R. M. Jha, *Boston, MA: Kluwer Academic Publishers, 1996.* **1996**.

[132] J. H. Oh; K. S. Oh; C. G. Kim; C. S. Hong, *Composites Part B: Engineering* **2004,** 35 (1), 49-56.

[133] G. Shen; Z. Xu; Y. Li, *Journal of Magnetism and Magnetic Materials* **2006,** 301 (2), 325-330.

[134] M. Meshram; N. K. Agrawal; B. Sinha; P. Misra, *Journal of Magnetism and Magnetic Materials* **2004,** 271 (2-3), 207-214.

[135] V. Kodali, *Inc., New York* **2001**.

[136] M. M. Lu; M. S. Cao; Y. H. Chen; W. Q. Cao; J. Liu; H. L. Shi; D. Q. Zhang; W. Z. Wang; J. Yuan, *ACS Applied Materials & Interfaces* **2015,** 7 (34), 19408-19415.

[137] P. Wang; L. Cheng; L. Zhang, *Carbon* **2017,** 125, 207-220.

[138] D. Micheli; A. Vricella; R. Pastore; M. Marchetti, *Carbon* **2014,** 77, 756-774.

[139] J. B. Goodenough, *IEEE Transactions on Magnetics* **2002,** 38 (5), 3398-3408.

[140] X. Zhang; X. Dong; H. Huang; Y. Liu; W. Wang; X. Zhu; B. Lv; J. Lei; C. Lee, *Applied Physics Letters* **2006,** 89 (5), 053115.

[141] S. Ni; S. Lin; Q. Pan; F. Yang; K. Huang; D. He, *Journal of Physics D: Applied Physics* **2009,** 42 (5), 055004.

[142] S. S. Kim; S. T. Kim; Y. C. Yoon; K. S. Lee, *Journal of Applied Physics* **2005,** 97 (10), 10F905.

[143] B. Lu; X. Dong; H. Huang; X. Zhang; X. Zhu; J. Lei; J. Sun, *Journal of Magnetism and Magnetic Materials* **2008,** 320 (6), 1106-1111.

[144] B. Zhang; Y. Feng; J. Xiong; Y. Yang; H. Lu, *IEEE Transactions on Magnetics* **2006,** 42 (7), 1778-1781.

[145] J. Qiu; M. Gu; H. Shen, *Journal of Magnetism and Magnetic Materials* **2005,** 295 (3), 263-268.

[146] F. Tabatabaie; M. Fathi; A. Saatchi; A. Ghasemi, *Journal of Alloys and Compounds* **2009,** 470 (1-2), 332-335.

[147] S. Sugimoto; K. Haga; T. Kagotani; K. Inomata, *Journal of Magnetism and Magnetic Materials* **2005,** 290, 1188-1191.

[148] B. Wen; M. Cao; M. Lu; W. Cao; H. Shi; J. Liu; X. Wang; H. Jin; X. Fang; W. Wang, *Advanced Materials* **2014,** 26 (21), 3484-3489.

[149] M. S. Cao; W. L. Song; Z. L. Hou; B. Wen; J. Yuan, *Carbon* **2010,** 48 (3), 788-796.

[150] A. Wadhawan; D. Garrett; J. M. Pérez, *Applied Physics Letters* **2003,** 83 (13), 2683-2685.

[151] L. Kong; X. Yin; Y. Zhang; X. Yuan; Q. Li; F. Ye; L. Cheng; L. Zhang, *The Journal of Physical Chemistry C* **2013,** 117 (38), 19701-19711.

[152] S. C. Chiu; H. C. Yu; Y. Y. Li, *The Journal of Physical Chemistry C* **2010,** 114 (4), 1947-1952.

[153] V. T. Truong; S. Riddell; R. Muscat, *Journal of Materials Science* **1998,** 33 (20), 4971-4976.

[154] W. Duan; X. Yin; F. Ye; Q. Li; M. Han; X. Liu; Y. Cai, *Journal of Materials Chemistry C* **2016,** 4 (25), 5962-5969.

[155] J. B. Kim; S. K. Lee; C. G. Kim, *Composites Science and Technology* **2008,** 68 (14), 2909-2916.

[156] Y. Fan; H. Yang; M. Li; G. Zou, *Materials Chemistry and Physics* **2009,** 115 (2-3), 696-698.

[157] W. L. Song; M. S. Cao; Z. L. Hou; X. Y. Fang; X. L. Shi; J. Yuan, *Applied Physics Letters* **2009,** 94 (23), 233110.

[158] T. Wu; Y. Liu; X. Zeng; T. Cui; Y. Zhao; Y. Li; G. Tong, *ACS Applied Materials & Interfaces* **2016,** 8 (11), 7370-7380.

[159] C. Zhang; B. Wang; J. Xiang; C. Su; C. Mu; F. Wen; Z. Liu, *ACS Applied Materials & Interfaces* **2017,** 9 (34), 28868-28875.

[160] X. J. Zhang; G. S. Wang; W. Q. Cao; Y. Z. Wei; J. F. Liang; L. Guo; M. S. Cao, *ACS Applied Materials & Interfaces* **2014,** 6 (10), 7471-7478.

[161] H. Zhang; X. Tian; C. Wang; H. Luo; J. Hu; Y. Shen; A. Xie, *Applied Surface Science* **2014,** 314,

228-232.

[162] X. Jian; X. Xiao; L. Deng; W. Tian; X. Wang; N. Mahmood; S. Dou, *ACS Applied Materials & Interfaces* **2018,** 10 (11), 9369-9378.

[163] G. Zheng; X. Yin; S. Liu; X. Liu; J. Deng; Q. Li, *Journal of the European Ceramic Society* **2013,** 33 (11), 2173-2180.

[164] W. L. Song; M. S. Cao; Z. L. Hou; J. Yuan; X. Y. Fang, *Scripta Materialia* **2009,** 61 (2), 201-204.

[165] C. Liang; Z. Wang, *ACS Applied Materials & Interfaces* **2017,** 9 (46), 40690-40696.

[166] X. Jian; W. Tian; J. Li; L. Deng; Z. Zhou; L. Zhang; H. Lu; L. Yin; N. Mahmood, *ACS Applied Materials & Interfaces* **2019,** 11 (17), 15869-15880.

[167] X. Hao; X. Yin; L. Zhang; L. Cheng, *Journal of Materials Science & Technology* **2013,** 29 (3), 249-254.

[168] S. Dong; P. Hu; X. Zhang; J. Han; Y. Zhang; X. Luo, *Ceramics International* **2018,** 44 (6), 7141-7150.

[169] J. Cordelair; P. Greil, *Journal of the European Ceramic Society* **2000,** 20 (12), 1947-1957.

[170] C. Luo; W. Duan; X. Yin; J. Kong, *The Journal of Physical Chemistry C* **2016,** 120 (33), 18721-18732.

[171] M. Zaheer; G. Motz; R. Kempe, *Journal of Materials Chemistry* **2011,** 21 (46), 18825-18831.

[172] X. Liu; Z. Yu; R. Ishikawa; L. Chen; X. Yin; Y. Ikuhara; R. Riedel, *Journal of Materials Chemistry C* **2017,** 5 (31), 7950-7960.

[173] H. L. Zhu; Y. J. Bai; R. Liu; N. Lun; Y. X. Qi; F. D. Han; J. Q. Bi, *Journal of Materials Chemistry* **2011,** 21 (35), 13581-13587.

[174] R. Meng; T. Zhang; P. Jiao; M. Zhang; X. Huang; L. Xia; B. Zhong; H. Zhao; H. Wang; G. Wen, *Journal of Alloys and Compounds* **2019,** 798, 386-393.

[175] M. Zhang; H. Lin; S. Ding; T. Wang; Z. Li; A. Meng; Q. Li; Y. Lin, *Composites Part B: Engineering* **2019,** 179, 107525.

[176] X. Ye; Z. Chen; M. Li; T. Wang; C. Wu; J. Zhang; Q. Zhou; H. Liu; S. Cui, *ACS Sustainable Chemistry & Engineering* **2019,** 7 (22), 18395-18404.

[177] Y. Zhang; X. Yin; F. Ye; L. Kong, *Journal of the European Ceramic Society* **2014,** 34 (5), 1053-1061.

[178] P. Colombo, *Polymer derived ceramics: from nano-structure to applications*. DEStech Publications, Inc: 2010.

[179] G. D. Sorarù; H. J. Kleebe; R. Ceccato; L. Pederiva, *Journal of the European Ceramic Society* **2000,** 20 (14-15), 2509-2517.

[180] J. Evans, *Journal of the European Ceramic Society* **2008,** 28 (7), 1421-1432.

[181] R. Harshe; C. Balan; R. Riedel, *Journal of the European Ceramic Society* **2004,** 24 (12), 3471-3482.

[182] N. Janakiraman; F. Aldinger, *Journal of the European Ceramic Society* **2009,** 29 (1), 163-173.

[183] K. Okamura; T. Shimoo; K. Suzuya; K. Suzuki, *Journal of the Ceramic Society of Japan* **2006,** 114 (1330), 445-454.

[184] M. Narisawa; A. Idesaki; S. Kitano; K. Okamura; M. Sugimoto; T. Seguchi; M. Itoh, *Journal of the American Ceramic Society* **1999,** 82 (4), 1045-1051.

[185] L. A. Liew; Y. Liu; R. Luo; T. Cross; L. An; V. M. Bright; M. L. Dunn; J. W. Daily; R. Raj, *Sensors and Actuators A: Physical* **2002,** 95 (2-3), 120-134.

[186] T. A. Pham; P. Kim; M. Kwak; K. Y. Suh; D.-P. Kim, *Chemical Communications* **2007,** (39), 4021-4023.

[187] F. Babonneau; G. D. Sorarú; K. J. Thorne; J. D. Mackenzie, *Journal of the American Ceramic Society* **1991,** 74 (7), 1725-1728.

[188] T. Ishikawa; T. Yamamura; K. Okamura, *Journal of Materials Science* **1992,** 27 (24), 6627-6634.

[189] F. Babonneau; G. D. Sorarù, *Journal of the European Ceramic Society* **1991,** 8 (1), 29-34.

[190] T. Ishikawa; S. Kajii; K. Matsunaga; T. Hogami; Y. Kohtoku; T. Nagasawa, *Science* **1998,** 282 (5392), 1295-1297.

[191] T. Ishikawa; Y. Kohtoku; K. Kumagawa, *Journal of Materials Science* **1998,** 33 (1), 161-166.

[192] E. Ionescu; B. Papendorf; H. J. Kleebe; F. Poli; K. Müller; R. Riedel, *Journal of the American Ceramic Society* **2010,** 93 (6), 1774-1782.

[193] J. Cordelair; P. Greil, *Journal of the American Ceramic Society* **2001,** 84 (10), 2256-2259.

[194] R. Hauser; A. Francis; R. Theismann; R. Riedel, *Journal of Materials Science* **2008,** 43 (12), 4042-4049.

[195] C. Linck; E. Ionescu; B. Papendorf; D. Galuskova; D. Galusek; P. Ŝajgalík; R. Riedel, *International Journal of Materials Research* **2012,** 103 (1), 31-39.

[196] Q. Sun; J. W. Lam; K. Xu; H. Xu; J. A. Cha; P. C. Wong; G. Wen; X. Zhang; X. Jing; F. Wang, *Chemistry of Materials* **2000,** 12 (9), 2617-2624.

[197] B. Clauſ, *Ceramic Matrix Composites: Fiber Reinforced Ceramics and their Applications* **2008**.

[198] R. Gadow; F. Kern, *Advanced Engineering Materials* **2002,** 4 (11), 883-886.

[199] L. Brigo; J. E. M. Schmidt; A. Gandin; N. Michieli; P. Colombo; G. Brusatin, *Advanced Science* **2018,** 5 (12), 1800937.

[200] R. Kolb; C. Fasel; V. Liebau-Kunzmann; R. Riedel, *Journal of the European Ceramic Society* **2006,** 26 (16), 3903-3908.

[201] V. Liebau-Kunzmann; C. Fasel; R. Kolb; R. Riedel, *Journal of the European Ceramic Society* **2006,** 26 (16), 3897-3901.

[202] H. Nowotny; E. Parthe; R. Kieffer; F. Benesovsky, *Monatshefte für Chemie und verwandte Teile anderer Wissenschaften* **1954,** 85 (1), 255-272.

[203] E. Parthe; W. Jeitschko; V. Sadagopan, *Acta Crystallographica* **1965,** 19 (6), 1031-1037.

[204] B. Gnesin; I. Gnesin, *Inorganic Materials* **2015,** 51 (10), 991-998.

[205] B. Gnesin; I. Gnesin; A. Nekrasov, *Intermetallics* **2013,** 41, 82-95.

[206] S. Maloy; A. H. Heuer; J. Lewandowski; J. Petrovic, *Journal of the American Ceramic Society* **1991,** 74 (10), 2704-2706.

[207] B. Gnesin; I. Gnesin, *Inorganic Materials* **2017,** 53 (7), 701-707.

[208] D. B. Lee; S. W. Woo In *Oxidation of SiOC composite having dispersoids of $Mo_{4.8}Si_3C_{0.6}$ and $MoSi_2$*, Materials Science Forum, Trans Tech Publ: 2005; pp 165-168.

[209] M. Seifollahi Bazarjani; H. J. Kleebe; M. M. Müller; C. Fasel; M. Baghaie Yazdi; A. Gurlo; R. Riedel, *Chemistry of Materials* **2011,** 23 (18), 4112-4123.

[210] S. Kaur; G. Cherkashinin; C. Fasel; H.-J. Kleebe; E. Ionescu; R. Riedel, *Journal of the European Ceramic Society* **2016,** 36 (15), 3553-3563.

[211] Z. Yu; P. Zhang; Y. Feng; S. Li; Y. Pei, *Journal of the American Ceramic Society* **2016,** 99 (8), 2615-2624.

[212] M. Morey; J. Bryan; S. Schwarz; G. Stucky, *Chemistry of Materials* **2000,** 12 (11), 3435-3444.

[213] Z. Yu; Y. Feng; S. Li; Y. Pei, *Journal of the European Ceramic Society* **2016,** 36 (15), 3627-3635.

[214] J. Wu; Y. Li; L. Chen; Z. Zhang; D. Wang; C. Xu, *Journal of Materials Chemistry* **2012,** 22 (14), 6542-6545.

[215] J. D. Peterson; S. Vyazovkin; C. A. Wight, *Macromolecular Chemistry and Physics* **2001,** 202 (6), 775-784.

[216] B. H. Toby; R. B. Von Dreele, *Journal of Applied Crystallography* **2013,** 46 (2), 544-549.

[217] A. Ferrari; J. Robertson, *Physical Review B* **2001,** 64 (7), 075414.

[218] G. Mera; A. Navrotsky; S. Sen; H. J. Kleebe; R. Riedel, *Journal of Materials Chemistry A* **2013,** 1 (12), 3826-3836.

[219] W. F. Chen; S. Iyer; S. Iyer; K. Sasaki; C.-H. Wang; Y. Zhu; J. T. Muckerman; E. Fujita, *Energy & Environmental Science* **2013,** 6 (6), 1818-1826.

[220] N. S. Alhajri; D. H. Anjum; K. Takanabe, *Journal of Materials Chemistry A* **2014,** 2 (27), 10548-10556.

[221] D. H. van Dorp; N. Hijnen; M. Di Vece; J. J. Kelly, *Angewandte Chemie International Edition* **2009,** 48 (33), 6085-6088.

[222] K. Ojha; S. Saha; H. Kolev; B. Kumar; A. K. Ganguli, *Electrochimica Acta* **2016,** 193, 268-274.

[223] B. P. Swain, *Surface and Coatings Technology* **2006,** 201 (3-4), 1589-1593.

[224] J. Wan; J. Wu; X. Gao; T. Li; Z. Hu; H. Yu; L. Huang, *Advanced Functional Materials* **2017,** 27 (45), 1703933.

[225] Z. Luo; R. Miao; T. D. Huan; I. M. Mosa; A. S. Poyraz; W. Zhong; J. E. Cloud; D. A. Kriz; S. Thanneeru; J. He, *Advanced Energy Materials* **2016,** 6 (16), 1600528.

[226] W. Gao; Y. Shi; Y. Zhang; L. Zuo; H. Lu; Y. Huang; W. Fan; T. Liu, *ACS Sustainable Chemistry & Engineering* **2016,** 4 (12), 6313-6321.

[227] L. F. Pan; Y. H. Li; S. Yang; P. F. Liu; M. Q. Yu; H. G. Yang, *Chemical Communications* **2014,** 50 (86), 13135-13137.

[228] Y. Zhao; K. Kamiya; K. Hashimoto; S. Nakanishi, *Journal of the American Chemical Society* **2015,** 137 (1), 110-113.

[229] M. Fan; H. Chen; Y. Wu; L. L. Feng; Y. Liu; G.-D. Li; X. Zou, *Journal of Materials Chemistry A* **2015,** 3 (31), 16320-16326.

[230] C. Tang; A. Sun; Y. Xu; Z. Wu; D. Wang, *Journal of Power Sources* **2015,** 296, 18-22.

[231] W. Li; D. Li; X. Gao; A. Gurlo; S. Zander; P. Jones; A. Navrotsky; Z. Shen; R. Riedel; E. Ionescu, *Dalton Transactions* **2015,** 44 (17), 8238-8246.

[232] B. Marinho; M. Ghislandi; E. Tkalya; C. E. Koning; G. de With, *Powder Technology* **2012,** 221, 351-358.

[233] B. Román-Manso; E. Domingues; F. M. Figueiredo; M. Belmonte; P. Miranzo, *Journal of the European Ceramic Society* **2015,** 35 (10), 2723-2731.

[234] R. M. Prasad; G. Mera; K. Morita; M. Müller; H.-J. Kleebe; A. Gurlo; C. Fasel; R. Riedel, *Journal of the European Ceramic Society* **2012,** 32 (2), 477-484.

[235] J. Lipowitz; J. A. Rabe; L. K. Frevel; R. L. Miller, *Journal of Materials Science* **1990,** 25 (4), 2118-2124.

[236] J. Wan; M. J. Gasch; A. K. Mukherjee, *Journal of the American Ceramic Society* **2001,** 84 (10), 2165-2169.

[237] Y. Y. Chen; Y. Zhang; W. J. Jiang; X. Zhang; Z. Dai; L. J. Wan; J. S. Hu, *ACS Nano* **2016,** 10 (9), 8851-8860.

[238] S. Wang; J. Wang; M. Zhu; X. Bao; B. Xiao; D. Su; H. Li; Y. Wang, *Journal of the American Chemical Society* **2015,** 137 (50), 15753-15759.

[239] F. Dalcanale; J. Grossenbacher; G. Blugan; M. R. Gullo; A. Lauria; J. Brugger; H. Tevaearai; T. Graule; M. Niederberger; J. Kuebler, *Journal of the European Ceramic Society* **2014,** 34 (15), 3559-3570.

[240] J. Kaspar; M. Graczyk-Zajac; S. Choudhury; R. Riedel, *Electrochimica Acta* **2016,** 216, 196-202.

[241] J. Diao; W. Yuan; Y. Su; Y. Qiu; X. Guo, *Advanced Materials Interfaces* **2018,** 5 (13), 1800223.

[242] Z. Hao; S. Yang; J. Niu; Z. Fang; L. Liu; Q. Dong; S. Song; Y. Zhao, *Chemical Science* **2018,** 9 (25), 5640-5645.

[243] J. Q. Chi; X. Shang; S. S. Lu; B. Dong; Z. Z. Liu; K. L. Yan; W. K. Gao; Y. M. Chai; C. G. Liu, *Carbon* **2017,** 124, 555-564.

[244] F. Li; X. Zhao; J. Mahmood; M. S. Okyay; S. M. Jung; I. Ahmad; S. J. Kim; G. F. Han; N. Park; J. B. Baek, *ACS Nano* **2017,** 11 (7), 7527-7533.

[245] K. Zhang; Y. Zhao; D. Fu; Y. Chen, *Journal of Materials Chemistry A* **2015,** 3 (11), 5783-5788.

[246] A. C. e Silva; M. Kaufman, *Metallurgical and Materials Transactions A* **1994,** 25 (1), 5-15.

[247] D. Ding; W. Zhou; B. Zhang; F. Luo; D. Zhu, *Journal of Materials Science* **2011,** 46 (8), 2709-2714.

[248] Q. Wen; Z. Yu; R. Riedel, *Progress in Materials Science* **2019**, 100623.

[249] S. I. Nakashima; H. Harima, *Physica Status Solidi (A)* **1997,** 162 (1), 39-64.

[250] P. Ivanov; V. Chelnokov, *Semiconductor Science and Technology* **1992,** 7 (7), 863.

[251] A. Sihvola, *Subsurface Sensing Technologies and Applications* **2000,** 1 (4), 393-415.

[252] C. Wang; X. Han; P. Xu; X. Zhang; Y. Du; S. Hu; J. Wang; X. Wang, *Applied Physics Letters* **2011,**

98 (7), 072906.

[253] Z. Guo; G. Blugan; T. Graule; M. Reece; J. Kuebler, *Journal of the European Ceramic Society* **2007,** 27 (5), 2153-2161.

[254] D. Micheli; R. Pastore; G. Gradoni; M. Marchetti, *AIP Advances* **2013,** 3 (11), 112132.

[255] P. Miles; W. Westphal; A. Von Hippel, *Reviews of Modern Physics* **1957,** 29 (3), 279.

[256] F. Ye; Q. Song; Z. Zhang; W. Li; S. Zhang; X. Yin; Y. Zhou; H. Tao; Y. Liu; L. Cheng, *Advanced Functional Materials* **2018,** 28 (17), 1707205.

[257] J. Rodríguez-Carvajal, *Physica B* **1993,** 192 (1-2), 55-69.

[258] P. Thompson; D. Cox; J. Hastings, *Journal of Applied Crystallography* **1987,** 20 (2), 79-83.

[259] D. V. Baxter; M. H. Chisholm; G. J. Gama; V. F. DiStasi; A. L. Hector; I. P. Parkin, *Chemistry of Materials* **1996,** 8 (6), 1222-1228.

Acknowledgements

Finally, it comes to acknowledgements, the indispensable part of a Ph.D. thesis. In spite that it is impossible to completely express my appreciation to the people who supported me during my Ph.D. period by saying some nice words, I still want to say:

I would like to express the deepest appreciation and respect to Prof. Dr. Ralf Riedel, my doctoral supervisor, who gave me a golden opportunity to work in his group. Many thanks for his continuous support, nice suggestions and warm encouragements during my Ph.D. study. I really enjoy and appreciate everyday working in his group and every time talking with him. His genius attitude and wisdom in scientific research teaches me how to continue my research career in future.

I am very grateful to my co-supervisor Prof. Dr. Zhaoju Yu, who was also my master supervisor. She introduced me into the field of polymer-derived ceramics. Warm thanks for her outstanding supervision and important support on my 7-years scientific research. I also sincerely acknowledge for her valuable comments and careful revision of the Ph.D. dissertation. In addition, many thanks for her warm encouragements and concerns on my master work, Ph.D. work and life.

I would like to greatly acknowledge the Chinese Scholarship Council (CSC) for 4-year financial support on my Ph.D. study in Germany. I'm proud of this experience forever.

I sincerely acknowledge Prof. Dr. Wolfram Jaegermann for allowing me using electrochemical devices and XPS in his lab as well as revising my manuscript.

I sincerely thank M. Sc. Jona Schuch for kindly supporting my work, especially in electrochemical measurements and XPS. Moreover, he has shared his plentiful experience with me on electrochemical characterization, as well as his collaboration on the first part of this Ph.D. work which has been published.

I sincerely thank Dr. Qingbo Wen for his great support with respect to my experiments from using apparatus to analyzing data. I also sincerely acknowledge his valuable comments and careful revision of my manuscript. I really enjoy that we have been working in the same office for 3 years.

I would like to thank PD Dr. Leonore Wiehl for teaching me the XRD refinement as well as revising my manuscript. I really appreciate that she helped me to identify the Nowotny phase in SiC-based nanocomposites.

I would like to thank M.Sc. Yujing Yang (Xiamen University, China) for microwave absorption measurements.

I also sincerely thank Dipl. Claudia Fasel for a lot of TG/MS measurements, elemental analysis as well as her nice supports on all other daily experiments.

I would like to sincerely acknowledge Dr. Magdalena Joanna Graczyk-Zajac for supporting my electrical conductivity measurements.

I also sincerely thank M.Sc. Nan Chai for a lot of Raman measurements as well as her nice supports on all other daily experiments.

I would like to thank Dr. Cong Zhou for the training of BET measurements and strong supports to perform my experiments.

I also would like to thank Dr. Isabel Gonzalo de Juan, Dipl. Dario De Carolis, M. Sc. Ying Zhan M. Sc. Sefa Akca Dr. Men Hu, M. Sc. Benjamin Juretzka, Dr. Dragoljub Vrankovic, M. Sc. Alexander Kempf, Dr. Christina Stabler, Dr. Felix Rosenburg, Dr. Fangtong Xie, Dr. Xingmin Liu, M. Sc. Alexander Ott, Mrs. Su-Chen Chang and all other Dispersive Solids group members who kindly supported my work or my life in different ways.

I really appreciate all my friends in Darmstadt and the time we spend together.

Particularly, I would like to deeply thank my dear parents, Mr. Dequan Feng (冯德全) and Mrs. Daoxiang Hu (胡稻芗) and all other family members who always love me, trust me and encourage me in my life.

Curriculum vitae

Yao Feng

Nationality: China

Gender: Male

Date of Birth: 05/04/1991

E-mail: y.feng@materials.tu-darmstadt.de or fengyao2554@gmail.com

Address: Nieder-Ramstädter Str. 11, 64283 Darmstadt, Germany

Education

- **Ph.D. Candidate of Material Science (Oct. 2016 ~ Jun. 2020)**, Department of Materials and Earth Sciences, Technische Universität Darmstadt, Germany.
- **Master of Polymeric Chemistry and Physics (Sep. 2013 ~ Jun. 2016)**, Department of Materials, Xiamen University, China
- **Bachelor of Polymer Materials and Engineering (Sep. 2009 ~ Jun. 2013)**, Department of Chemistry, Xiangtan University, China
- **Bachelor of Business Administration (Double Degree, Sep. 2009 ~ Jun. 2013)**, Department of Business, Xiangtan University, China

Research Experience

- **10/2016~ , Supervisor:** Prof. Dr. Ralf Riedel
  - **Program:** Electrocatalytic property and electromagnetic wave absorbing performance of single-source-precursor synthesized SiC-based nanocomposites with an in-situ formed Nowotny phase.
- **09/2013 ~ 06/2016, Supervisor**: Prof. Dr. Zhaoju Yu
  - **Program:** Synthesis and properties of porous ceramics via a polymer-derived ceramic route.
- **11/2009 ~ 06/2013, Supervisor:** Prof. Dr. Hailiang Zhang

Conferences

- **Feng Y**, Yu Z, Schuch J, Tao S, Wiehl L, Fasel C, Jaegermann W, Riedel R, Ternary Nowotny rhase $Mo_{3+2x}Si_3C_{0.6}$ dispersed in a porous SiC/C matrix: A novel catalyst for hydrogen evolution reaction. *HT-CMC 10th (2019), Bordeaux, France.* (**Oral presentation)**

Honors and Awards

- Chinese Scholarship for 4 Years of Ph.D. Work in Germany 2016-2020
- Scholarship of Xiamen University March 2016
- Scholarship of Department of Materials, Xiamen University March 2014

Research Skills

- Chemical synthesis and characterization: Schlenk technique for oxygen and moisture sensitive materials, TG/MS analysis, FI-TR analysis, NMR analysis, etc.
- Microstructure characterization: XRD, Raman, SEM, TEM, N_2 adsorption BET and Elemental Analysis, etc.
- Electrochemical characterization (electrochemical impedance spectroscopy, cyclic voltammogram, etc.).
- Analysis of dielectric properties, microwave absorption and electromagnetic interference shielding performance.

Publications and patents (2015 ~ 2020)

1. **Feng Y**, Yang Y, Wen Q, Riedel R, Yu Z, Dielectric properties and electromagnetic wave absorbing performance of single-source-precursor synthesized $Mo_{4.8}Si_3C_{0.6}$/C/SiC nanocomposites with an in-situ formed Nowotny phase. *ACS Applied Materials & Interfaces*, 2 (2020) 16912-16921.

2. **Feng Y**, Yu Z, Schuch J, Tao S, Wiehl L, Fasel C, Jaegermann W, Riedel R, Ternary Nowotny rhase $Mo_{3+2x}Si_3C_{0.6}$ dispersed in a porous SiC/C matrix: A novel catalyst for hydrogen evolution reaction. *Journal of the American Ceramic Society*, 103 (2020) 508-519.

3. **Feng Y**, Yu Z, Riedel R, Enhanced hydrogen evolution reaction catalyzed by carbon-rich $Mo_{4.8}Si_3C_{0.6}$/SiC/C_{free} nanocomposites via a PDC approach. *Journal of the American Ceramic Society*, 103 (2020) 1385-1395.

4. Jia Sun, Wen Q, Li T, Wiehl L, Fasel C, **Feng Y**, Carolis D.D, Yu Z, Fu Q, Riedel R, Phase evolution of SiOC-based ceramic nanocomposites derived from a polymethylsiloxane modified by Hf- and Ti-alkoxides, *Journal of the American Ceramic Society*, 103 (2020) 1436-1445.

5. **Feng Y**, Lai S, Yang L, Riedel R, Yu Z, Polymer-derived porous Bi_2WO_6/SiC(O) ceramic nanocomposites with high photodegradation efficiency towards Rhodamine B. *Ceramics International*, 44(2018),8562-8569.

6. Yu Z, Li S, Pei Zhang, **Feng Y**, Liu X, Polymer-derived mesoporous Ni/SiOC(H) ceramic nanocomposites for efficient removal of acid fuchsin, *Ceramics International*, 43 (2017) 4520-4526.

7. Yu Z, Pei Y, Lai S, Li S, **Feng Y**, Liu X, Single-source-precursor synthesis, microstructure and high temperature behavior of TiC-TiB_2-SiC ceramic nanocomposites, *Ceramics International*, 43 (2017) 5949–5956.

8. Yu Z, **Feng Y**, Li S, Pei Y, Influence of the polymer-polymer miscibility on the formation of mesoporous SiC(O) ceramics for highly efficient adsorption of organic dyes, *Journal of the European Ceramic Society*, 36 (2016) 3627-3635.

9. Wen Q, **Feng Y**, Yu Z, Peng D, Nicoloso N, Ionescu E, Riedel R, Microwave absorption of SiC/HfC_xN_{1-x}/C ceramic nanocomposites with HfC_xN_{1-x}-carbon core–shell particles, *Journal of the American Ceramic Society*, 9 (2016) 2655–2663.

10. Yu Z, Zhang P, **Feng Y**, Li S, Pei Y, Template-free synthesis of porous Fe_3O_4/SiOC(H) nanocomposites with enhanced catalytic activity, *Journal of the American Ceramic Society*, 99 (2016) 2615-2624.

11. Yu Z, Min H, Yang L, **Feng Y**, Zhang P, Riedel R, Influence of the architecture of dendritic-like polycarbosilanes on the ceramic yield, *Journal of the European Ceramic Society*, 35 (2015) 1161-

1171.

Cover:

Top-left: the crystal structure of the Nowotny phase;

Top-right: the crystal structure of the $MoSi_2$. It can be formed by adjusting the carbon content of ceramics;

Central part: the schematic illustration showing the microstructure of $Mo_{4.8}Si_3C_{0.6}/SiC/C_{free}$ ceramic nanocomposites.

Bottom-left: the figure of microwave absorption performance of the SMC-D1-1500 ºC;

Bottom-right: the schematic illustration of the porous NP/C/SiC-based ceramic nanocomposites for HER.